Université du Québec
Institut nationale de la recherche scientifique
Centre Énergie Matériaux Télécommunications

Development of Ytterbium Laser-based Terahertz Sources and Enhancing the Terahertz Emission of GaAs-based Photoconductive Antennas via the Nanodecoration of Their Surfaces by Pulsed-Laser-Deposited Gold Nanoparticles

Par

Elchin Isgandarov

Thèse présentée pour l'obtention du grade de Philosophie Doctor (Ph.D.) en

Sciences de l'Énergie et des Matériaux

Jury d'évaluation

Président du jury et Examinateur interne	François Vidal INRS-EMT
Examinateur externe	Ke Wu Department of Electrical Engineering Polytechnique Montréal
Examinateur externe	Damien Bigourd Laboratoire de l'Intégration du Matériau au Système Université Bordeaux
Directeur de recherche	Tsuneyuki Ozaki INRS-EMT

ACKNOWLEDGMENT

First of all, I would like to express my sincere gratitude and appreciation to my Ph.D. supervisor, Dr. Tsuneyuki Ozaki, who gave me the opportunity to work in his team. His guidance and advice carried me through all the stages of the research and writing this thesis. I am also pleased to thank Dr. Xavier Ropagnol, who helped me acquire the necessary fundamental skills needed to conduct my experiments on building THz-TDS setup and characterization of various THz sources. I would also like to take this opportunity to thank our collaborator, Dr. My Ali El Khakani, and his team for their assistance during the nanodecoration process of my samples, and for providing all the experimental analysis that helped to better understand the underlying phenomena of my experiments. I also want to express my gratitude to Dr. Alessandro Tomassino for his insightful remarks and helpful suggestions on the thesis. My gratitude also goes to Philippe Lassonde and Antoine Laramée for their contribution to my experiments on the characterization process of our femtosecond Yb laser source. I am also very grateful to Claude Sirois and Carol Morissette from the technical team of the mechanical workshop for their immediate assistance when needed. I would also like to express my thanks to the entire defense committee for accepting and time for the evaluation of my thesis. Finally, I am very grateful to my family, friends, and all my colleagues for their moral support, which has been essential to the completion of this work

ABSTRACT

The science and technology of terahertz (THz) electromagnetic radiation has witnessed significant advances over the past few decades. For most of the 20th century, this part of the electromagnetic spectrum was modest due to the lack of tunable high-power sources and fast, sensitive detectors, thus dubbed the THz gap. Nowadays, we can count various techniques for the generation and detection of THz radiation. Among these techniques, photoconductive antennas (PCAs) are widely used devices for THz wave generation and detection. With their unique characteristics such as good shot-to-shot pulse stability of the radiated THz pulses, compactness, and relatively higher optical-to-THz conversion efficiency while pumping the lower optical pump power, PCAs have been used for a wide range of applications. The THz sources have become increasingly advanced over the past few decades, due to the increasing availability and commercialization of ultrafast Ti:Sapphire lasers generating femtosecond pulses at the central wavelength of 800 nm. Today, we can count many efficient THz sources and detectors that can be operated at the fundamental and secondary harmonic (SH) wavelengths of Ti:Sapphire laser.

Recently, Ytterbium (Yb)-doped femtosecond lasers have become the main promising alternative to Ti:Sapphire light sources due to their obvious advantages of stability, compactness, and achieving higher average power levels with higher pulse repetition rates. In addition, relatively low cost, free maintenance, and higher heat transfer from the active medium to air make Yb-lasers very attractive compared to Ti:Sapphire lasers. The latter advantages make Yb-lasers very attractive light sources for applications in THz technology. From this perspective, in this thesis, we explored the implementation of various THz sources driven by a femtosecond Yb laser oscillator delivered optical pulses at the fundamental and SH wavelengths of 1045 and 522 nm, respectively. Specifically, we first performed a series of comparative studies on two optical rectification THz sources excited by the fundamental pulses of the Yb laser at 1045. Then, the fabrication and characterization of the THz photoconductive sources were studied using the SHG of the Yb laser at 522 nm. In addition, considering one of the current limitations of the optical-THz conversion efficiency in conventional photoconductive sources, we presented a new method to improve their radiation efficiency. To this end, a systematic study of the THz radiation performance of photoconductive antennas (PCAs) decorated with various concentrations of NPs has been implemented under the excitation of 522 nm laser pulses. The novel pulsed laser deposition (PLD) method presented for the decoration of PCAs allows the density of the deposited NPs to be progressively adjusted over the excitation area, thus controlling the efficiency of the

emitted THz pulses from the antenna. Therefore, the dependence of the THz radiation amplification of SI-GaAs PCAs on the variation of the Au-NPs concentration in the active excitation region has been demonstrated. Another advantage of PLD is its ability to direct the deposition of high-quality NPs in a large excitation area, which could be a novel solution to overcome the current limitations of generating higher-intensity THz pulses from large-aperture photoconductive antennas (LAPCAs). Furthermore, a new experimental approach for the generation of intense quasi-half-cycle THz pulses with variable polarization has been presented in this thesis. This experimental approach consists of using different thicknesses of phase masks on interdigitated large aperture photoconductive antennas (ILAPCA) having a specific design with alternating vertical and horizontal electrodes. Therefore, by changing the thickness of the phase mask, we can tune the polarization state of the radiated THz pulses from linear to quasi-circular on demand.

Table of Contents

LIST OF FIGURES

LIST OF TABLES

LISTE OF ABBREVIATIONS

LISTE OF PUBLICATIONS

- X. Ropagnol**, E. Isgandarov**, X. Chai, S. M. Raeis-Zadeh, S. Safavi-Naeini, M. Reid, F. Blanchard, and T. Ozaki, "Generation of intense sub-cycle terahertz pulses with variable elliptical polarization," Appl. Phys. Lett. **120**, 171106 (2022).

- **E. Isgandarov**, X. Ropagnol, M. Singh, and T. Ozaki, "Intense terahertz generation from photoconductive antennas," Front. Optoelectron. 2020 141 **14**, 64–93 (2021).

- X. Ropagnol, M. Matoba, J. E. Nkeck, F. Blanchard**, E. Isgandarov**, J. Yumoto, and T. Ozaki, "Efficient terahertz generation and detection in cadmium telluride using ultrafast ytterbium laser," Appl. Phys. Lett. **117**, 181101 (2020).

- M. Singh, M. A. Fareed, A. Laramée, **E. Isgandarov**, and T. Ozaki, "Intense vortex high-order harmonics generated from laser-ablated plume," Appl. Phys. Lett. **115**, 231105 (2019).

- X. Ropagnol, M. Matoba, J. E. Nkeck, F. Blanchard, **E. Isgandarov**, J. Yumoto, and T. Ozaki, "Efficient terahertz generation and detection using CdTe crystal pumped by ultrafast Ytterbium laser," Int. Conf. Infrared, Millimeter, Terahertz Waves, IRMMW-THz 2019-September, (2019).

- A. Ovchinnikov, A. Savelev, A. Ushakov, C. M. Garcia-Rosas, **E. Isgandarov**, M. Agranat, O. Chefonov, T. Ozaki, X. Chai, and X. Ropagnol, "Observation of crossover from intraband to interband nonlinear terahertz optics," Opt. Lett. Vol. 43, Issue 21, pp. 5463-5466 **43**, 5463–5466 (2018).

CHAPTER 1 INTRODUCTION

Terahertz (THz) science and technology have witnessed significant progress over the past 30 years. Due to a lack of powerful tunable lasers and sensitive detectors, research, and development in this region of the electromagnetic spectrum, known as the THz gap, remained modest until the last two decades of the 20th century. The THz gap covers the entire electromagnetic spectrum at wavelengths lying between infrared and microwaves (10 μm- 300 μm), corresponding to a frequency range between 0.1 to 10 THz (Figure 1.1). Furthermore, the timescale associated with 1 THz ($\tau = \frac{1}{\nu}$) is equal to 1 picosecond (ps), which corresponds to a wavelength ($\lambda = \frac{c}{\nu}$, where c is the speed of light) of 300 μm, a wavenumber of 33 cm^{-1} ($k = \frac{1}{\lambda}$), photon energy ($E = h\nu$, where h is Planck's constant) of 4.1 meV, and an equivalent temperature ($T = \frac{h\nu}{k_B T}$, where k_B is Boltzmann's constant) of 47. 6 K [1].

Today, THz technology is in high demand in a broad range of applications, from fundamental science such as biochemical spectroscopy, solids materials, astronomy, and science of nanomaterials, to practical areas such as environmental science, pharmaceutics, agriculture, and security [2–6]. The advantages of the THz wave include its ability to transmit through objects that are opaque in the visible range, as well as its low photon energy of 1-100 meV, which is an important energy range for various materials and biomolecules. In addition, the non-ionizing and non-invasive characteristics of THz wave make it much safer for medical inspections compared to X-rays. These characteristics allow various imaging and spectroscopy applications with THz waves and thus make THz measurements a powerful tool for non-destructive testing [7–9].

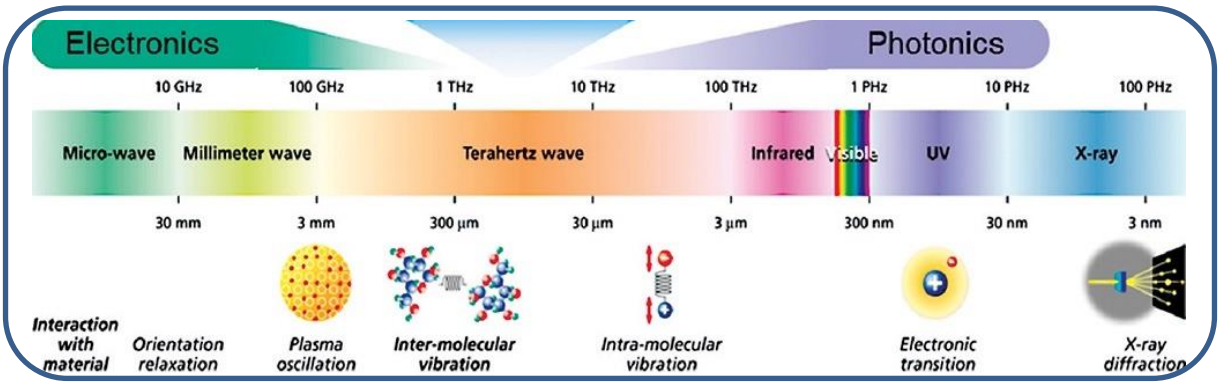

Figure 1-1 The electromagnetic spectrum representing THz range

1.1 SCOPE OF THZ PHOTONICS

Since the first demonstration of THz wave generation in time-domain spectroscopy (TDS) measurements in the late 1980s, THz technology has witnessed a significant advance due to the development of intense THz sources and more sensitive detectors [10]. Today, taking advantage of high-power tunable sources, such as synchrotron and free-electron lasers, back-wave oscillators, quantum cascade lasers (QCLs), optical laser amplifiers, and compact laser oscillators we can access versatile reflection and transmission mode spectrometers integrated into intense THz sources, and ultrafast, real-time THz imaging systems. Since THz radiation has shorter wavelengths than microwaves, it offers a higher spatial resolution and improved fingerprint spectrality. Further, with its low photon energies below the ionization threshold, THz radiation provides significant potential for the study of lattice vibrations, molecular rotations, spin waves, inner excitations of electron-hole pairs, and phonon vibrations in solid crystals and hydration states in biological systems [11–13]. In addition, owing to its highly directional, transient nature, compact THz sources have been widely used for many technological, and industrial applications, including medical treatment, information and communication technology, ultrafast computing, environmental monitoring, and non-destructive evaluation, pharmacy [14–19].

However, despite these remarkable advances, THz technology still needs further development of efficient THz sources capable of generating high-power broadband THz pulses with high peak-to-peak pulse stability, where shot-to-shot THz field amplitudes are stable. Indeed, the strong electric field associated with intense THz radiation can induce ultrafast modulation in the electric or magnetic fields in the picosecond time scale, which is much faster than we can achieve with conventional electronics. The study of these nonlinear phenomena has been made possible by the development of ultrafast nonlinear THz spectrometers. Another notable advantage of intense THz pulses is their associated high ponderomotive energy, which can accelerate electrons by increasing their kinetic energy when interacting with semiconductor materials [20,21]. Therefore, electrons acquiring sufficiently high kinetic energy can induce electric field-driven interval scattering in thin semiconductor layers [22]. For example, single-cycle THz pulses with a peak electric field of 10 MV/cm can give an electron ponderomotive energy reaching 100 eV, which is much higher than the energy required to separate an electron from a hydrogen atom and large enough to induce nonlinear transport phenomena such as impact ionization dynamics by inter-band and intra-band scatterings in the narrowband semiconductors.

Previous applications of intense THz pulses in spectroscopy studies include the demonstration of nonlinear absorption bleaching in n-doped InGaAs thin films using the

conventional Z-scan technique [23,24]. Similarly, by probing via intense THz pulses under the excitation of femtosecond optical pulses (optical pump/THz probe), the nonlinear behavior of intervalley carrier scattering in GaAs thin films was demonstrated. In addition, using THz pump/THz probe (TPTP) experiments, several non-linear phenomena, such as impact ionization and conductivity dynamics in indium antimonide (InSb) and graphene thin films grown by chemical vapor deposition (CVD) have been studied [25–27]. Furthermore, a series of studies on saturation absorption and the high harmonic generation (HHG) effect has previously been experimentally demonstrated in monolayer graphene and GaSe and InGaAs crystals under the excitation of high-intensity THz pulses using conventional TPTP experiments [28,29]. Finally, in recent nonlinear light-matter interactions related to high-intensity THz radiation, we can count a series of studies such as lattice (phonon) dynamics of crystals, control of vibrational resonance states of molecules, as well as the demonstration of the Higgs amplitude mode in Bardeen-Cooper-Schrieffer (BCS) superconductors and the Josephson plasmon in layered superconductors [30–33]. Despite these recent advances in the THz domain, the peak electric field of the intense THz pulses radiated from the conventional tabletop sources is limited to a few MV/cm. In addition, the spectra of the radiated THz pulses are limited to the low-THz range, using large-area structures, so far [28]. Therefore, to improve the radiation efficiency of the generated THz pulses and unveil many other interesting non-linear phenomena in materials, such as strong THz electric field-induced Kerr effect and self-focusing effects, it is necessary to improve the performance of conventional table-top sources by overcoming existing current technical limitations.

1.2 YTTERBIUM LASER SYSTEMS

Since most of the THz wave generation experiments in this thesis involve using a Ytterbium (Yb)-doped solid-state laser, the following section provides a brief overview of femtosecond Yb laser systems. Ytterbium is one of the most important rare earth materials used to manufacture high-quality laser oscillators and amplifiers. Belonging to the group of rare-earth metals, Yb plays a vital role in laser technology in its form of the trivalent ion Yb^{3+}, which is used as an active dopant in a range of host materials, including crystals, glasses, and ceramics and is also often used in active optical fibers [34]. Yb ions have a simple electronic level structure, with a single excited state manifold ($F_{5/2}$) that can emit visible or near-infrared photons to the ground state ($F_{7/2}$) manifold (Figure 1-2) [35]. Transitions between different sublevels of the ground state and excited state are involved in pumping and amplification. The sublevels would be energy degenerate in a vacuum, but this degeneracy is eliminated by the electric field in the crystal lattice.

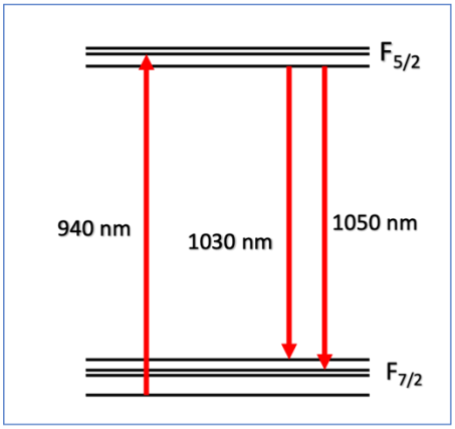

Figure 1-2 Typical pump and laser transitions and energy levels of Yb3+ ions in Yb: YAG [68].

The main advantage of Yb-doped materials for laser technology is their low quantum defect (<10%), which results in low heat deposition. In addition, the significant improvement in heat removal capability due to the surface-to-volume ratio from the active medium based on thin disk, fiber, or slab-based materials allows the Yb-lasers to be pumped by efficient high-power diodes [36,37]. Besides this performance, other practical advantages such as simplicity, compactness, cost-effectiveness, and low maintenance make Yb-lasers technology highly attractive in many applications such as material processing [38], medical [39–41], and military applications [42,43], sensing, coherent telecommunication [44], and optical frequency-domain reflectometry [45]. Today, we can count various Yb-doped pulsed and continuous-wave laser systems that can reach multi-kilowatt levels, the output power of Yb-doped picosecond and sub-picosecond pulsed lasers with a modest number of bulk optics in the cavity has been limited to a few hundred watts [46]. In addition, commercially available Yb-doped regenerative amplifiers can

Specifications	HighQ2-IR	HighQ2-IR
Average Power	>1.5 W	>0.65 W
Wavelength	1045 ±8.0 nm	522 ±4.0 nm
Repetition Rate	63 MHz	
Pulse Energy	>24 nJ	>10 nJ
Peak Power	>80 kW	>35 kW
Beam Quality	TEM_{00}, M^2 <1.15	
Beam Diameter, at waist	0.8 mm	1.0 mm
Polarization	100:1, vertical	100:1, horizontal

Table 1-1 The specification of HighQ2-IR laser

generate significantly higher pulse energy and peak power levels, reaching 40 J and 100 MW, respectively. Besides the high-power laser sources mentioned above, there are Yb-based mode-locked laser oscillators, which provide ultrafast pulses in the 1020-1070 nm spectral range, with pulse widths of several hundred femtoseconds. In this case, the Yb-doped gain medium (bulk crystal or fiber) is directly pumped by an infrared diode laser. These lasers provide optical pulses having ultra-high peak power while operating at moderate average power levels (1-5 W). The commercially available air-cooled High-Q2 laser (from Spectra-Physics) used in our experiments is one of the Yb-doped solid-state oscillator systems that can deliver optical pulses with an average power of 1.5 W, with a higher repetition rate of 63 MHz at the central wavelength of 1045 nm. Table 1-1 summarizes some of the important specifications of the High-Q2 laser driven at the fundamental and second harmonic (SH) wavelengths [47]. This compact light source does not require thermoelectric and water-cooling systems. Also, with the reduced number of optical components such as lenses or mirrors in the cavity, these laser sources have the advantages of no adjustment, no maintenance, and high stability, which is unmatched by conventional lasers. In addition, they can be operated in harsh environments, with high tolerance to dust, shock, humidity, and temperature.

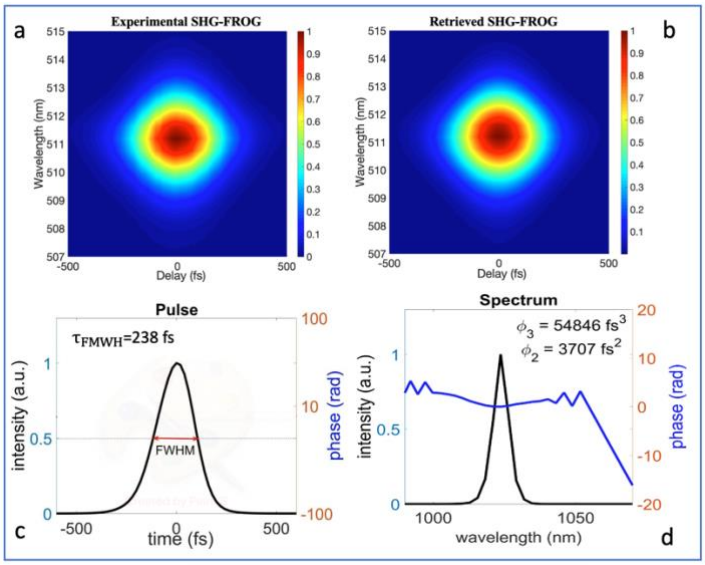

Figure 1-3 Characterization of the duration of optical pulses delivered by HighQ-2 laser using SH-FROG measurement

(a) Experimental and (b) retrieved FROG spectrogram of HighQ2 laser, (c) corresponding retrieved laser pulse in time domain, (d) intensity and phase in the spectral domain

To accurately characterize the pulse duration of the High-Q2 laser, we performed second harmonic generation and frequency-resolved optical gating (SHG-FROG) measurements. The measured spectrogram (Figure 1-3 (a)), and iteratively retrieved one (Figure (1-3(b)) are relatively

close to each other, affirming the validity of the characterization. The reconstructed temporal profile (Figure 1-3 (c)) reveals that the pulse duration of the High-Q2 laser is about 240 fs.

1.3 MOTIVATION AND OUTLINE

Photoconductive antennas (PCAs) are widely used devices for generating and detecting THz radiation [48]. THz-PCAs have unique characteristics such as compactness, higher optical-to-THz conversion efficiency while requiring relatively lower optical pump powers, and the ability to operate without complex cryogenic systems. These THz sources are especially appealing for applications outside the research labs due to their comparatively low cost and stable operation. Owing to these characteristics, PCAs have recently been employed in numerous time-domain spectroscopy (TDS) studies as emitters and detectors of pulsed THz radiation [49–53].

With a relatively narrow spectrum and a lower cut-off frequency, PCAs with large laser excitation areas can provide intense, sub-cycle THz pulses with central frequencies with several tens of GHz to a few hundred GHz [43]. Due to their associated higher ponderomotive energy, intense THz pulses generated by large aperture photoconductive antennas (LAPCAs) are excellent candidates for studying several nonlinear light-matter interaction processes such as interband and intraband carrier dynamics in n-doped materials, including impact ionization phenomena in undoped narrow bandgap semiconductors [54]. In addition, these THz pulses with extremely high field strength can provide outstanding advantages in controlling the macroscopic magnetization precession and spin degree of freedom in antiferromagnetic layers due to the induced strong magnetic field [55]. Furthermore, the recent advent of polarization state tunability control of intense THz pulses generated by large-aperture photoconductive antennas with interdigitated electrodes (ILAPCA) opens a new avenue for studying polarization effects in high-field light-matter interactions, such as circular dichroism and optical activities in chiral metamaterials [56,57].

However, despite the above-mentioned potentials, conventional PCAs exhibit several drawbacks related to thermal runaway, corona discharge, and dielectric breakdown, which limit the peak electric field of the radiated THz pulses and the overall performance of photoconductive emitters. As a result, the peak electric field of THz pulses emitted by these photoconductive sources is limited to a few hundred kV/cm. To this end, several studies have recently been reported on improving the THz radiation performance of PCAs. Encapsulating the antenna surface with a high-resistivity anti-reflection coating is one of the proposed solutions to enhance

photon absorption and high voltage breakdown limits [58,59]. In addition, performing high-quality ohmic contacts, and inserting a number of interdigitated electrodes in the active illuminated area are other alternative solutions for boosting the optical-to-THz conversion efficiency due to the improved applied bias fields and locally enhanced DC fields over the active excitation area by decreasing the average distance of the photo-excited charge carriers from the edges of the PCA electrodes [60,61]. Among these approaches, using wide-bandgap semiconductors (WBG-SCs) is one of the recent steps toward improving the THz radiation performance of LAPCAs. Since the intensity of the THz pulses radiated from PCAs increases linearly with the applied external bias field, semiconductors with high dielectric strength are recommended for fabricating such sources. It is also noteworthy to mention that large bandgap semiconductors exhibit higher dielectric strength, which is necessary to overcome the breakdown limit under strong bias voltages applied. Therefore, the wide bandgap semiconductors with short carrier lifetime, relatively high carrier mobility, and high dark resistance have been attractive for the fabrication of LAPCAs [62]. Recently, the LAPCAs integrated into some WBG-SC crystals have been utilized to generate intense sub-cycle THz pulses, by using optical pulses via the SH excitation of a Ti:Sapphire laser at 400 nm as the pump. The generated high-intensity sub-cycle THz pulses reached the maximum peak electric field corresponding to several hundred kV/cm. Such high-intensity THz pulses can strongly accelerate the carriers, due to their relatively high ponderomotive energy as high as 15 eV in vacuum [63]. Furthermore, ILAPCAs integrated into WBG-SCs are other alternative means to enhance the efficiency of the radiated THz pulses by applying a relatively lower bias voltage. Recently, the peak field strength of the radiated THz pulses from ILAPCA fabricated on a 4H-SiC crystal with a band gap of ~ 3.26 eV achieved up to 117 kV/cm when excited under laser pulses delivered by a sub-picosecond amplified KrF excimer laser at 248 nm [64]. The generated intense THz pulses had an energy of 11 μJ, with a narrow spectrum of 0.4 THz, which can strongly accelerate electrons through a high pondermotive energy of 60 eV in vacuum.

Despite this outstanding performance, one of the significant drawbacks of LAPCAs integrated into WBG-SCs is the limited photon absorption when used with conventional Ti:Sapphire lasers, which are one of the most widely used femtosecond laser sources with a central wavelength of 800 nm and corresponding photon energy of 1.55 eV. Although UV lasers with relatively high photon energy could be an alternative solution, their high cost and danger of handling decrease the appeal of this source for use in the THz PCA technology. On the other hand, although doubling the initial photon energy of intense femtosecond Ti:Sapphire laser pulses via SH excitation has been proposed as an alternative solution to improve the performance of LAPCAs, some semiconductors with better electrical and thermal properties, such as 4H-SiC, ZnO, GaN, and

diamond have limited photon absorption due to their larger bandgap than the 3.1 eV photon energy at 400nm [65–68].

Besides the abovementioned studies, the deposition of nanoparticles (NPs) in the active excitation area of PCA is one of the current promising approaches for enhancing the THz radiation intensity [69–72]. The increase of photocarriers in NP-embedded photoconductive substrates can be attributed to the local enhancement of the electric field of the femtosecond pump beam in the vicinity of deposited particles. Indeed, when the pump laser at a specific wavelength hits a host semiconductor decorated with metal NPs, the collective oscillation frequency of the surface electrons leads to a significant increase in photon absorption due to a drastic enhancement of the near field in the surrounding area of the deposited particles. Therefore, plasmons acquiring sufficiently strong near-fields tear the valence electrons from their valence bond, resulting in the generation of electron-hole pairs in the conduction and valence bands of the host substrate. Consequently, the increase in the density of generated photocarriers contributes to enhancing the efficiency of the THz radiation from the PCA due to increased current density.

By taking advantage of the enhanced photon absorption, the THz radiation performance of nano-decorated GaAs PCAs with various plasmonic NPs has been recently reported in [69,73–75]. The amplitude of THz pulses radiated from nanodecorated PCAs exhibited an amplification between 1.4 and 2 times compared to bare substrate integrated GaAs antennas when operated under the same optimum conditions at a pump laser wavelength of 800 nm. Although these early studies provide an essential solution to improve the performance of conventional PCAs, the efficiency of radiated THz pulses was only compared to one randomly nanodecorated substrate concentration. In addition, the previous methods proposed for preparing and depositing NPs require some thermal and chemical treatments. These treatments have some essential drawbacks, such as the non-uniform distribution and the control of the concentration of the deposited NPs, which is very important in small surface dimensions such as the photoconductive gap of PCAs [76]. In addition, chemical methods used for nanodecoration require precipitating toxic chemicals on the substrates and an additional purification process of the nanoparticles after the deposition process, which is difficult for large-scale production, long processing time, and high cost of the equipment for the processing [77].

Therefore, the pulsed laser deposition (PLD) method for the nanodecoration of GaAs-PCAs presented for the first time in our study allows the relatively simple and efficient formation of NPs using laser pulses. The PLD is a highly efficient physical method for in-situ nano-decoration of any material surface by highly-pure metallic or semiconducting NPs [78–80]. In comparison to

the chemical methods (such as sol-gel), the PLD technique stands out by its capacity to produce high-purity films of nanoparticles (without resorting to chemical precursors and hence no residual contamination), good controllability of the deposited amount of decorating material, ability to control the size and surface density of PLD-deposited nanoparticles, a prevalent congruent composition transfer (CST) from the ablated target to the NPs under specific ablation conditions, and a better attachment of the deposited NPs to the substrate (because of the high energy of the ablated species involved in the laser ablation process). The PLD opens the door to a simple and relatively low-cost method to improve the efficiency of micro-antenna for pulsed emission and detection of THz radiation. Furthermore, this straightforward laser-based method allows the deposition of uniformly sized NPs on large-area substrates, which is an essential solution for developing LAPCAs.

1.4 OVERVIEW OF THE THESIS

Taking into consideration the perspectives mentioned above, this thesis involves the first systematic studies of the THz emission performance of nanodecorated PCAs in the active excitation region using a Yb-doped femtosecond laser. To this end, we conducted a number of comparative studies on the peak field amplification of THz radiation as a function of the concentration of metallic gold nanoparticles (Au-NPs) deposited on SI-GaAs PCAs before and after decorating various numbers of ablated laser pulses (N_{LP}). Our investigations have shown that deposited NPs have a strong influence on the nonlinear amplification of the peak field of the radiated THz pulses from PCAs when excited by the second harmonic generation of the Yb-laser at 522 nm. Then, considering the drawbacks presented by PCAs deposited by metal NPs, we will present our preliminary studies on lead sulfide (PbS) nanoparticle decorated emitters that could be a plausible solution to overcome the short-circuit limitations presented by Au-NPs.

In addition to the above-mentioned studies, we have conducted a series of experimental investigations into the development of THz sources operating at the fundamental and second harmonic (SH) wavelengths of commercially available Yb lasers. To this end, we performed some comparative studies on the THz radiation efficiency of two organic and inorganic crystals through the optical rectification (OR) method when excited by a Yb-doped laser at the fundamental wavelength of 1045 nm, the conditions excited by the Yb -doped laser at the fundamental wavelength in a nitrogen-purged environment. Then, the fabrication and the study of the THz radiation performance of PCAs fabricated on two various semiconductor substrates will be presented when excited by the second harmonic generation (SHG) of the Yb-laser at 522 nm.

Afterward, a new method for controlling the polarization states of the THz pulses radiated from ILAPCA sources will be briefly introduced. We believe that the works presented in these will contribute to the development of Yb-laser-based sources. In addition, the progressive control of the density of NPs-deposited in the active excitation region of the antennas via PLD would allow tuning the photon absorption performance of large-aperture photoconductive emitters overcoming one of the main current limitations of intense THz pulse generation. Furthermore, the new method for controlling the polarization states of high-intensity THz pulses from the large-aperture photoconductor emitter with a specific interdigitated structure would be an advent solution for the studies of polarization-dependent high-filed light-matter interactions.

Considering the studies above, this thesis is organized as follows. Following the current chapter, which focuses on the general overview and scope of the THz technology chapter 2 will provide a brief introduction to methods for generating and detecting THz pulses using femtosecond tabletop laser systems. Along with theories of THz wave generation by optical rectification and two-color laser-induced plasma filament techniques, the theory of PCA-based THz sources will be presented in this section. We will also discuss THz wave generation from large-area excitation PCAs (LAPCAs) and interdigitated large-aperture photoconductive antennas (ILAPCAs) and promising materials for the fabrication of these sources. Then, the next section will briefly outline current techniques for coherent and incoherent detection of THz pulses.

Chapter 3 will be devoted to our first experimental works conducted on the THz emission performance of cadmium telluride (CdTe) and N-benzyl-2-methyl-4-nitroaniline (BNA) crystals in a nitrogen-purged environment via OR. The radiation performance of these THz emitters will be compared under the same conditions to be pumped by optical pulses delivered at the fundamental wavelength of the Yb laser at 1045 nm.

Our second experimental study, performed on the generation of high-intensity THz pulses with variable elliptical polarization from ZnSe ILAPCAs sources, will be presented in Chapter 4. The new method presented in this chapter allows tuning the polarization state of the generated half-cycle intense THz pulses from linear to circular, with the intermediate states described as having elliptical polarization over a quarter cycle.

Next, we will present our experimental studies performed on the fabrication and characterization of Yb laser-based photoconductive sources in Chapter 5. To this end, we will present the manufacturing process of semi-insulating gallium arsenide (SI-GaAs) and CdTe PCAs, as well as the THz radiation performance of these sources under SH excitation of the Yb laser at 522 nm.

Finally, in chapter 6, we will demonstrate further details of the PLD method used for the decoration of PCAs with NPs, as well as the theory explaining the enhancement of the THz radiation efficiency of antennas decorated with Au-NPs. The experimental results of THz radiation efficiency of nano-decorated antennas with different densities of Au-NPs will also be presented in this chapter. In addition, the advantage and preliminary studies performed on semiconductor NPs such as PbS.

Summarizing the results obtained during this research, the perspectives, and proposals of new types of NPs, as well as the advantage of nano-decoration of LAPCAs using the new PLD method to increase their THz radiation performance, will be concluded in Chapter 7.

CHAPTER 2 METHODS FOR GENERATING AND DETECTING OF EFFICIENT THZ RADIATION

Depending on the operating modes of the excitation lasers, tabletop THz sources are classified into two main categories. The first category includes THz sources excited by continuous-wave lasers, while THz sources driven by pulsed lasers constitute the second category. For each of these modes of laser operation, we can count several solutions for the generation and detection of THz waves using different methods. Among other continuous wave laser-driven sources, optical parametric oscillators OPOs [81], quantum cascade lasers (QCLs) [82], and semiconductor-integrated photo-mixers [83] are commonly used for THz wave generation. It is also worth mentioning that high average power continuous THz sources, such as free electron lasers (FELs), have been used for several nonlinear studies, including magnons, phonons, plasmons, and inter-subband transitions in solids [84]. However, although FELs have the potential to reach the peak electric field of radiated THz pulses of tens of MV/cm, their large size and complexity of the installation, as well as their high cost reduce the interest in these laser sources for practical applications [85]. In addition, these sources present simple physical scaling difficulties, losses in the metal walls, the need for strong magnetic and electric fields, and high electron current densities.

On the other hand, table-top pulsed femtosecond-laser-driven sources with relativistic higher peak power have been widely used for non-linear light-matter interaction in THz time-TDS studies. Pulsed femtosecond laser-driven tabletop THz sources have been classified into three main categories: optical rectification, laser-plasma interaction-based systems, and PCAs. Even though the peak amplitude of the radiated THz pulses generated from conventional high-power THz sources based on table-top femtosecond lasers ranges from a few hundred kV/cm to several MV/cm, these sources offer several practical advantages, such as direct probing characteristic resonances in the THz domain across a large tuning range. Further, these sources have simple alignment, and stable THz output [21,86,87]. Therefore, with respective pulse energy levels ranging from several μJ to mJ, such strong THz sources are capable to drive selected degrees of freedom of the matter in regimes well beyond the small perturbation limit. This property has enabled new applications in nonlinear spectroscopy and control material by driving the system into a target state.

In view of these characteristics, we briefly overview the mechanism of THz wave generation from current tabletop sources and detectors based on pulsed femtosecond lasers, and their respective advantages and limitations.

2.1 OPTICAL RECTIFICATION

Optical rectification (OR) is a straightforward technique for generating THz pulses which are based on the nonlinear interaction between femtosecond laser pulses and nonlinear crystals. In other words, when ultrashort laser pulses interact with a non-centrosymmetric crystal having second-order nonlinear properties, a photo-induced direct current (DC) field corresponding to the intensity of the optical pulses is generated from the difference frequency by all frequencies within the bandwidth of the femtosecond laser pulse. The schematic illustration of THz wave generation by OR is described in Figure 2-1. In nonlinear optics, the electrical polarisation *P* induced in the medium can be written as a power series of the electrical field *E*:

$$P = \varepsilon_0(\chi^{(1)}E + \varepsilon_0\chi^{(2)}EE + \varepsilon_0\chi^{(3)}EEE + \dots) \tag{2.1.1}$$

Where $\chi^{(n)}$ is the nth order susceptibility tensor of the material. On the other hand, radiated THz field from the OR process is proportional to the second-order nonlinear polarization in the near field, which is described by the following equations [88]

$$\mathrm{P}_{OR}^{(2)}(\Omega) = \varepsilon_0\chi^{(2)}(\Omega = \omega_2 - \omega_1; \omega_1 - \omega_2)\mathrm{E}(\omega_1)\mathrm{E}^*(\omega_2) \tag{2.1.2}$$

Here, Ω is the difference between two ($\omega_1\ and\ \omega_2$) frequency components of the optical pump pulse, $\mathrm{E}(\omega_1)\ and\ \mathrm{E}^*(\omega_2)$ are the respective amplitudes of the spectral components of the laser pulse. From Maxwell's equations, in the far field, THz electric field generated by OR is proportional to the derivative of second-order polarization, and given as follow [89]:

$$\mathrm{E}_{\mathrm{THz,far}}^{\mathrm{rad}}(\mathrm{t}) \propto \frac{\partial^2 \mathrm{P}}{\partial \mathrm{t}^2} \tag{2.1.3}$$

The efficiency of THz pulses generated via OR depends mainly on the orientation of the crystallographic azimuthal angle, the laser pulse energy, and the effective nonlinear coefficient of the crystal. The pulse energy of the radiated THz pulses from OR sources has a quadratic dependence on the intensity of the pump laser. On the other hand, some optical phenomena such as two-photon absorption and second harmonic generation can result in a reduction in the efficiency of the radiated THz pulses due to the depletion of the pump beam, as well as the

absorption of the free carrier of the THz beam. The phase matching between the optical group velocity and the THz phase velocity is another factor influencing the efficiency of radiated THz pulses via OR. Indeed, for an effective OR process, the group velocity of the optical pulse and

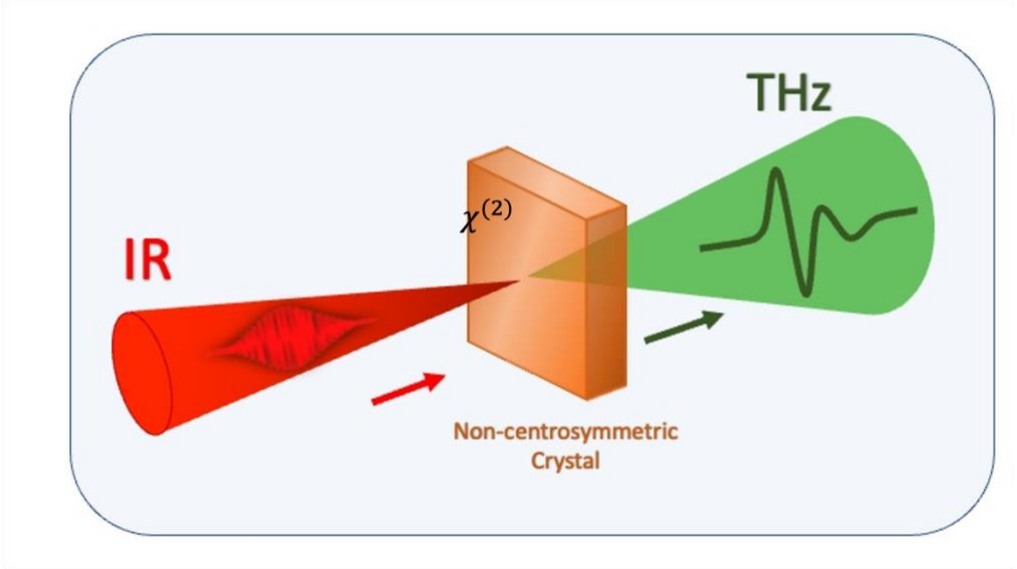

Figure 2-1 Schematic illustration of THz generation through optical rectification

the phase velocity of the THz wave must be respected over the entire crystal thickness. The equation 2.1.4 describes a perfect phase matching condition for the generation of THz pulses via OR.

$$k(\omega_2 + \Omega) - \mathrm{k}(\omega_2) = \mathrm{k}(\Omega) \tag{2.1.4}$$

where, k is the wave vector, ω_2 is the angular frequency of the pump beam, Ω is a particular frequency corresponding to the THz wave packet radiated from the crystal. Considering all these factors influencing the efficiency of THz radiation, Hebling *et al.* proposed a figure of merit to identify the performance of the most used OR crystals. The figure of merit (FOM) for crystals with low and strong THz absorption is defined as $\mathrm{FOM_A}$ and $\mathrm{FOM_{NA}}$, respectively, and given as follow [90]:

$$\mathrm{FOM_A} = \frac{4\mathrm{d_{eff}^2}}{\mathrm{n_{NIR}^2 n_{THz} \alpha_{THz}^2}} \tag{2.1.5}$$

$$\mathrm{FOM_{NA}} = \frac{\mathrm{d_{eff}^2 L^2}}{\mathrm{n_{NIR}^2 n_{THz}}} \tag{2.1.6}$$

here, d_{eff}^2 is the nonlinear coefficient of crystal, L is the length of the optical path, n_{NIR}, n_{THz} are crystal refractive indexes corresponding to the NIR and THz frequencies, α_{THz} is the absorption coefficient for the THz radiation.

Among OR-based THz emitters, zinc telluride (ZnTe) is a commonly used crystal for THz wave generation. Its relatively high figure of merit of 424 pm^2cm^2/V^2, and good phase matching conditions between the group velocity of the optical pump pulses and the phase velocity of the THz pulses at near-infrared wavelength range increases the interest in using the ZnTe crystal for the generation of intense THz pulses with Ti:Sapphire laser amplifiers and optical parametric amplifiers (OPAs). Therefore, the reported high-intensity THz pulses reached a maximum electric field strength of 160 kV/cm [91], and 570 kV/cm [92] when pumped at 800 nm, and 1030 nm,

Crystal	d_{eff} (pm/V)	n_{NIR}	n_{THz}	α_{THz} (cm^{-1})	FOM_A (pm^2cm^2/V)	Wavelength (nm)
DAST [98]	618	2.38	2.4	150	**4.99**	800
DSTMS [97]	230	2.19	2.2	~26	**29.6**	1500
BNA [97]	234	1.84	2.1	~10	**308**	1064
CdTe [98]	81.8	2.82	3.23	4.2	**58.06**	1064
ZnTe [98]	68.5	2.85	3.2	1.3	**424**	800
$LiNbO_3$ [98]	168	2.25	5.16	16	**16.8**	800

Table 2-1 Characteristics of commonly used nonlinear crystals for the generation of THz waves
Here, the value of the THz absorption coefficient for all transmitters has been considered at 1THz.

respectively. On the other hand, lithium niobate ($LiNbO_3$) crystal is another potential candidate for the generation of intense THz pulses at the excitation of 800 nm. With the tilted-front-pulse technique, the peak amplitude of the THz pulses radiated from this crystal reached up to ~3.3 MV/cm, due to its high electro-optic coefficient and high damage threshold [93]. This OR source has also been successfully used with Yb-doped laser amplifiers, and the peak field strength of the generated THz pulses has reached up to 400 kV/cm when excited by pulse energy of 400 µJ at 1026 nm [94].

Although many other OR-based THz emitters have recently been studied using ultrafast Ti:Sapphire lasers, it is also necessary to develop such sources for portable THz-TDS systems integrated into commercially available Yb-doped lasers, with unique characteristics. For this purpose, CdTe crystals with a thickness of 1 mm were used for the generation and detection of THz radiation using an Yb-doped laser amplifier and oscillator at wavelengths of 1025 and 1045 nm, respectively. The efficiency of the THz pulses radiated from the CdTe crystal was 5 times higher than that of the GaP emitter under the same optimal conditions. It should also be mentioned that the significant two-photon absorption process in CdTe crystal was observed when pumped with a 1026 nm amplified laser, which reduces the efficiency of the radiated THz pulses, even when pumped at low optical fluence [95]. On the other hand, efficient wavelength conversion, ultra-fast response on the sub-picosecond time scale, and high nonlinear susceptibility organic crystals have been widely used for applications in high-power THz wave generation [96]. From this perspective, the figures of merit of some effective organic and inorganic crystals with respect to the excitation wavelengths are summarized in Table 2-1 [97,98]. Here, the figure of merit of the crystals was calculated by considering the n_{THz}, and α_{THz} values at 1 THz. Among other organic crystals, DAST DSTMS, OH1, and BNA are commonly used for THz wave generation. Having a high conversion efficiency of 2.1%, high-intensity single-cycle THz pulses with a peak electric field of 1.35 MV/cm were generated when the DAST crystal is pumped by a Ti:Sapphire laser system-based OPA at 1550 nm. Also, extremely high-intensity THz pulses reaching a peak electric field of 83 MV/cm were generated by DMST and OH1 crystals when pumped by OPA-delivered 1550 and 1350 nm optical pulses. Furthermore, BNA crystals have recently been reported to generate intense THz pulses through OR using near-infrared (NIR) laser excitation. Due to its higher effective nonlinear coefficient, BNA is particularly attractive for THz wave generation at excitation wavelengths of 1 μm.

2.1.1 Study Of THz Radiation Characteristics Of BNA Crystals At Ytterbium Laser Wavelength

BNA is a yellow-coloured nonlinear organic crystal. Due to its excellent temporal stability at room temperature and effective nonlinear coefficient of 234±31 pm/V in the NIR region, BNA has been attractive for some industrial applications such as monochromatic THz sources and wavelength-tunable broadband optical crystals. In addition, a high damage threshold of 6.2 mJ/cm^2 presents a great advantage for using BNA under high excitation fluence driven by the laser with a pulse duration of 100 fs at 800nm. In addition, among the other most promising organic THz sources, a relatively low absorption loss of the pump beam and THz radiation, as

well as a suitable phase matching condition in the range of 1 μm, make BNA more attractive for use with commercially available Yb lasers.

Studies Year	Thickness (mm)	Peak THz field (MV/cm)	Bandwidth (THz)	Optical-to-THz conversion (%)	Pump beam parameters	Optical fluence (mJ/cm²)
Shalaby *et al.*, 2016 [99]	0.65	0.5	0.2-3	0.25	800 nm, 50fs 100 Hz	5.3
Zhao, *et al.*, 2019 [100]	0.2-07	10	0-7.5	0.8	1150-1550 nm 35 fs, 1kHz	4
Tangen, *et al.*, 2019 [101]	0.1-0.7	1.6	0-6			8
Roeder, *et al.*, 2020 [102]	0.6	4	0-3	0.2	800 nm, 100fs, 10Hz	8
Zaccardi, *et al.*, 2021 [103]	0.3-0.5	0.266 (without sapphire plate) 0.633 (with sap. plate	0.5-5.5	-	800nm, 100fs, 500 Hz	6.2 (without sapphire) 16 (with sapphire)
Mansourzadeh, *et al* 2022 [104]	0.65	0.029	0-7.5	0.12	1035 nm, 240fs, 540 kHz	-

Table 2-2 Recent works performed on the THz wave generation using BNA crystals via OR

The first demonstration of broadband THz wave generation in the BNA was performed by Miyamoto *et al.* Using a KTP-OPA, the generated THz pulses reached a maximum bandwidth between 0.1 and 15 THz when pumped with optical pulses with a duration and repetition rates of 7 fs and 100 Hz, respectively, at 900 nm. Following this study, several experimental studies have been conducted on THz wave generation from BNA via OR. Table 2-2 summarizes some of the experimental results on the generation of effective THz pulses from the BNA [99–104]. As illustrated in Table 2-2 the first demonstration of intense THz generation from BNA using a Ti:Sapphire laser amplifier was performed by Shalaby *et al.* [99]. The peak field of THz pulses from the 0.65 mm thick BNA crystal reached up to 500 kV/cm when pumped by a pulse duration and repetition rate of 50 fs and 100 Hz, respectively at 800 nm. Following this study, by increasing the optical fluence up to 8 mJ/cm^2 on the BNA, the peak amplitude of the radiated THz pulses was increased up to 4 MV/cm under the excitation of the pump beam with pulse duration and repetition rate of 100 fs and 10 Hz at 800 nm [102]. However, it should be mentioned that even though the THz pulses generated by the BNA reach a very high peak field, the corresponding bandwidth is limited to 3 THz, which is shorter than the bandwidth of the THz pulses generated when BNA is pumped at laser wavelengths ranging from 1150 to 1550 nm. Indeed, with a maximum optical-to-THz conversion efficiency of 0.8%, the bandwidth of the generated THz pulses was extended to 7.5 THz when a 2.9 mm thick BNA crystal was pumped at wavelengths

between 1150 and 1550 nm. However, when the excitation wavelengths increased towards 1550 nm, the bandwidth of the radiated THz pulses is reduced below 7 THz. This can be explained by the better phase-matching condition between the optical group velocity at 1150 nm and the phase velocity of the generated THz pulses from BNA. Furthermore, previous studies have shown that the thermal damage threshold of the BNA crystal can be improved by bonding a sapphire window with higher thermal conductivity. As a result, the peak field strength of the radiated THz pulses reached 1 GV/cm due to 2.8 times higher optical fluence with 16 mJ/cm^2. With a wider bandwidth extending to 7 THz, the high-intensity THz pulses with a maximum field strength of up to 1 GV/cm make the BNA an excellent THz source for Yb-doped femtosecond laser-based THz-TDS studies.

2.2 TWO-COLOR LASER-INDUCED PLASMA FILAMENT

Two-color plasma-based THz radiation is another commonly used method for generating intense THz pulses. As shown in Figure 2-2, this method is based on THz wave generation by focusing ultrashort laser pulses in a gaseous medium, such as air. In this method, the fundamental harmonics (FH) of strong laser pulses generate free carriers in the air while accelerating these

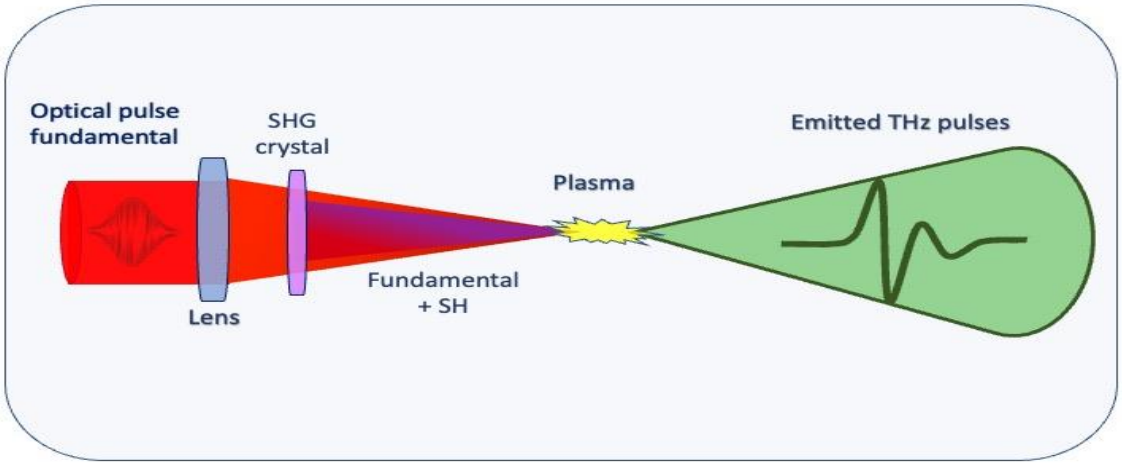

Figure 2-2 The experimental demonstration of THz wave generation using two-color laser induced air plasma technique

carriers by pulses on the second harmonic (SH) of this laser. In other words, the FH and SH fields propagate together to a common focal point, resulting in a two-color laser pulse that ionizes oxygen and nitrogen molecules at atmospheric pressure near the focus. This generates a plasma of electrons called "air plasma" which produces a macroscopic current leading to THz emission. The main advantage of this method is its ability to generate extremely broadband THz pulses with a spectrum extending up to 75 THz. Among other tabletop THz sources such as OR crystals and photoconductive emitters, air plasma induced by laser does not have a damage threshold.

Therefore, the THz pulses generated are expected to have a much higher intensity than those generated THz pulses by other tabletop sources.

Another advantage of this method is its remote detection ability, which largely avoids the propagation loss of the generated THz pulses. The first experimental demonstration of the intense THz generation in the laser-induced plasma medium was performed by Hamster *et al.* [105]. In this study, intense laser pulses with energy and duration of 50 mJ and 120 fs, respectively were focused on a helium gas to generate THz pulses. The origin of the intense THz pulses generated in this specific configuration has been demonstrated by the acceleration of electrons driven by ponderomotive forces. However, this method induces a conical THz wave emission, which makes the detected THz energy relatively low. Following this study, Löffer *et al.* proposed a new technique to avoid conical THz emission from the laser-induced filament by applying a DC current to the focal position of the femtosecond laser in the vertical propagation direction [106]. In this case, the generation of THz waves originates from the current created by the acceleration of ionized electrons, inside the plasma, by the static electric field. Similar to the PCAs, the amplitude of the THz electric field emitted by the laser filament increases linearly with the amplitude of the static electric field applied. The main limitation of this technique is its low sensitivity due to the use of high-order non-linearity and the need for critical alignment.

2.2.1 Theoretical Concept

Another experimental approach for the generation of THz pulses from the laser filament is based on the mixing of the fundamental infrared (IR) optical pulses with its second harmonic. In this configuration, the efficiency of the generated THz pulses is four times higher than that obtained by the previous methods based on the acceleration of the ionized electrons by the ponderomotive force. Several theories have been proposed to explain the principle of THz wave generation by two-color plasma [107,108]. Kim *et al*. proposed that THz wave generation results from photo-current induced during gas ionization. The generation of a directional current in a centrosymmetric medium such as a gas or plasma only occurs if the spatial symmetry of the medium can be broken. First, free electrons are generated from tunneling ionization. In this study, the superposition of the fundamental frequency (ω) of the ultrashort laser pulse and its second harmonic (2ω) is responsible for the generation of THz pulses, resulting in the movement of electrons in a symmetry-breaking electric field. Therefore, the temporal variation of the current density in the plasma leads to the electric field of the THz radiation, which is expressed as follows:

$$E_{THz} \propto \frac{\partial J}{\partial t} = e n_e a = \frac{n_e e^2}{m_e} E_{laser} \tag{2.2.1}$$

were, e and m_e is the charge and effective mass of the electron, a and n_e are the acceleration and density of the electrons, respectively. The current in equation 2.2.1, is expressed as follows:

$$J = -e n_e v_e \tag{2.2.2}$$

were, v_e is the average velocity of the electrons. E_{laser} is the electric field of the mixed two-colour laser, and is described by the following expressions:

$$E_{laser} = (E_\omega \cos(\omega t) + E_{2\omega} \cos(2\omega t + \theta)) \times e^{-\frac{t^2}{t_p^2}} \tag{2.2.3}$$

where, $E_\omega, E_{2\omega},$ and t_p are given as follow:

$$E_{\omega,2\omega} = \sqrt{\frac{2I_{\omega,2\omega}}{c\varepsilon_0}} \tag{2.2.4}$$

$$t_p = \frac{\tau}{\sqrt{2\ln 2}} \tag{2.2.5}$$

where, ω and 2ω are angular frequencies of the fundamental and second harmonic waves, E_ω and $E_{2\omega}$ are their respective amplitudes, I_ω and $I_{2\omega}$ are the corresponding intensities, θ is the relative phase between, ω and 2ω, c is the speed of light, τ is the pulse duration of the laser, and ε_0 is the permittivity of air. As we can see from equation 2.2.1, the radiated THz field depends on the density of the electrons generated within the plasma. To this end, many studies were performed to determine the choice of gas and the pressure that would improve the photoionization and thus the generation of THz waves. For example, Thomson *et al.* have shown that the increase in the plasma volume has a significant influence on the efficiency of THz generation [109]. Another method has shown that by increasing the length of the laser-induced plasma, it is possible to improve the THz generation efficiency due to a better directivity of the THz pulses generated in the elongated filament [110]. Furthermore, recently, from the two-color filaments generated by

mid-infrared femtosecond laser pulses at 3.9 μm, with 2.36% higher optical-THz conversion efficiency, the peak field strength of 100 MV/cm was achieved [111]. This peak field strength is the highest value obtained experimentally in THz pulses from tabletop sources. Another notable technique for enhancing THz pulses generated via a two-color plasma is to apply an external magnetic field to the gas in the vertical direction of beam propagation. A recent theoretical study has shown that a strongly magnetized helium plasma using magnetic fields higher than 100 T can significantly enhance the peak field strength of the radiated THz pulses up to 1 GV/cm [112].

2.3 TERAHERTZ WAVE GENERATION FROM PHOTOCONDUCTIVE ANTENNAS

This section reviews the previous and recent studies on generating THz pulses from photoconductive sources. More specifically, we will examine generating intense THz pulses from PCAs, which we have discussed previously in [113]. Therefore, the theory of THz generation and recent works performed on photoconductive antennas with the large aperture PCA (LAPCA) with large aperture dipoles and interdigitate electrodes will be mainly introduced. We will first discuss the fundamentals of THz generation from PCAs. The critical parameters for improving the peak intensity of THz radiation from LAPCAs will be summarized. We will then describe the saturation and limitation process of LAPCAs along with the advantages and disadvantages of working with wide bandgap semiconductor substrates. Then, we will explain the evolution of LAPCA with interdigitated electrodes, which allows one to reduce the photoconductive gap size, and thus obtain higher bias fields while applying lower voltages. We will also describe recent achievements in intense THz pulses generated by interdigitated LAPCAs based on WBG-SCs driven by amplified lasers.

2.3.1 Theoretical Concept

The development of terahertz (THz) radiation sources based on PCAs has progressed with the emergence of ultrafast Ti:Sapphire lasers. The first demonstration of free-space pulsed THz generation using PCAs was reported in 1984 [114]. In this study, two identical PCAs with coplanar strip line electrodes with a gap size of 10 μm were fabricated on Silicon-on-sapphire (SOS) substrate and placed opposite each other. To generate and detect THz pulses, a mode-locked ring dye laser with pulse energy and duration of 50 pJ and 100 fs, respectively, at a repetition rate of 100 MHz, was used to pump the PCA emitter and detector. The measured far-infrared radiation had a temporal width of 1.6 ps full-width at half maximum. There have been various examples of THz generation, detection, and application using PCAs. They are very

compact, have high optical-THz conversion efficiency, and can generate sub-cycle THz pulses with relatively high peak powers while being pumped with relatively low optical power.

The principle of THz wave generation from LAPCA can be described by the current surge model. A femtosecond laser pulse hits a semiconductor crystal on which metal electrodes have been deposited, and a bias voltage is applied. Photons are absorbed by the substrate, exciting carriers from the valence band to the conduction band. The bias field accelerates these free carriers, generating a photocurrent. The variations of the photocurrent density on the picosecond scale generate THz radiation in the reflection and transmission directions of the LAPCAs. The relation between the time-dependent photocurrent *J(t)* and the radiated near field E_{near} is given by the following equation.

$$J(t) = \frac{(1+\sqrt{\varepsilon_r})}{\eta_0} E_{near}(t) \tag{2.3.1}$$

Here, η_0 is free impedance, ε_r is the permittivity of relative material. From Ohm's law, we can extract the photocurrent as

$$J(t) = \sigma_s(t)(E_b + E_{near}(t)) \tag{2.3.2}$$

Here, $\sigma_s(t)$ is the surface conductivity of the PCA, and E_b is the bias electric field applied across the antenna electrodes. The conductivity is, in turn, proportional to the mobility and density of electrons and holes. Here we make an approximation by considering only the electron mobility, which is constant during the duration of the increase of the current density. In this case, we can express the current density as follows:

$$J(t) = e\mu n(t) \tag{2.3.3}$$

Here, e is the charge of the electron, μ is electron mobility, and $n(t)$ is the time-dependent electron density. Since we are using a femtosecond laser pulse for PCA excitation, the electron density will increase on the timescale of the femtosecond laser and then decrease on a timescale proportional to the recombination of the charge carriers within the antenna substrate. Therefore, we can write the equation (2.3.3) as:

$$\sigma_s(t) = \frac{e(1-R)\mu}{h\nu} \int_{-\infty}^{\infty} I_{op}(t') \exp\left(\frac{t-t'}{\tau_c}\right) dt \tag{2.3.4}$$

Here, R is the reflectivity of the antenna substrate at the given laser wavelength, hv is the photon energy, I_{op} is optical intensity, and τ_c is the carrier recombination time. Also, if we consider equation (2.3.2) in equation (2.3.1), we can obtain a new expression for $E_{near}(t)$ as follows:

$$E_{near}(t) = -E_b \eta_0 \frac{\sigma_s(t)}{\sigma_s(t)\eta_0 + (1+\sqrt{\varepsilon_r})} \tag{2.3.5}$$

From equation (2.3.5), we can see that the radiated near field E_{near} is linearly proportional to the bias electric field E_b. Also, the scaling of E_{near} is hyperbolically proportional to the surface conductivity. Therefore, we can express the maximum radiated near field E_{near}^{max}, as follows.

$$E_{near}^{max} = -E_b \eta_0 \frac{\sigma_s^{max}}{\sigma_s^{max}\eta_0 + (1+\sqrt{\varepsilon_r})} \tag{2.3.6}$$

Here, σ_s^{max} is the maximum surface conductivity. In our case, the maximum surface conductivity occurs at the end of the absorbed laser pulse, just before carrier recombination. From the equation (2.3.4), we can write the maximum surface conductivity as

$$\sigma_s^{max} = \frac{e(1-R)\mu F_{opt}}{hv} \tag{2.3.7}$$

Here, F_{opt} is the optical fluence. By substituting the equation (2.3.7) in (2.3.6), we can express E_{near}^{max} as follow:

$$E_{near}^{max} = -E_b \frac{F_{opt}}{F_{opt} + \frac{hv(1+\sqrt{\varepsilon_r})}{e(1-R)\mu\eta_0}} = -E_b \frac{F_{opt}}{F_{opt} + F_{sat}} \tag{2.3.8}$$

Here, F_{sat} is the saturation fluence, which is inversely proportional to the mobility of the electrons.

$$F_{sat} = \frac{hv(1+\sqrt{\varepsilon_r})}{e(1-R)\mu\eta_0} \tag{2.3.9}$$

From equation (2.3.8), we can see that the radiated electric field in the near field has a hyperbolic growth with the optical fluence (the laser energy per unit area). Therefore, when we increase the optical fluence, we reach a saturation regime where the radiated near field saturates with the optical fluence. From a physical point of view, when the optical fluence is low compared to the saturation fluence, the radiated near field increases almost linearly. However, when the optical fluence is higher, the amplitude of the radiated near field saturates. We can note that the direction

of the radiated near field has the opposite direction of the bias electric field. From a physical point of view, under the latter condition, when the amplitude of the radiated near field is comparable to the amplitude of the bias electric field, it screens the bias electric field itself, which causes the saturation of the radiated near field. When LAPCAs are operated in the saturation regime, the only option to increase the radiated near electric field is to apply a higher bias field. We can express the relation between the far field and bias applied voltage as follows:

$$E_{far}(t) \propto \frac{\partial J}{\partial t} \propto E_b \frac{\partial n}{\partial t} \tag{2.3.10}$$

The optical-to-THz conversion efficiency of the LAPCA can be expressed as follows:

$$\eta = \frac{\tau_{THz} E_b^2}{2F_{opt}\eta_0}\left(\frac{F_{opt}}{F_{opt}+F_{sat}}\right)^2 \tag{2.3.11}$$

Here, τ_{THz} is the duration of the THz pulse. As shown in equation (2.3.11), the efficiency of optical-to-THz conversion is inversely proportional to the optical fluence and exhibits quadratic behavior with respect to the external bias field. We can express the maximum efficiency of the optical-THz conversion as follow when the optical fluence is equal to the saturation fluence.

$$\eta_{max} = \frac{\tau_{THz} E_b^2}{8F_{sat}\eta_0} \tag{2.3.12}$$

The energy of the THz pulses can be expressed as follows:

$$W_{THz} = \eta \times W_{opt} = \eta \times A \times F_{opt} \tag{2.3.13}$$

Since the maximum energy of the THz pulses has a linear behaviour to the maximum conversion efficiency of the LAPCA, it can be expressed as

$$W_{THz}^{max} = \frac{A\tau_{THz} E_b^2}{8\eta_0} \tag{2.3.14}$$

Here, W_{THz}^{max} is the maximum energy of the THz pulses radiated from the LAPCA, and A is the area of the optical beam, which is considered equal to the excitation surface of the LAPCA. From the equation (2.3.13), we can see that the maximum energy of the radiated THz pulses from the LAPCA only depends on the excited area of the antenna and the square of the applied bias field applied across the electrodes. Furthermore, the energy of the THz pulses radiated from a PCA is extracted from the bias voltage rather than from the optical pump power. This characteristic is

also advantageous for using PCAs with laser oscillators, which allows obtaining a high optical-THz conversion efficiency while using relatively low optical energy. Compared to other tabletop THz sources, such as nonlinear crystals based on optical rectification, this unique characteristic makes PCAs very special. Studies on THz generation and detection have been greatly enhanced by the advent of femtosecond Ti:Sapphire lasers, one of the most widely used femtosecond lasers since the 1990s, with a central wavelength of 800 nm and corresponding photon energy of 1.55 eV. Since then, taking advantage of the characteristics of the Ti:Sapphire laser and using semiconductors with a band gap below 1.55 eV, many works have been performed on the fabrication and development of PCA. With their unique properties, such as relatively high dielectric strength, high carrier mobility, and ideal band gap, GaAs has rapidly emerged as an extensively used substrate for the fabrication of PCAs over the past 20 years. These PCAs have been widely used both as THz emitters and detectors, leading to new functionalities such as THz-TDS, which was first demonstrated in 1990 by Grischkowsky *et al.* Other applications, such as imaging, security control, non-destructive testing, and telecommunications, are also being developed. These applications typically use photoconductive microstructure sources, which allow the use of much lower bias voltages. In addition, these sources can be pumped by oscillator lasers with optical pulses having energy levels in the order of nano-joules with a high repetition rate, which allows for generating THz pulses with a higher average power and measurements with a superior dynamic range. Although the fabrication of these photoconductive sources requires high-precision photolithography technology, they promise to achieve optical-to-THz conversion efficiency ranging from 10^{-4} to 10^{-3}. Furthermore, by taking advantage of extreme lithography technology, fabricated photoconductive emitters with nano-plasmonic electrodes, such as nano-islands and nano-rods, can generate broadband THz radiation with an optical-to-THz conversion efficiency of 7.5%, which is the highest conversion efficiency recorded to date [115]. Further, the amplified laser-driven LAPCAs are capable of generating strong THz pulses with high peak power, offering a new field of study, such as the nonlinear interactions between matter and strong THz waves. Several such nonlinear and non-resonant effects have been unveiled, such as the ionization of Rydberg atoms, absorption bleaching and high-frequency THz generation. Indeed, these photoconductive sources with a large excitation area typically generate quasi-half-cycle asymmetric THz pulses composed of a strong positive peak followed by a long but weak negative tail. The main frequency component corresponding to these THz pulses is in the lower part (<1 THz) of the spectrum. These two unique properties distinguish LAPCA as a special THz source among other high-field tabletop sources driven by amplified lasers.

2.3.2 The THz Wave Generation from LAPCAs

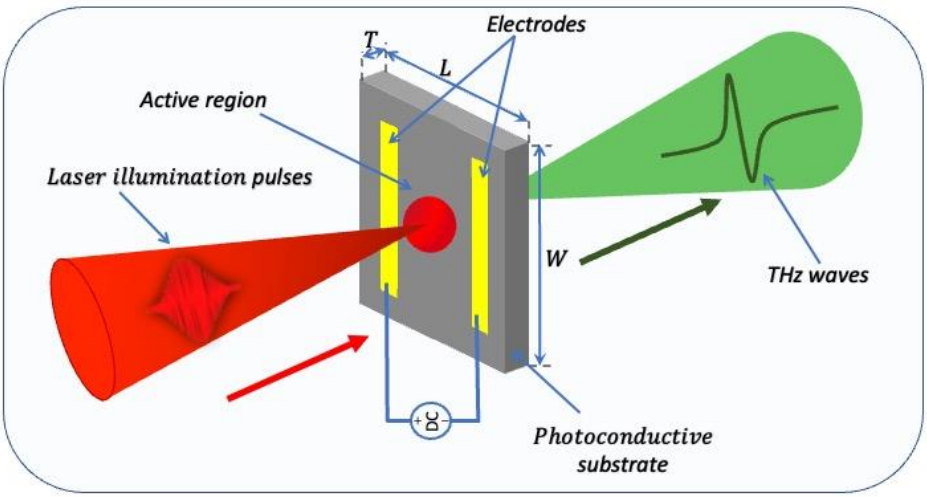

Figure 2-3 Systematic representation of a typical large-aperture photoconductor emitter

Increasing the total exciting area of conventional photoconductive emitters while maintaining the same optical fluence provides a simple way to improve the peak electric field of radiated THz pulses. The emitting surface of LAPCAs can typically range from a few hundred mm^2 to a few tens of cm^2. The gap size between the electrodes of these photoconductive emitters varies between 1 mm and 1 cm, which is much larger than the wavelength of the generated THz pulses. With a relatively smaller gap size than LAPCAs, ranging from a few hundred μm to 1 mm, the semi-large photoconductive emitters have almost the same inter-electrode distance relative to the wavelength of the emitted THz pulses. However, the theory of THz wave generation from LAPCAs remains the same as for semi-large PCAs. The schematic diagram of conventional LAPCAs is shown in Figure 2-3. The advantage of working with LAPCAs having a large surface area is to avoid saturation and thermal damage limitations by expanding the beam size of the high-energy femtosecond pump lasers. Therefore, a larger number of carriers will be injected, resulting in a larger radiated electric field. Furthermore, unlike micro-dipole photoconductive emitters, LAPCAs are not affected by the space charge screening effect, which is one of the saturation effects limiting the intensity of THz pulses.

This effect can be explained by the separation of free charges (electron-hole) in the semiconductor. These free carriers are accelerated by the applied bias field, thus creating a static Coulomb field, which is in the opposite direction of the bias field and finally causes a partial screening of the applied bias fields during a picosecond timescale. Previous studies based on Monte Carlo simulations have shown that when the inter-electrode spacing is larger than 100 μm,

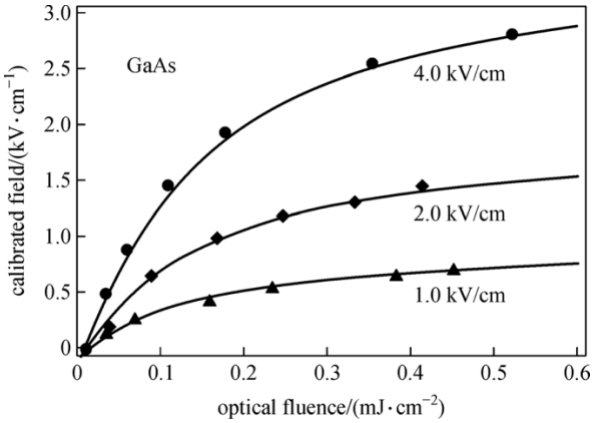

Figure 2-4 Calibrated radiated field as a function of optical fluence from 0.5 mm gap GaAs at bias fields of 4.0, 2.0, and 1.0 kV/cm [126]

the space charge screening effect is almost negligible in GaAs PCAs. In addition, some previous studies have shown that the choice of the semiconductor substrate significantly impacts the performance of LAPCAs. For the generation of high-intensity THz pulses, it is typically beneficial to work with a semiconductor substrate with high dielectric strength, excellent thermal properties, and high carrier mobility. Following this perspective, the generation of intense THz pulses using a LAPCA was first demonstrated by You *et al.* [116]. The THz pulse energy generated by a GaAs LAPCA with a pair of 3.5 cm x 3.5 cm aluminum electrodes deposited on the backside of the substrate reached up to 0.8 μJ when excited with an optical fluence of 40 μJ/cm^2 and an applied bias field of 10.7 kV/cm. With an effective optical-THz conversion efficiency of 1.6 x 10^{-3} and a calculated peak THz electric field of 150 kV/cm, this source can be considered one of the most efficient LAPCAs to date. Using a LAPCA fabricated on a low temperature (LT) grown GaAs substrate, another early demonstration of intense THz wave generation was performed by Darrow *et al.,* [117]. With an inter-electrode distance of 500 μm, this photoconductive emitter was illuminated by a mode-locked ring dye laser with pulse energy and duration of 8 μJ and 70 fs, respectively, at a central wavelength of 618 nm. The waveform of the THz pulses radiated by the antenna was a quasi-half-cycle with a duration (FWHM) of 600 fs. On the other hand, as we can see in Figure 2-4, the LAPCA shows a strong saturation behavior in the peak electric field of the radiated THz pulses, under the excitation of an optical fluence of 1 mJ/cm^2, with an increase in the applied bias voltages from 1.0 to 4.0 kV/cm [117]. Furthermore, under this fixed optical fluence of 1 mJ/cm^2, pushing the applied bias field up to 5 kV/cm caused thermal damage to the LAPCA. Moreover, experimental studies on LAPCAs integrated into semi-insulating (SI) GaAs, InP, and ZnSe substrates have shown that all types of antennas exhibit screening of the bias field when excited at optical fluences higher than the saturation fluence with photon energy above the band gap of the semiconductor substrate. From this point of view, we can see that increasing the

CRYSTAL	E_G eV	E_C kV·cm^{-1}	μ cm^2/V·s	τ_c ps	ρ Ω·cm^{-1}	K W·cm^{-1}·K^{-1}
SI-GaAs	1.44	<10	9500	2-10	10^6-10^8	0.27
LT-GaAs	1.44	10	150-200	0.3-1	10^6	0.27
Diamond	5.46	2000	2800	-	10^{11}-10^{18}	25
GaN	3.40	300	1250	> 150	> 10^8	1.3
ZnSe $_{mono}$	2.67	60	300-600	> 500	10^{12}	0.18
6H-SiC	3.23	>500	200-300	1000	> 10^{12}	3.7
4H-SiC	3.02	1000	800	< 1000	< 10^{12}	3.7

Notes: E_G, bandgap; E_C, material dielectric strength; μ, carrier mobility; τ_c, carrier lifetime; ρ, resistivity; K, thermal conductivity

Table 2-3 Important parameters of semiconductors used for the fabrication of PCAs

optical fluence drives the THz electric field screening. However, working with LAPCAs in the screening regime has the advantage of having less fluctuation in the radiated THz field. This is particularly evident when LAPCAs are pumped by a very low repetition rate amplified laser. In this case, one way to increase the intensity of the THz pulses is to increase the bias field. Another recent theoretical study has shown that applying an external magnetic field to the electrodes in the parallel direction is another effective solution to increase the maximum intensity of the THz pulses radiated by the LAPCA [118].

2.3.3 Parameters Influencing the Performance of PCAs

In this section, we will describe some of the parameters that influence the performance of LAPCAs. To this end, in Table 2-3 we summarized the essential parameters of some semiconductors that have already been successfully used to fabricate LAPCAs to generate intense THz pulses. Where E_G, and E_C are the semiconductor substrate's bandgap and dielectric strength, μ and τ_c are carrier mobility and lifetime, ρ and K are the resistivity and thermal conductivity, respectively. These semiconductors have common characteristics such as high dielectric strength, higher carrier mobility, and good thermal conductivity.

2.3.3.1 Bandgap

The bandgap of the semiconductor is probably the most important parameter when choosing a substrate for the fabrication of LAPCA. Indeed, the bandgap determines the wavelength of the laser that we can use to generate THz radiation by the photoconductive

emitters. To significantly improve photon absorption, the photon energy of the laser pulse must be slightly higher than the bandgap of the photoconductive substrate. This will provide an efficient absorption with high quantum efficiency, but also, the free carriers will be generated at the bottom of the conduction band, where the mobility of the carriers is the highest. Another parameter we need to consider is the dielectric strength (E_C), which has an empirical relationship with the bandgap (E_G) of the material as follows

$$E_C = 1.36 \times 10^7 \left(\frac{E_G}{4}\right)^2 \tag{2.3.15}$$

As we can see in equation 2.3.14, a slight increase in the energy bandgap will lead to a strong increase in the dielectric strength. Since the radiated peak electric field has a linear behavior with the bias electric field applied, this parameter is essential for LAPCA. From equation 2.3.14 one can see that it is advantageous to work with semiconductor substrates having a large bandgap when fabricating LAPCAs. Another parameter related to the bandgap is the material dark resistivity. Indeed, if the bandgap of a semiconductor is broader, its intrinsic carrier concentration will be low, but the dark resistivity will be higher. Since LAPCAs require a high voltage, which is applied primarily during the on-state of the photoconductive switch but also during the off-state if a high-voltage pulse generator is used, the high dark resistivity will limit the high-voltage-induced current leakage during the off-state of the photoconductive switch, thus reducing the heating of LAPCAs. Recently, several wide-bandgap semiconductors such as gallium nitride (GaN), zinc selenide (ZnSe), zinc oxide (ZnO), and silicon carbide (SiC) have been experimentally tested as substrates for LAPCA for intense THz generation.

2.3.3.2 Carrier mobility

Carrier mobility is the second important parameter that should be taken into consideration. Indeed, in theory, carrier mobility does not affect the maximum intensity of THz pulses radiated from LAPCAs. However, as shown in Equation 2.3.12, since the maximum efficiency is linearly proportional to the carrier mobility, the latter will have an essential impact on the maximum efficiency of LAPCAs. A further effect of the high carrier mobility is that the saturation fluence of the semiconductor will be higher, thus requiring higher optical energy to reach the screening regime. On the other hand, when working with semiconductors with low carrier mobility, the increase in THz intensity can be compensated by increasing the energy of the driven laser, allowing more carriers to be injected to achieve the same current density.

Some simulations show that substrates with higher electron mobility do not exhibit an increase in THz intensity [119–121]. Experimentally, it is challenging to have the same substrate with the same characteristics with only a difference in carrier mobility. The closest example we can cite is probably LT-GaAs versus SI-GaAs. The difference in carrier mobility is 200 $cm^2/V{\cdot}s$ versus 8500 $cm^2/V{\cdot}s$. Even though some other parameters (such as the carrier lifetime) also differ, the experimental results are truly intriguing. It was shown that using low optical power or fluence, the SI-GaAs photoconductive emitter was more efficient and radiates a higher THz electric field than the LT-GaAs PCA. However, by increasing the laser energy (power), while the SI-GaAs were already working in the THz screening regime, the electric field radiated by the LT-GaAs PCA increased and was slightly larger [122,123]. Another important parameter to take into consideration is the fact that the mobility of carriers, when injected from the valence band to the conduction band, rarely reached the steady state, where the mobility of carriers is the highest. For example, it was found that for excitations of 815 nm from a dye-amplified laser, the effective carrier mobility was found to be 430 $cm^2/V{\cdot}s$ in SI-GaAs LAPCA [124], which is significantly less than the steady-state carrier mobility of GaAs (8500) $cm^2/V{\cdot}s$. This was attributed to the generation of hot electrons and the electron scattering process.

2.3.3.3 Carrier recombination time

Carrier recombination time is another parameter that influences the performance of PCAs. As discussed in the previous section, the THz fields radiated in the far field are proportional to the time derivative of the photocurrent density induced inside the PCA. Figure 2-5 illustrates the current density and the intensity profile of the femtosecond optical pulse as a function of time

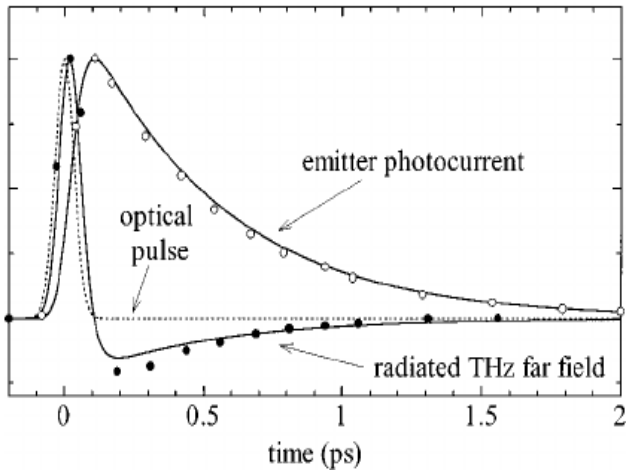

Figure 2-5 Calculated photocurrent, the amplitude of the radiated electric field and the laser pulse shape as a function of time [125].

inside a PCA, as well as the temporal profile of the electric field of the THz pulse propagating in the far-field [125]. As can be seen in Figure 2-5, in an ideal case, the temporal profile of the photocurrent reaches its maximum value at the end of the optical pulse duration. On the other hand, carrier recombination is the main dominating factor that influences the decay time of the photocurrent. The temporal profile of the THz pulses emitted by LAPCAs in the far field depends on how fast the photocurrent increases and decreases. In this specific illustration, the THz pulses are composed of a positive peak followed by a long and negative tail. Experimentally, many examples show that the THz waveforms are quasi-half-cycle and exhibit strong asymmetry.

For THz radiation from LAPCAs, the role of carrier lifetime can be distinguished into two different regimes relative to the duration of the optical pulses [126–128]. In the first case, the carrier lifetime is approximately equal to or shorter than the laser pulse duration. The second case is when the carrier lifetime is longer than the optical pulse duration. In the first regime, free carriers start to recombine before or just after the total duration of the laser pulse. Consequently, an extremely rapid decay in photocurrent is observed. Of course, in this configuration, the THz waveforms would not be a quasi-half-cycle pulse but will be more a single-cycle pulse with good symmetry between the positive and the negative peak. Numerical studies performed on different semiconductors have shown that when the carrier recombination is faster than 1 ps, the time profile of the radiated electric field has a higher symmetry between the positive and the negative part of the THz pulse [118,127–131]. To put in evidence this phenomenon experimentally, studies performed on LAPCAs made from LT-GaAs with carrier lifetime ranging from 0.35 ps to 1.2 ps have shown that these substrates exhibit a clear transition in the amplitude of the emitted THz pulses from nearly symmetrical bipolar to a quasi-unipolar waveform [123]. In other words, the LAPCA with the shortest carrier lifetime radiates THz pulses with good symmetry, while the one with the 1.2 ps carrier lifetime was strongly asymmetric with a slight enhancement of the THz peak electric field (Figure 2-6 a-c). The strong negative peak observed in the THz pulses emitted by the shortest carrier lifetime LT-GaAs LAPCAs is due to the faster decay in transient photocurrent due to the relatively short carrier lifetime. In the second regime, where the carrier lifetime is much longer than the duration of the optical pulse, the decay of photocurrent is relatively slow, and then the derivative of this part is almost zero. Thus, the negative polarity of the THz waveform tends to be zero. Numerically, it has been shown that a carrier lifetime longer than 2 ps has almost no effect on the peak photocurrent density and the THz waveforms [129–132]. Experimentally, all the LAPCAs fabricated from semiconductors with a carrier lifetime longer than 2 ps generate asymmetric quasi-half-cycle THz pulses [123,133]. There is a significant advantage of having a substrate with a short carrier lifetime, for example, below 1 ps, if the

maximum radiated peak electric field is not impacted, we could apply a larger bias field. We will discuss this point in the next section.

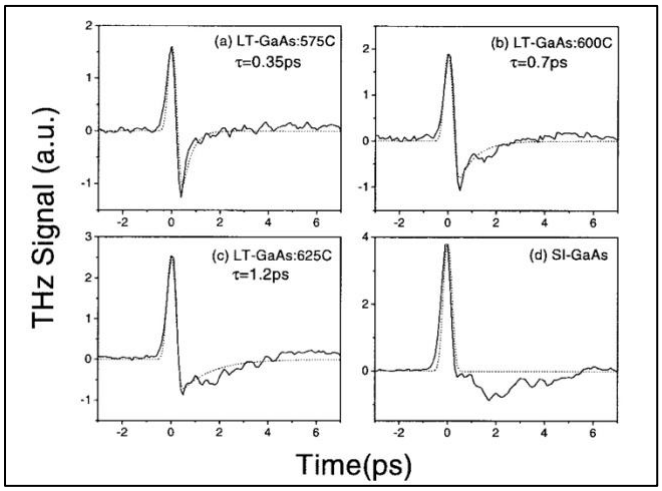

Figure 2-6 THz waveforms from LT-GaAs and SI-GaAs emitters excited with low optical fluence single pulses. Emitter material: (a) LT-GaAs annealed at 575 ˚C, LT-GaAs annealed at 600 ˚C, (c) LT-GaAs annealed at 625 ˚C, and (d) SI-GaAs [123].

There have been several theoretical studies on the influence of the laser pulse duration on the THz pulses emitted by photoconductive emitters [125,128,134]. This latter parameter has a significant influence since the THz electric field is proportional to the time derivative of the photo-current density. Intuitively, one could imagine that a longer pulse duration induces a longer time injection of free carriers, which in turn creates a slower current transient and less intense peak current. Consequently, the duration of the half-cycle THz pulses will be longer with a lower peak electric field. Simulations based on the Drude-Lorentz theory model or by a semi-classical Monte-Carlo simulation showed that for a laser pulse duration of 30 fs and above, when the laser pulse duration is increased, the THz peak field decreases, the duration of the THz pulse increases and the frequency components of this pulse are narrower and the peak frequency shifts toward lower frequency [126,128,134,135]. More surprisingly, the three-dimensional Monte-Carlo simulation shows that a maximum THz peak field is reached for a laser pulse duration of 40 fs. However, for shorter laser pulse duration, the THz peak field decreases [126]. This drop is attributed to the fact that a shorter laser pulse with a duration below 40 fs is extremely broad. Consequently, the variation of photon energy is also large. For example, photons with energy smaller than the bandgap will not participate in the processes of THz generation since they will not be absorbed by the substrate. On the other hand, photons with much larger energy than the bandgap could

excite carriers into the satellite valley where the electron mass is higher and the carrier mobility smaller, thus making it less efficient for the THz generation process [126].

2.3.3.4 PCA failure

As previously mentioned, the most straightforward method to generate high-intensity THz pulses from LAPCA is to apply the highest bias field possible. The semiconductor substrate of a LAPCA, under the excitation of a femtosecond laser pulse, shows a rapid decay in its resistivity. Such a low-resistivity substrate, when biased with high voltage, could lead to inevitable failures. It is well-known that photoconductive switches have a limited lifetime, from several shots up to millions of shots if the performances of the switch are pushed to the limit [136]. Among the most common failures observed in conventional PCAs is thermal heating that leads to thermal runaway, corona discharge, surface flashover and dielectric breakdown. Dielectric breakdown happens when the electric field is strong enough to rip electrons from the valence band to the conduction band. Then this electron is accelerated by the electric field itself and gains kinetic energy. This electron can collide with another bound electron and get excited into the conduction band, creating another free electron. In the end, the rapid multiplication of free electrons leads to an avalanche dielectric breakdown where the semiconductor substrate becomes conducting [137]. The dielectric breakdown happens at lower fields for material with relatively low bandgap or when the quality of the substrate is poor with defects, high grain, and high micro stripe density. It is intuitive to understand that dielectric breakdown by electron avalanche happens at a higher bias field when using low-bandgap semiconductors. On the other hand, flashover and corona discharge occurs when dust, grease or charge accumulation arises at one of the electrodes and suddenly discharges. These arcs gradually deteriorate both the substrate and electrodes, which considerably reduce the lifetime of the photoconductive emitter. However, in all cases of failure, the most common is likely the thermal runaway. The photocurrent that creates heat by the Joule effect and the power of the illuminated laser leads to the rise in the switch temperature. A study has shown that for a GaAs photoconductive switch, an increase of 25 degrees results in a drop in the bias electric field threshold by 40% [138]. In another work, some GaAs microstructure PCAs for THz generation have been investigated using X-ray diffraction topography [139]. It was shown that due to the increase in temperature, some electromigration of the gold electrodes occurred, resulting in a total electrical short-cut of the electronic circuit preventing the PCA from working (Figure 2-7). Moreover, the GaAs substrate itself was degraded. To prevent thermal runaway, it is preferable to choose semiconductor substrates with high thermal conductivity for dissipating heat. In addition, it is important to realize high-quality Ohmic contacts on the substrate.

Another option is to have a substrate with a short carrier lifetime and high dark resistivity to limit the heating of the PCA by the current. The dark resistivity of the photoconductive antenna (PCA) is the resistivity measured in the off-state when the antenna electrodes have maximum resistance and there is no illuminating laser beam. This resistivity is primarily determined by the bandgap of the semiconductor substrate. The use of wide bandgap semiconductors with high dark resistivity reduces the heating of PCAs by lower dark currents. Another option is to work with a semiconductor substrate with a short carrier lifetime. The short lifetime reduces the duration of

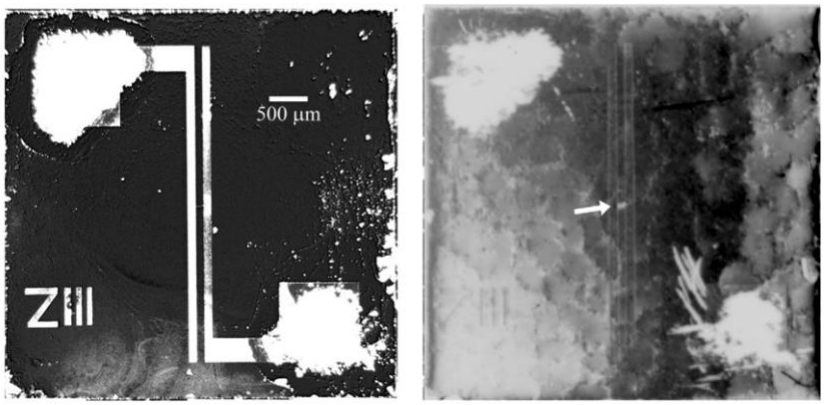

Figure 2-7 Optical micrograph (a) and respective X-ray topography (b) of a failed PCA
X-ray topography of the antenna shows considerably grain boundaries and domains as well as electro-migration of gold (arrow) in between the microstrips [139]

the photocurrent, which is the specific moment where the heating by the Joule effect is stronger. Many techniques have been tested on GaAs semiconductors for decreasing the carrier lifetime. These studies are clearly described in the review on microstructure PCA for THz radiation by Burford *et al.* [48]. Most of these GaAs PCA with short carrier lifetime show general performances that are better than SI-GaAs PCA and equivalent to LT-GaAs PCA. This was possible because the higher thermal stability of the PCAs allows applying a higher bias field, which in turn increases the maximum radiated peak electric field. To reduce the lifetime of carriers inside the GaAs substrates, one of these techniques is ion implantation. Recent studies have shown that ion implantation in GaAs semiconductors improves their carrier mobility compared to LT-GaAs, resulting in point defects within the crystal structure. These recombination centers, in turn, can significantly reduce the carrier lifetime [140,141]. GaAs doped with Ar^+ ions had the shortest carrier lifetime over semi-insulating and low-temperature grown GaAs substrates [142]. Using the same technique, several research groups have implanted ions such as oxygen, nitrogen, and iron into GaAs crystals, resulting in very short carrier lifetimes [143,144]

2.3.4 Materials for the Development of THz-PCAs

In the previous section, we reviewed the different parameters of semiconductors substrates that would influence the intensity of the THz pulses radiated by LAPCAs. We mentioned that a high dielectric strength linked with a wide bandgap is the most critical parameter. Other important parameters are carrier mobility for optimized efficiency and good thermal conductivity. From Table 2-3, one can see that diamond is probably the perfect material for generating intense THz radiation. A chemical vapor deposition (CVD) grown polycrystalline diamond thin film was tested to fabricate a LAPCA with an interdigitated structure illuminated by an excimer laser [65]. In this study, the applied bias field was increased by depositing an encapsulation layer up to 0.5 MV/cm. Although diamond LAPCA offers promising results, without saturation of the scaling of the THz field versus bias field, with an obtained radiated energy density as high as 10 $\mu J/cm^2$, which is one order of magnitude larger than GaAs, with a bias field applied of 100 kV/cm, diamond PCA has not been intensively studied. This is due to its bandgap of 5.46 eV, which requires the 4^{th} harmonic of an 800 nm Ti: Sapphire laser or a two-photon absorption process with an excimer laser, which has limited until now its application. In addition, the cost of the diamond antenna dramatically reduces its attractiveness. For this purpose, ZnO and GaN are other wide-bandgap semiconductors used as promising materials for the fabrication of LAPCAs [66,67,145]. However, in the case of ZnO, the poor fabrication quality of the substrate, with many defects, leads to the saturation of the THz yield as a function of the bias electric field for values as low as 0.8 kV/cm. In comparison, GaAs LAPCA has demonstrated linear scaling of the THz field versus bias field up to 50 kV/cm [146]. In the next section, we will examine the performances of ZnSe and SiC LAPCAs pumped above and below the bandgap by the first and the second harmonic of a Ti: Sapphire laser. Then, using an ultraviolet (UV) laser, we will review the performances of LAPCAs fabricated with different wide bandgap semiconductors and pumped by a UV laser with a photon energy of 5.0 eV.

2.3.4.1 Zinc selenide

Zinc selenide (ZnSe) has a bandgap of 2.67 eV and is widely used as optical windows and lens for the infrared region [147]. ZnSe substrates were also used as photoconductive switches where switching of bias field above 100 kV/cm with a peak current of 100 kA/cm^2 with electrodes deposited on the two-opposite face of the substrate were achieved [148–150]. Due to these good performances, it was natural to test ZnSe PCA for THz generation. The ZnSe bandgap allows photoexcitation with Ti:Sapphire laser via standard photon absorption (PA) when using the 2^{nd}

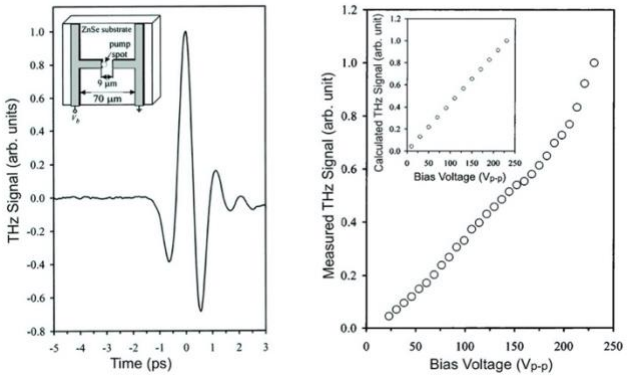

Figure 2-8 Waveform of the THz pulses from ZnSe H-dipole micro-structured PCA, (b) Measured peak-to-peak THz field amplitudes as a function of the external bias voltage[151].

harmonic, and via two-photon absorption (TPA) when using the fundamental harmonic. In the first case, we will discuss the above bandgap photoexcitation, and in the second case, we will discuss the below bandgap photoexcitation. The first demonstration of THz radiation from ZnSe PCAs was done by J. F. Holzman *et al.* [151]. The PCA was an H-dipole geometry with a gap of 9 μm (Figure. 2-8 (a)). By focusing the optical spot close to the anode with an excitation wavelength of 800 nm with below bandgap excitation, they demonstrate a linear scaling of THz field versus bias field up to 125 kV/cm and versus fluence up to 28 mJ/cm^2. The linear behavior of the scaling of the THz pulse versus bias field is very important since it is the major condition for scaling up the source for high-intensity THz pulse generation (Figure 2-8 (a)). Surprisingly, the peak electric field of the THz pulse scales linearly with the fluence up to 28 mJ/cm^2 without showing any sign of saturation. Indeed, the below bandgap photoexcitation leads to a TPA process, which is a non-linear process and depends on the intensity of the laser pulse. However, there is no reason that the PCA would not show any saturation regime if the optical fluence keeps increasing. We note that these results differ from the observations in another work with THz wave generation via single-photon and TPA in ZnSe LAPCA pumped by an amplified Ti:Sapphire laser [152]. This

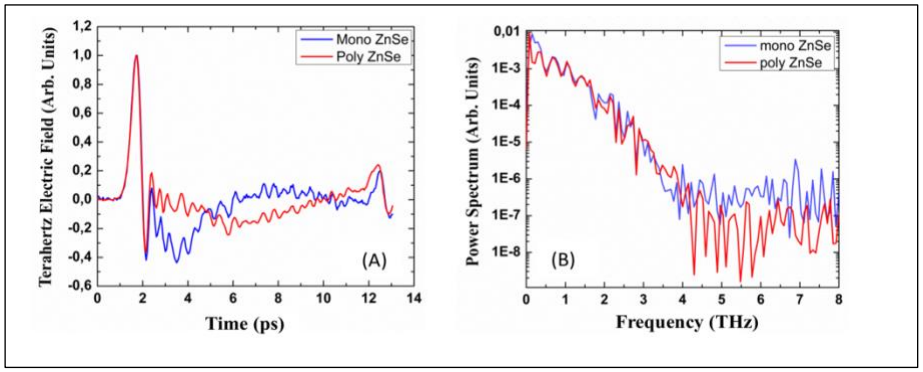

Figure 2-9 (a) Normalized waveforms and (b) relative spectra of the THz pulses emitted by mono- and polycrystalline ZnSe LAPCAs [152].

study shows the influence of the wavelength and the quality of the substrate on the THz generation from the ZnSe LAPCAs [152]. For this study, ZnSe monocrystalline and polycrystalline substrates were used to fabricate LAPCAs with an interelectrode distance of 1 mm, with electrodes on each side of the crystal to limit air breakdown. The normalized waveforms of the THz pulses emitted from mono- and polycrystalline ZnSe LAPCAs, as well as the corresponding power spectrum of radiated THz pulses obtained by Fourier transform, are shown

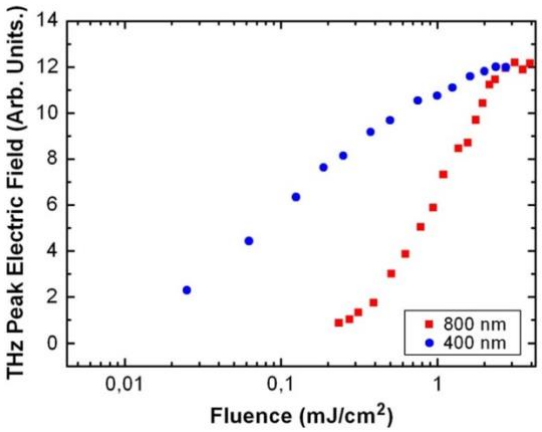

Figure 2-10 Fluence dependence of the peak THz electric field from ZnSe single crystal antenna illuminated at 400 nm and 800 nm [152].

in Figure 2-9 the performances of mono- and poly-crystalline ZnSe LAPCAs excited with 400 nm laser pulses were studied. Linear scaling of the THz peak field as a function of bias voltage and a hyperbolic behavior of the scaling of the peak field versus optical fluence were found. The major difference was in the value of the saturation fluence, which was measured to be 0.15 mJ/cm^2 for monocrystalline ZnSe LAPCAs and 1.01 mJ/cm^2 for polycrystalline ZnSe LAPCAs. The difference in the saturation fluence was attributed to the difference in carrier mobility between the two substrates. Next, the authors studied the differences in the performance of monocrystalline ZnSe LAPCA excited above and below the bandgap. As mentioned above, the scaling of the THz field follows a hyperbolic behavior versus optical fluence when pumped above the bandgap. On the other hand, when the ZnSe LAPCA is pumped below the bandgap with an 800 nm laser pulse, the scaling of the THz pulse follows a quadratic behavior for fluence below 0.7 mJ/cm^2, then it becomes linear for fluence up to 2.1 mJ/cm^2 and saturation starts to occur for fluence above 2.1 mJ/cm^2 (Figure 2-10). More importantly, when the LAPCAs are working in the saturation regime, the field of the THz pulses generated by the monocrystalline ZnSe LAPCAs saturates at the same peak field value for above and below bandgap. The only noticeable difference was that the ZnSe LAPCA pumped with 800 nm laser pulses was more fragile than when pumped with 400 nm laser pulses. This difference was attributed to the fact that the optical power and the Joule effect leading

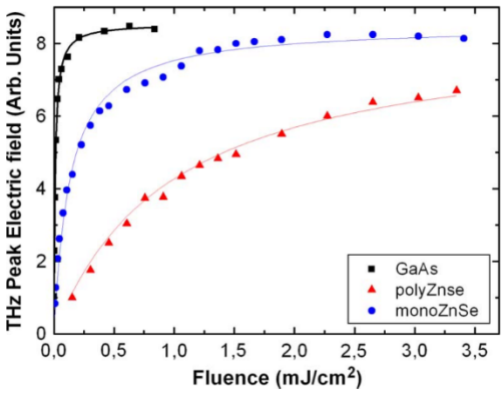

Figure 2-11 Fluence dependence of peak field of THz radiation from GaAs, ZnSe single crystal, and polycrystalline ZnSe photoconductive antenna
Squares are the experimental data, and solid lines are fits to the data [152].

to the enhancement of the temperature of the switch, was stronger when the LAPCAs were pumped below the bandgap than above the bandgap. Next, they compare the performances of mono- and poly-crystalline ZnSe LAPCAs with GaAs LAPCAs pumped above the bandgap with an 800 nm laser and with the same electrode configuration (Figure 2-11). The scaling of the THz field versus optical fluences was hyperbolic for the three antennas. Of course, due to the difference in carrier mobility between the three substrates, the saturation fluence of the three LAPCAS was quite different (0.01, 0.15 and 1.07 mJ/cm^2 for GaAs, mono-and poly-crystalline ZnSe LAPCAs, respectively). However, it is quite fascinating that the value of the THz peak field once the LAPCAs operated in the screening regime was the same for the three antennas (Figure 2-12).

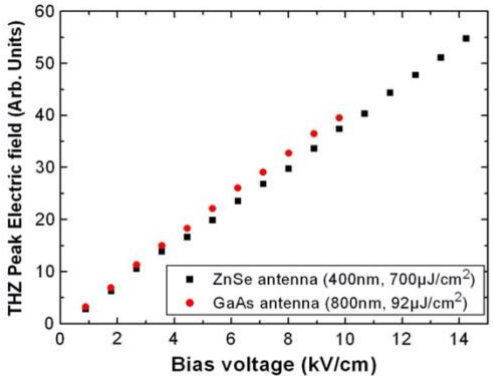

Figure 2-12 Comparison of bias field dependence of the peak THz electric field for GaAs antenna excited at 800 nm and monocrystalline ZnSe antenna excited at 400 nm [152].

The last part of the study was to compare the scaling of the THz peak field as a function of the bias field for the monocrystalline ZnSe LAPCAs and the GaAs LAPCAs [51]. The two curves show linear behavior with approximately the same slope. However, while the GaAs LAPCAs break down at a bias field of around 10 kV/cm, the ZnSe LAPCA took advantage of its higher dielectric

strength and sustained higher bias voltage. Consequently, the peak electric field of THz pulses generated by the ZnSe LAPCAs was larger than that generated by the GaAs LAPCA.

2.3.4.2 Silicon carbide

Silicon Carbide (SiC) has dielectric strength and thermal conductivity that are more than ten times higher than GaAs with relatively high carrier mobility. These semiconductors are also highly resistant to damage, such as corona discharge, due to their extreme hardness. In addition, good electrical properties and excellent thermal stability make these semiconductors an ideal candidate for manufacturing high-power electronic devices such as Schottky barrier diodes, MOSFETs [114] and photoconductive switches [153,154]. For 4H-SiC photoconductive switches with lateral configuration, pumped with 7 ns pulse duration lasers at 355 nm, the switching of 20

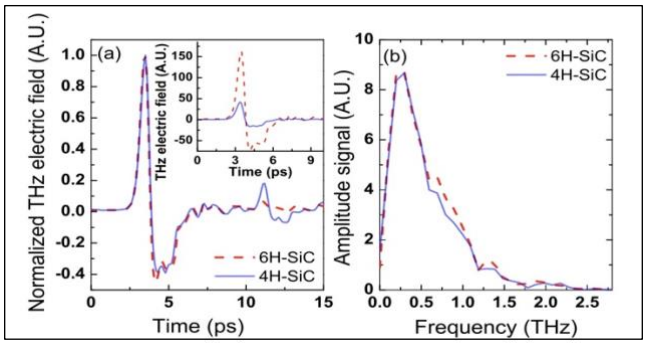

Figure 2-13 Normalized and original THz waveforms (inset) radiated by 6H- and 4H-SiC LAPCA antennas excited at 400 nm, and their respective normalized amplitude spectra presented respectively on the figure (a), and (b) [68].

kV DC voltage for an equivalent bias electric field of 328 kV/cm was demonstrated. The fact that the substrate can withstand this bias field was possible due to the significant improvement in the growth of high-quality SiC substrate, especially 4H-SiC [155,156]. Some damages were also observed, and applying such high fields creates holes at the interface between the contact and the substrate [157]. We note that applying such a bias field onto a SiC LAPCA would generate gigantic low-frequency half-cycle THz pulses, which would open the door for new physics, such as fast magnetization switching by a single pulse [158]. Therefore, LAPCAs based on SiC polytypes having hexagonal symmetry with double (4H) and triple (6H) stacking periodicities pumped by ultrafast laser pulse for THz radiation were naturally tested. The LAPCAs made from semi-insulating 6H-SiC semiconductors were pumped using 800 and 400 nm laser pulses. 4H-SiC LAPCAs were pumped only using a 400 nm laser beam. Figure 2-13 (a) shows the normalized waveform, and in the inset, the original waveforms and (b) their normalized amplitude spectra of the THz pulses radiated by the 6H-and the 4H-SiC LAPCAs [68].

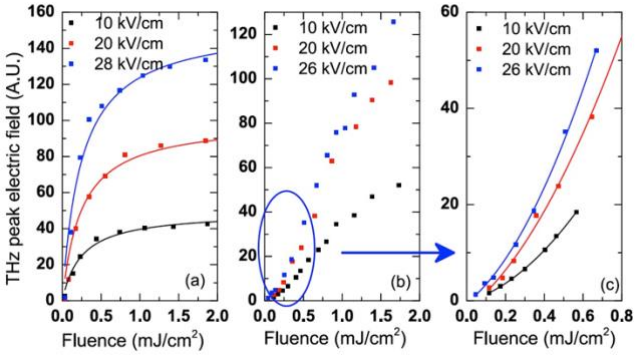

Figure 2-14 THz peak electric field versus fluence for a 6H-SiC (a) and 4H-SiC (b) PCA excited at 400 nm and biased with three different bias fields. (c) is an expanded scale of the bottom left part of (b) [68].

The authors demonstrated a linear scaling of the THz field versus the bias field in all conditions for a bias field up to 32 kV/cm. In this case, linear behavior was demonstrated (Figure 2-14). Further, the scaling of the THz electric field generated by the 6H-SiC LAPCAs only showed a standard behavior in the scaling of the radiated THz field versus optical excitation when pumped with 400 nm laser pulse (Figure 2-14). The saturation fluence was around 0.24 mJ/cm^2, which is close to the saturation fluence obtained with ZnSe LAPCAs. Despite the higher carrier mobility of 6H-SiC, this saturation fluence recorded for LAPCAs is higher than the estimated value. This difference in value was explained by the fact that the 6H-SiC has a bandgap slightly lower than that of the photon energy at the 400 nm wavelength. Consequently, each electron injected into the conduction band requires two-photon absorption. This decreases the quantum efficiency of the free carrier generation process.

Under optical excitation at 800 nm, the 6H-SiC LAPCA shows a similar scaling behavior in the THz field to that of the ZnSe LAPCA when pumped with a laser beam at 800 nm. This was expected since, in this case, the absorption process for the two substrates is two-photon absorption. Despite pumping the LAPCA with pump laser intensities of up to 9 mJ/cm^2, the LAPCA was still not running in the screening regime. More surprisingly, the scaling of the electric field of THz pulses radiated by the 4H-SiC LAPCA pumped by a 400 nm laser pulse was a mixture between a quadratic behavior for optical fluence lower than 1 mJ/cm^2 and a hyperbolic behavior for higher fluences (Figure 2-15). This was explained by the fact that at low optical fluence, the TPA process dominated since the bandgap of 4H-SiC is 3.26 eV, slightly higher than the photon energy at 400 nm wavelength (3.10 eV). However, by increasing the optical fluence, the onset of saturation appears due to the screening of the bias field by the THz field. The screening regime

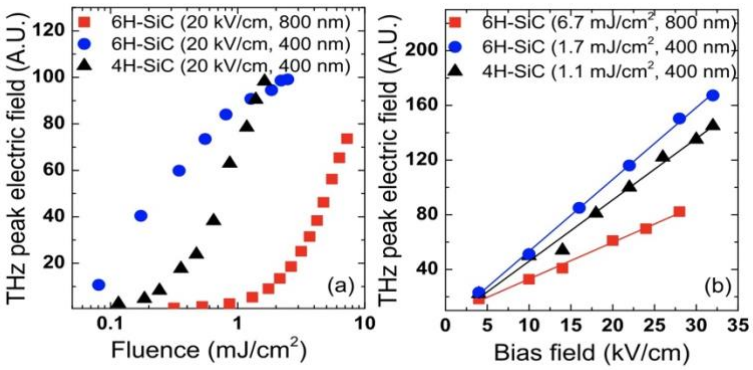

Figure 2-15 THz peak electric field versus fluence for 6H-SiC PCA excited at 400 nm and 800 nm, and for 4H-SiC PCA excited at 400 nm at the bias field of 20 kV/cm. The plot (b) shows the peak THz electric field versus bias field for 6H-SiC PCA [68].

appears at much higher fluence for the 4H-SiC LAPCAs than the 6H-SiC LAPCAs, although the carrier mobility is higher.

2.3.4.3 Large bandgap semiconductors excited by UV lasers

As we have previously discussed, to take advantage of LAPCAs fabricated from wide-bandgap semiconductors pumped by the second harmonic of a Ti:Sapphire laser, the bandgap of the semiconductor substrate must be less than 3.1 eV to maximize photon absorption. To extend the choices of the semiconductor crystal, one solution is to work with lasers with a fundamental wavelength shorter than 400 nm. Excimer lasers are a family of high-pressure, pulsed gas lasers that produce intense UV light [159]. The wavelength of these lasers is determined by the gas gain media of the laser ranging from 193 nm to 353 nm [160]. Also, with specific configurations, the duration of the laser pulse can be compressed to a few hundreds of femtoseconds and even shorter [161–163]. As we mentioned earlier, diamond PCAs have been studied using a KrF laser with a pulse duration of 500 fs at 248 nm [65]. The photoconductive emitters based on GaN semiconductors have also been studied under the excitation of the 3rd harmonic of a Ti:Sapphire laser with a pulse duration of 120 fs and an energy of 19 μJ/pulse at 266 nm [66]. In addition, GaN PCAs have been recently studied using driving laser pulses at 352 nm from an optical parametric amplifier (OPA) [164]. All these studies show high potential for generating intense THz pulse from LAPCA with wide bandgap semiconductor crystal pumped by a UV laser. However, there was no direct comparison of their performances as a substrate of LAPCAs.

Recently, a study was performed on the THz radiation from LAPCAs fabricated from ZnSe, 6H- and 4H-SiC, GaN and β-Ga_2O_3 using KrF laser excitation at 248 nm, which allowed a direct comparison of their performances [165]. The main reasons why these crystals have been

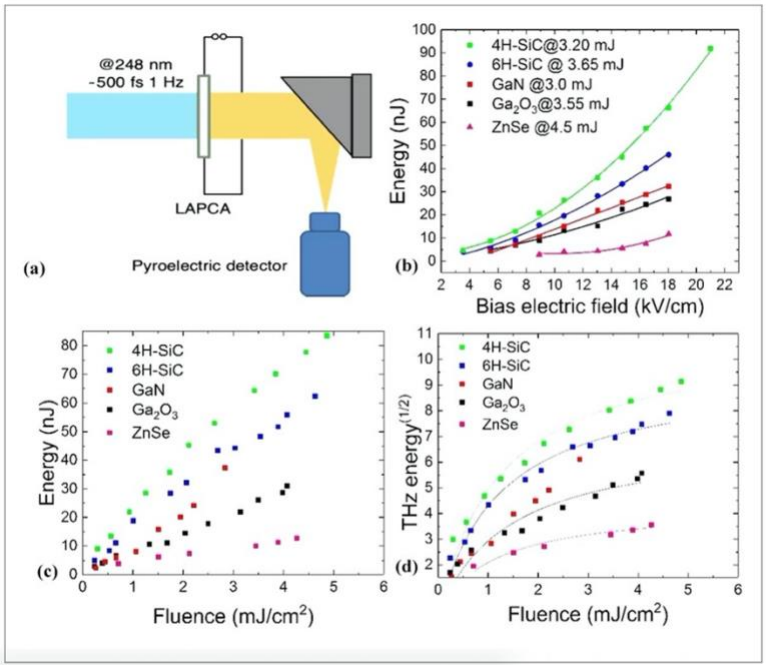

Figure 2-16 The energy of the THz pulses radiated from 4H-SiC, 6H-SiC, GaN, Ga2O3, and ZnSe LAPCAs as a function of bias field and optical fluence
(a) experimental configuration, (b) scaling of the THz energy as a function of the bias field, (c) optical fluence for all LAPCAs and (d) scaling of the square root of THz energy as a function optical fluence [165].

selected are because most of them have been tested previously for THz generation from PCA. In addition, these semiconductors have a bandgap of less than 5 eV with high dielectric strength and are commercially available with relatively large wafer sizes. The design of all the LAPCAs studied was the same, with the electrode length and gap size of 15 mm and 3 mm, respectively, using Cr/Al electrode deposition. To excite these photoconductive emitters, a hybrid dye-excimer laser (KrF) with pulse energy and duration of 30 mJ and 500 fs, respectively, at 248 nm is used [166]. The scaling of the THz pulse energy as a function of the bias field and optical fluence is shown in Figure 2-16. The authors showed that the 4H-SiC and the 6H-SiC emitted the maximum THz pulse energy in this configuration, followed by GaN, β-Ga_2O_3 and ZnSe LAPCAs, in descending order. As can be seen from Figure 2-16, at a bias field of 18 kV/cm and an optical fluence of 3 mJ/cm^2, the energy of the THz pulses radiated by the 4H-SiC LAPCA was 1.5 and 2 times higher than that of the 6H-SiC and the GaN LAPCAs, respectively. For almost all antennas, the scaling of the THz energy was quadratic with the bias field and mostly hyperbolic with the optical fluence. When the optical fluence was high enough, the scaling of the THz energy reached a saturation regime. The latter observation is in good agreement with the theory. Surprisingly, despite the significant differences in their carrier mobility, all the LAPCAs studied have shown almost the same saturation fluence of around 1.2 mJ/cm^2. Indeed, the calculated carrier mobility

for ZnSe and 6H-SiC LAPCA is between 50 and 60 cm^2/Vs, which is approximately one order of magnitude smaller than the theoretical values. This difference is attributed to the fact that the 5.0 eV photon energy of the 248 nm laser pulse pumps the electrons into the higher valley of the conduction band, where the effective mass of the electron is higher with smaller carrier mobility. We note that the carrier mobility of 4H- and 6H-SiC, β-Ga_2O_3 and ZnSe are close to that of GaN LAPCA when pumped by a 266 nm laser pulse and 120 fs duration [165]. Also, the observed difference in performances of the LAPCAs studied can be explained by the difference in inter- and intra-valley carrier dynamics of the semiconductor substrates [126–128]. However, to fully understand the scattering mechanisms, additional measurements such as optical pump/THz-probe spectroscopy is needed [167].

In this section, we review the principal results on LAPCAs, demonstrating their potential for generating intense THz pulses. We have shown how wide-bandgap semiconductor crystals are well adapted for generating intense THz pulses when excited by the second harmonic of a Ti:Sapphire or UV laser pulses. Our research has shown that, except for two works with GaAs LAPCAs pumped by 800 nm laser pulses, there does not exist any demonstration of the generation of intense THz pulses with LAPCAs with peak field above 100 kV/cm [116,168]. The major reason is that these THz devices require a large area with a very high pulse voltage of up to several tens of kV [169]. Such pulsed, high-voltage sources are dangerous to handle and expensive. To overcome this challenge, one solution is to work with ILAPCA, which keeps the size of the antenna large while reducing the gap size, thus avoiding the use of very high voltage pulses. One parameter that we did not mention is the electrode configuration. Many works have shown that the design of electrodes onto the PCAs is an important parameter that influences the efficiency and the maximum intensity of the radiated THz pulses [48,122]. It was shown that the highest power was obtained with an SI-GaAs bowtie PCA. However, these sources are not well adapted to generate THz pulses with high peak intensity, like plasmonic antennas, since their configuration is not scalable to a larger area, so we did not develop this part. Another characteristic of PCA is that with a specific electrode configuration, one can manipulate the polarization of the radiated THz field. For example, THz pulses with longitudinal, radial and azimuthal polarization have been demonstrated [170,171].

2.3.5 Interdigitated Large-Aperture Photoconductive Antennas

The idea of working with interdigitated large-aperture photoconductive antennas (ILAPCAs) was taken from the interdigitated photoconductive switch technology, which was

studied in the mid-1980s [172,173]. ILAPCA simply consists of a pair of anode and cathode connected to several open-ended parallel electrode combs (Figure 2-17). Therefore, ILAPCA is an array of small photoconductive antennas connected in parallel. Consequently, two adjacent open-ended electrodes with the same gap size will generate THz pulses having opposite polarity, which will interfere destructively when propagating in the far-field [129,174–178]. Therefore, it is necessary to block the illumination of all antennas biased with one specific bias field direction (positive or negative) by using, for example, a shadow mask. Thus, destructive interferences are avoided by generating carriers only in gaps with the same polarity of the applied bias field. Consequently, by blocking the incident optical excitation in every second inter-electrode spacing, photogeneration occurs only in regions with the same bias field directions, and there will be constructive interference of THz pulses emitted with the same polarity in the far-field [179]. Traditionally this process is performed during the fabrication process of the ILAPCA by the

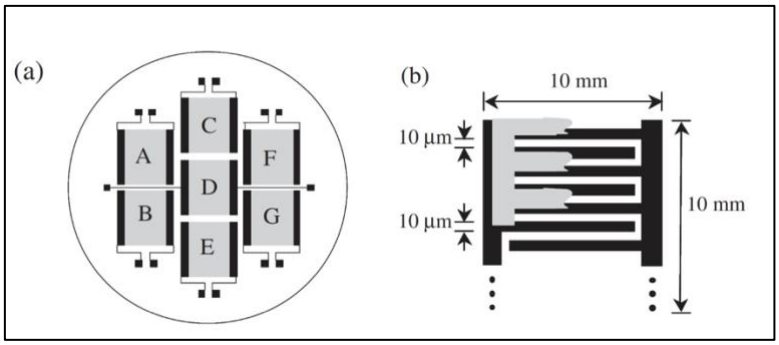

Figure 2-17 Top view of an ILAPCA fabricated on a SI-GaAs substrate (a) Schematic of THz emitter composed of seven photoconductive antenna units having interdigitated electrode structure (b) Structure of electrodes and shadow mask of each unit [174].

photolithography technique. After the deposition of electrodes onto the substrate, a thin dielectric layer, such as SiO_2, is deposited on the top of the electrodes, followed by the deposit of a metal layer only onto the neighboring antenna. The role of the second metallic layer is to reflect the incoming laser pulse avoiding the illumination of the neighboring antenna, while the role of the dielectric layer is to avoid electronic short-circuit between the electrodes and the second metallic layer. The inter-electrode spacing of the antenna is traditionally limited by the thickness of the deposited dielectric layers. Since the thickness of the deposited dielectric layers is limited, the maximum gap size of the antenna is restricted. ILAPCAs offer several advantages over conventional LAPCAs. As we mentioned earlier, the reduced distance between the cathode and anode allows large bias fields to be applied without needing a very high-voltage power supply. The drop in applied bias voltage reduces the heating of the ILAPCAs by the Joule effect and prevents antenna failure allowing a higher bias field to be applied. Also, the maximum bias field

applied is limited by the air breakdown on the antenna surface [180]. It has to be noted that this encapsulation layer for the improvement of the maximum bias applied field can also serve as an anti-reflection coating, improving photon absorption [58,59,68]. Further, the trap field enhancement, which is just an enhancement of the bias field localized close to the anode, is multiplied due to the multiplication of the number of anodes inside the comb [60,126,181].

Despite these advantages, ILAPCAs have some drawbacks. The biggest one is that by using a standard shadow mask on the interdigitated structure, only half of the total antennas will be illuminated. If we add the surface of the electrodes, where in some cases the electrode width is equal to the inter-electrode distance, only 25% of the total surface of the ILAPCA will be illuminated and will efficiently participate in the generation of the THz radiation [146]. This reduces the maximum radiated peak electric field and efficiency of the ILAPCA. Another drawback is that by adding the second metallic layer on the top of the interdigitated structure, the inter-electrode distance is limited by the maximum thickness of the dielectric layer, which is generally limited to a few tens of μm before cracks start to appear. Consequently, the gap size is chosen to be in the 10s of μm range or smaller [182], which limits the maximum radiated THz field due to the appearance of strong space-charge screening at a timescale shorter than 1 ps. The other consequence is that the waveforms of the THz pulses change from a quasi-half cycle to a single-cycle nature. Finally, the multiplication of the number of antennas inside the interdigitated structure increases the capacitance significantly, which can, in turn, distort the high-voltage pulse for biasing the ILAPCA and reduce the maximum radiated power [183–185]. Another point is that ILAPCA has a large area with a diameter much larger than the wavelength of the radiated THz waves. Therefore, we expect a THz beam divergence that is relatively small. However, the inter-electrode distance is smaller or equivalent to the radiated wavelength, while the electrode length will be much larger than the radiated wavelength. Consequently, the beam divergence will be

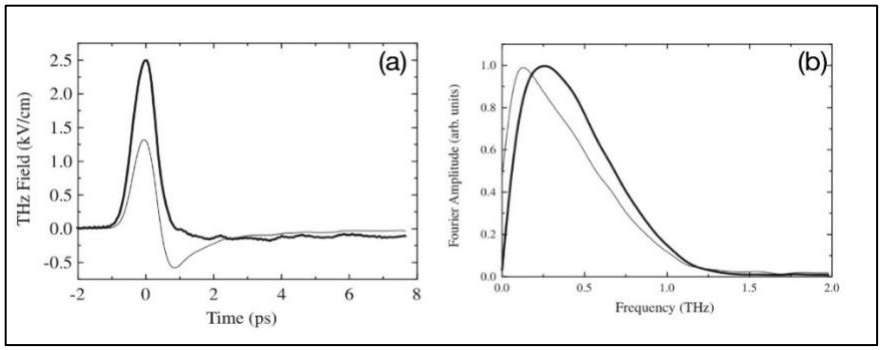

Figure 2-18 THz waveforms and respective spectra obtained from conventional LAPCA (thick line), and micro-structured LAPCAs (thin line) [174].

quite different for the direction perpendicular versus the direction parallel to the electrode orientation. As a result, it is generally challenging to focus the THz beam close to the diffraction limit, which is one of the key points for achieving a large peak field.

2.3.5.1 Overview of Interdigitated LAPCAs

To overcome the limitations of conventional LAPCAs with the goal of increasing the peak intensity of the emitted THz pulses, several works have focused on ILAPCAs [65,146,165,174,175,186–188]. One of the key points was the demonstration of increased intensity of the THz pulses emitted by ILAPCAs compared to THz pulses generated by conventional LAPCAs. The first comparison was made by Hattori *et al.* [174] where they compared the intensity of THz pulses generated by a conventional SI-GaAs LAPCA with a 3 cm gap size with an ILAPCA with 7 units with an area of

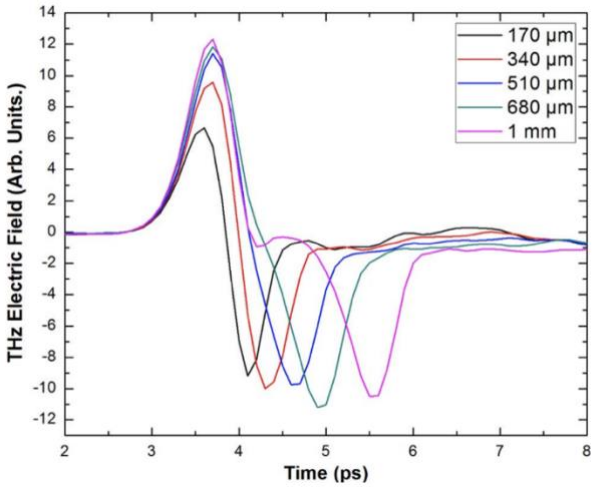

Figure 2-19 Evolution of the THz pulse shape for different glass phase mask thickness used on GaAs ILAPCA The thickness of the phase masks covered the antenna are respectively 0.17, 0.34, 0.51, 0.68, and 1 mm, and GaAs ILAPCA is biased by an external field of 1.2 kV/cm at the excitation fluence of 14 µJ/cm2 [133].

1 cm^2 each, connected together, with gap size and electrode width equal to 10 µm for a total illumination area of 25%. Although the ILAPCA was biased at 30 kV/cm, compared to only 2 kV/cm for the LAPCA, the THz pulses generated from the LAPCA were 2 times larger than the one from the ILAPCA (Figure 2-18 (a)). Following the scaling law of the peak amplitude of the THz pulses as a function of the illuminated area, the peak field of the THz pulses emitted by the ILAPCAs should have been 7 times larger than the peak electric field of the THz pulses emitted by the conventional LAPCAs. The authors explained that the difference in amplitude of the emitted THz pulses was due to insufficient charge supply within the ILAPCA due to the small gap size. However, we believe that a 10 µm gap size of SI-GaAs ILAPCA can lead to a strong static Coulomb field that screens the bias field, which is the origin of the space charge screening, which could explain this difference [189]. This hypothesis is supported by the observation that the

waveforms of THz pulses generated by the LAPCA and the ILAPCA are completely different. The waveforms of the THz pulses generated by the LAPCA are asymmetric and quasi-half cycle. In contrast, the waveform of the THz pulse generated by the ILAPCA is a single cycle and symmetric, which is a sign of space-charge screening. Another theoretical study shows that the amplitude of the generated THz pulses from a GaAs ILAPCA is 3 times larger than the peak electric field radiated by a dipole antenna. However, although the optical fluence and applied bias field remain constant, the illuminated area of the PCA with an interdigitated structure was larger than the one of the dipole antenna, which makes it difficult to directly compare the performance of both antennas [181]. Using the same approach, Dreyhaupt *et al.* showed that the amplitude of the THz pulses emitted by SI-GaAs ILAPCAs is 20 times larger than those of a SI-GaAs dipole antenna [190,191]. However, due to the difference in the size of the illuminated area, it is difficult to directly compare the performance of both antennas.

One of the key aspects of ILAPCAs is to manipulate the antenna structure to control the specific parameters of the THz pulses emitted or to increase the efficiency and performance of the antenna. For example, there are different techniques for blocking the illumination of the neighboring antenna. One consists of using a large-aperture microlens area with a hexagonal structure to lead the beam onto every other antenna of the interdigitated structure [192,193]. The latter enhances the efficiency of the ILAPCA since all the optical energy is used to illuminate its active area. Another technique consists of suppressing one bias field direction by etching the active area of the neighboring antennas [194]. This technique is demanding in terms of cleanroom micro-fabrication because a thin semiconductor layer needs to be transferred onto an insulating substrate and etched into grooves. The last step consists of the deposition of metal electrodes on this structure. With this technique, using an LT-GaAs ILAPCA, the generation of THz pulses with a peak field up to 120 kV/cm was demonstrated [195].

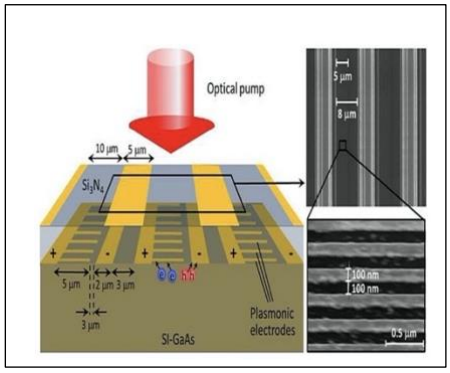

Figure 2-20 Schematic and scanning electron microscope images of a large area plasmonic photoconductive source fabricated on a SI-GaAs substrate [83].

Another technique that could replace the deposition of the second metallization is the binary mask. The latter allows the entire illumination of the interdigitated structure by delaying the timing of the antenna illumination with the opposite bias field direction. This avoids the destructive interference from the quasi-half cycle THz pulses with opposite polarity since a time delay is introduced between them [133]. Indeed, the binary mask is only composed of a piece of glass that is transparent at the wavelength of the optical pump. As a result, we first observe the generation of a quasi-half-cycle THz pulse for each antenna that is not covered by the mask. After a time delay, this is followed by the generation of another quasi-half-cycle pulse with opposite polarity, originating from the neighboring antenna covered by the mask. By adjusting the time delay, which is proportional to the mask thickness, and mixing the glass piece with some opaque pieces, it is possible to perfectly control the waveform of the THz pulses and to perform THz pulse shaping. Consequently, increasing the thickness of the phase mask increases the time delay between the positive and negative polarity of the THz pulses. Further, the optical-to-THz conversion efficiency, as well as the energy of the THz pulses emitted by ILAPCAs, can be doubled (Figure. 2-19). Another parameter that influences the intensity of the THz pulses generated from the ILAPCA is the interdigitated structure itself. It has been demonstrated that increasing the width of the anode, for substrates having much higher electron mobility than hole mobility can significantly increase the amplitude of the THz field [196]. The enhancement in the THz pulse amplitude was attributed to the plasmonic oscillation induced by electrons arriving at the anode. Singh *et al.* demonstrated that changing the anode width from 2 to 50 µm could increase the peak field of the emitted THz pulses by up to 7 times. However, for an electrode width over 50 µm or for an antenna with a gap size larger than the radiated wavelength, this effect tends to saturate [197]. In terms of efficiency, selecting an electrode width equal to the inter-electrode distance when using a shadow mask is the worst configuration since only 25% of the total area of ILAPCA is effective for illumination when using a shadow mask. One solution for increasing the active area of the ILAPCA is to have a gap size larger than the electrode width [183]. However, this ratio of the effective area illuminated can be further increased by reducing the dark gap size relative to the bright gap size and optimizing the width of the anode. It has been demonstrated that an ILAPCA with a gap size, anode and cathode width, and dark gap size of 20, 10, 5 and 5 µm, respectively, results in an enhancement of 1.5 times in the radiated THz peak field compared with an ILAPCA with the same area but reduced gap size and anode width of 5 µm each [198]. This relative improvement is attributed to the plasmonic effect occurring near the anode and to the acceleration of carriers within the substrate, where the illuminated surface has been doubled from 25% to 50%. While playing with the parameters of the

interdigitated structure, we can achieve a significant improvement in the THz intensity, it is also possible, by reducing the distance of the bright gap, to modify and compress the waveform of the THz pulses, which leads to a broadening of the THz spectra [199]. By using a 2 µm gap size for a semi-insulating GaAs ILAPCA, the generation in reflection mode of THz pulses with frequencies extending up to 20 THz has been demonstrated. The enhancement of the cut-off frequency was to the detriment of the peak electric field, which was reduced due to the strong space-charge screening effect [200].

Pushing the microfabrication technology to the extreme, interdigitated PCAs were manufactured with an electrode comb having nanometric gap sizes [83]. These plasmonic photoconductive emitters have shown significant enhancement in THz power and optical-to-THz conversion efficiency up to 50 times over standard micro-PCAs, with a conversion efficiency of

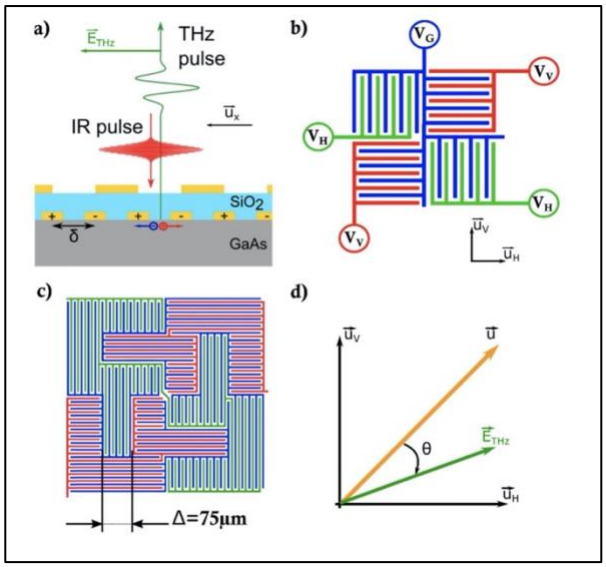

Figure 2-21 Interdigitated photoconductive switch used for modulation of the polarization of radiated THz pulses (a) cut view of the antenna (b) top view of the intermixed geometry principle, (c) Large area implementation investigated with total area of the gold finger electrodes (d) orientation of the wire grid polarizer [56].

1.6% for an interdigitated structure (Figure 2-20). Despite their impressive performance, these antennas are not considered as large-area emitters due to their limited dimensions (less than a few mm), which is the key aspect for generating intense THz pulses [59]. Another key aspect parameter of the interdigitated structure is its ability to fully control the amplitude and degree of polarization of the THz field emitted. Indeed, by building an ILAPCA with an intermixed sickle geometry, with vertical and horizontal electrodes, allows the generation of THz waves with horizontal and vertical polarization (Figure 2-21) [56]. It has been shown that the generation of THz pulses with amplitude and degree of polarization can be controlled by applying different voltages to the vertical and horizontal electrodes. The speed of this photoconductive device for

polarization modulation can reach up to 10 kHz, which opens new perspectives for THz polarimetry measurements with small polarization changes.

2.3.5.2 Generation of Intense THz pulses from ZnSe and 6H-SiC ILAPCAs excited by femtosecond laser pulses.

As described in section 2.3.2, the best and easiest way to generate intense THz pulse from LAPCAs is to work with wide bandgap semiconductor crystals. We described that ZnSe and 6H-SiC LAPCAs showed promising results when excited by the second harmonic of an amplified Ti:Sapphire laser. Consequently, the next step was to fabricate ZnSe and 6H-SiC LAPCAs with an interdigitated structure [133]. To this end, the first ILAPCAs were manufactured using a polycrystalline ZnSe substrate. The antenna electrodes have been deposited using a standard photolithography technique. The ILAPCA structure was composed of 24 open-ended microstrip electrodes with a bright gap size equal to the dark gap size with a dimension of 0.6 mm, and electrode length and width of 22 mm and 0.4 mm, respectively. The gap size of the antenna was

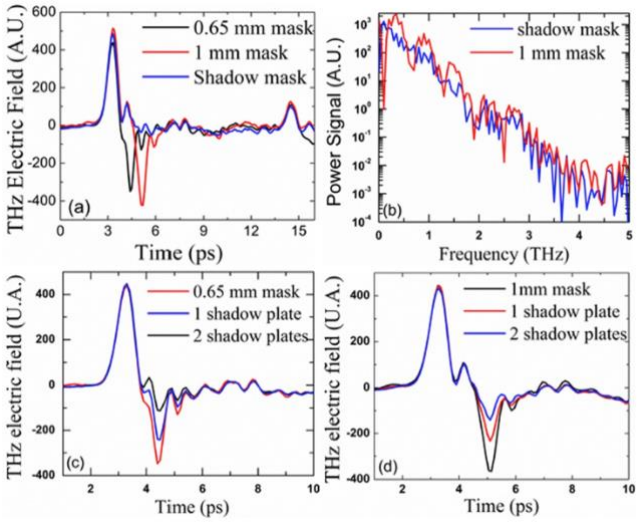

Figure 2-22 Waveforms and spectra of THz pulses generated ZnSe ILAPCAs when used different thickness shadow masks

THz pulses shapes generated from the ZnSe interdigitated LAPCA (a), power spectra with a (blue line) shadow mask, and (red line) the 1 mm binary mask (b), the THz pulse shapes obtained with the 0.65 mm and 1 mm (d) binary mask, (c) and (d) respectively [133].

large enough to allow the ILAPCA to work in the screening regime rather than in the space-charge screening regime. The ILAPCA proposed was covered with a shadow mask or a quartz binary mask with a thickness of 0.65 and 1 mm. The active illuminating area was 1.5 cm^2 and 3.0 cm^2 when using the shadow and the binary mask, respectively. The waveforms of the THz pulses generated by ILAPCAs covered by the 3 masks or a combination of shadow and binary mask are shown in Figure 2-22. One can clearly observe that the THz pulses are changing from a quasi-

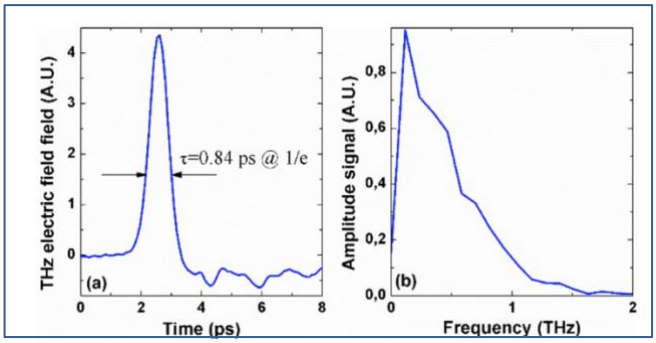

Figure 2-23 Waveform and amplitude spectrum of the THz pulses emitted from ZnSe LAPCAs with Ti/Au contacts.The antenna was covered by a shadow mask, and excited at 400 nm [203].

half cycle to a single-cycle waveform with significant degrees of freedom between the two, offering full control of the generated waveform. More importantly, when excited with a 10 Hz, 400 nm and up to 20 mJ of optical energy, the energy of the THz pulse generated from the ILAPCAs covered with the 1 mm mask is 1.7 larger than that generated by the shadow mask when the ILAPCA is biased and excited with the same parameters. The maximum energy of the THz pulses was found to be 3.6 μJ when the ILAPCA was biased at 47 kV/cm, excited with a fluence of 0.55 mJ/cm^2, which was 2.5 times larger than the saturation fluence, and covered with the 1mm binary mask. The corresponding THz peak field was evaluated as 143 kV/cm. Following the same approach, Ropagnol *et al.* further improved the peak field strength of the emitted THz pulses by significantly increasing the surface area of the ILAPCA with an active surface of 4.4 cm^2 when covered by a shadow mask [201]. The interdigitated antenna structure consisted of 35 identical electrodes with an equally bright and dark gap size of 0.7 mm. The illuminated active area was 35% of the total area of the antenna. The whole antenna structure was covered by an Al_2O_3 encapsulation layer with a thickness of 300 nm, which also acts as an antireflection layer. The ILAPCA was illuminated using the second harmonic of an amplified Ti:Sapphire laser with up to 24 mJ pulse energy, operating at a repetition rate of 10 Hz. Despite this relatively low repetition rate of the laser, the signal-to-noise ratio of the detected electric field was relatively high, with an amplitude signal-to-noise ratio of around 500 with only one scan. This value was possible because the pulsed bias voltage was set to be only half the repetition rate of the laser and acts like an electronic chopper [202]. The waveform of the THz pulses is a quasi-half cycle with a peak frequency located at 0.12 THz and the main frequency components below 1 THz (Figure 2-23). The maximum energy of the THz pulses was found to be 8.3 μJ when the ILAPCA was covered by the shadow mask, biased at 42 kV/cm and excited with 15 mJ of optical energy. The corresponding calculated peak electric field was slightly above 0.3 MV/cm. Despite having a

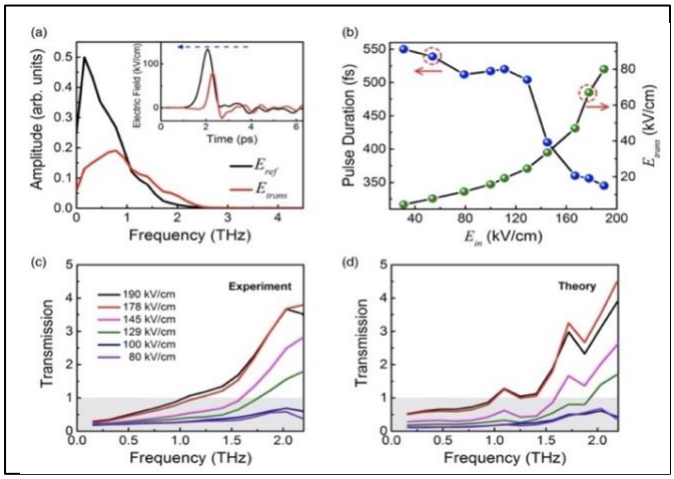

Figure 2-24 Experimental results on n doped InGaAs thin films under the excitation of intense THz pulses (a) The amplitude of the transmitted THz pulses through the bare substrate (E_{ref}) and the InGaAs sample (E_{trans}) with the incident peak field of 190 kV/cm, (b) Field dependence of E_{trans} and half-cycle duration (amplitude FWHM) as a function of the incident peak field E_{in} in air. (c) Transmission spectra at various incident fields, (d) Calculated transmission spectra based on the described model [24].

much higher THz pulse energy, this peak electric field strength is much lower than the peak intensity of the THz pulses emitted by the $LiNbO_3$ source with the pulse-front-tilt technique [203]. This is because the beam radius spot size was 1.17 and 1.37 mm in the X and Y direction, respectively. These dimensions are much large than a diffraction-limited spot size of a THz beam generated by a $LiNbO_3$ crystal. Despite this difference in the THz peak electric field, in this specific case for this ILAPCA, the maximum ponderomotive energy of the THz pulses was calculated to be 15 eV, which is slightly higher than the ponderomotive energy of the THz pulses at 1 THz with an electric field of 1 MV/cm. In pursuit of increasing the intensity of THz pulses generated by ILAPCAs, we can easily imagine that increasing the area of the ILAPCA structure is a straightforward solution. However, the multiplication of the number of electrodes inside the antenna array strongly increases the total capacitance of the ILAPCAs, which leads to a limitation of the maximum THz energy radiated in free space [184]. Also, the high voltage pulse was stretched and distorted, limiting the maximum bias field that could be applied before the appearance of corona discharges [116].

To verify the large ponderomotive potential of these THz pulses, the nonlinear transmission inside an n-doped InGaAs thin layer deposited onto a semi-insulating InP substrate was studied using an open aperture Z-scan technique. With a measured peak field of 174 kV/cm, a maximum transmission enhancement of 12.7 was observed at the focus of the THz pulse. This transmission enhancement is 4.5 times larger than the observed transmission enhancement inside the same InGaAs layer sample, obtained with a peak field of 200 kV/cm and a peak

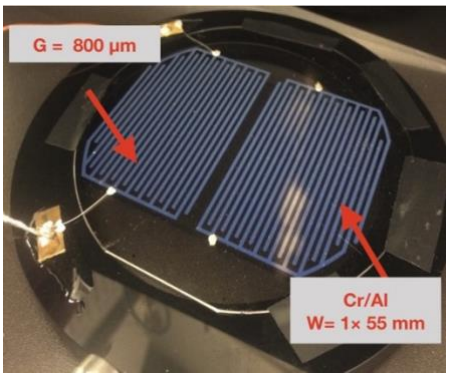

Figure 2-25 Top view of a typical 6H-SiC ILAPCA
The ILAPCA is composed of 38 electrodes with a gap size of 800 µm and a width and length of 1 and 55 mm respectively

frequency of 1.0 THz [201]. More importantly, it is shown that these THz pulses generated by the ZnSe ILAPCAs generated high-frequency components in the same n-doped InGaAs layer [24]. (Figure 2-24). In another recent study, the performance of the ZnSe and 6H-SiC ILAPCAs covered by shadow masks were compared. The two ILAPCAs did not have the same interdigitated structure with a gap size of 0.8 mm and 1.0 mm for the ZnSe and the 6H-SiC ILAPCAs, respectively. However, the optical beam dimensions, the optical energy at 400 nm and the bias field were kept the same at 3.9 cm, 6.5 mJ and 30 kV/cm, respectively. A photo of the studied 6H-SiC ILAPCA is shown in Figure 2-25. The THz pulses emitted by the ILAPCAs were detected by electro-optic sampling using a 0.3 mm (110) GaP crystal. With a peak electric field strength of 51 kV/cm, the 6H-SiC ILAPCA has exhibited slightly better performance than the peak field of the THz pulses generated by the ZnSe ILAPCA. As we can see in Figure 2-26 (a), the peak intensity of the emitted THz pulses from both antennas is observed at the same timing of 4 ps with a pulse duration (FWHM) of 590 fs. The major difference between the two pulses is in the negative tail, where we can observe strong oscillation of the electric field from THz pulses

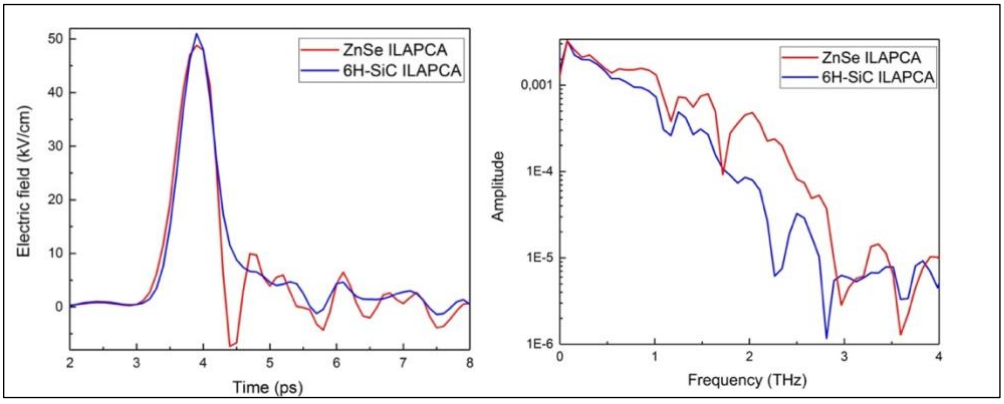

Figure 2-26 Waveforms (a), and the respective power spectra (b) of the THz pulses radiated from ZnSe and 6H-SiC ILAPCAs

generated by the ZnSe ILAPCAs. Since the experiment has been done in both cases in the same unpurged environment, these oscillations are not from water. These oscillations are due to the fast variation of the photocurrent density in the ZnSe substrate. In the case of the 6H-SiC substrate, the decay of the photocurrent is probably slower than that for the ZnSe crystal due to the indirect nature of the bandgap. In terms of spectra, both spectra have a peak frequency located around 100 GHz and extend up to 3.0 and 2.5 THz for the ZnSe and the 6H-SiC ILAPCAs, respectively. However, the spectra of the THz pulses generated by the ZnSe ILAPCA have an amplitude larger than the one of THz pulses generated by the 6H-SiC ILAPCA between 0.5 and 3 THz. This difference is attributed to the fast oscillation in the tail of the THz pulses generated by the ZnSe ILAPCA.

2.3.5.3 6H-SiC and 4H-SiC LAPCAs excited by sub-picosecond UV lasers.

As we described in section 2.3.4.3, both 6H-SiC and 4H-SiC LAPCAs have shown good performance for generating intense THz pulses under UV laser excitation. To generate high-intensity THz pulses, two 6H-SiC and 4H-SiC ILAPCAs were fabricated, and their performances were studied under the excitation of a KrF excimer laser with a wavelength of 248 nm, a pulse duration of 0.7 ps and an energy of 80 mJ [165]. The antenna structure was simple and consisted of 18 electrodes with the same bright and dark gap size and the same electrode width of 1 mm. The total illuminated area was 4.5 cm^2. Since only a shadow mask is used in this experience, only 25 % of the total area of the ILAPCA was illuminated (Figure 2-27). The electrode composition was Cr/Al, and the end of the electrodes was circular to allow the largest bias field to be applied without surface flashovers occurring at the edges of the electrodes. As expected, when both

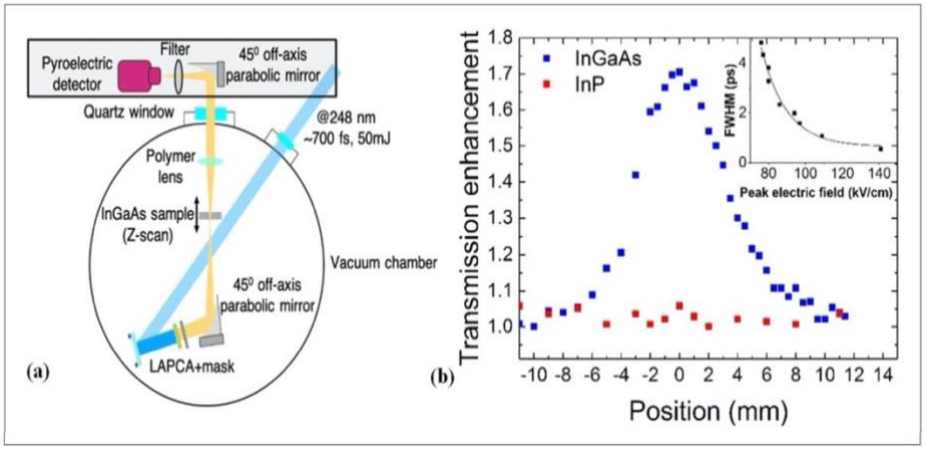

Figure 2-27 Z-scan experiment with the n-doped InGaAs thin film excited intense THz pulses generated by 4H-SiC ILAPCA

(a) Experimental scheme of Z-scan technique, (b) normalized transmission as a function of the Z-scan position for the InGaAs sample and the InP substrate [165].

ILAPCAs are excited with an optical fluence above the saturation fluence (1.2 mJ/cm^2), the 4H-SiC exhibits better overall performance than the 6H- SiC ILAPCA. The maximum energy of the THz pulses generated by the 4H-SiC ILAPCA was 2.3 μJ, with a bias field of 30 kV/cm. Using a Michelson interferometer, the measured time duration of the half-cycle pulse was around 2.2 ps FHWM. This duration is approximately 4 times longer than the pulse duration of the THz pulses emitted by the ZnSe ILAPCA when excited at 400 nm laser beam with 50 fs duration. Consequently, the spectra of these THz pulses show a peak frequency located at 50 GHz with a cut-off frequency at 400 GHz. The latter can be described as sub-THz radiation. The main reason for this longer duration of THz pulses and these sub-THz frequencies is explained by the much longer duration of the laser pulse [67,166]. However, there is also the effect of carriers being excited into the satellite valley since the photon energy of the laser are much larger than the bandgap of the substrate [127,128,167,204]. By placing the 4H-SiC ILAPCA in a vacuum chamber, the maximum bias field was increased up to 64 kV/cm before the corona discharge occurred. In this condition and with an optical energy of 54 mJ, the measured THz energy was 11 μJ, the highest THz pulse energy ever generated by ILAPCAs to date. The corresponding THz peak radiation field was calculated as 117 kV/cm. Although this peak field is relatively small, the associated ponderomotive energy was as large as 60 eV. Using these THz pulses with higher ponderomotive energy, an open Z-scan experiment was performed to demonstrate the non-linear effect in the n-doped InGaAs layer. An increase in non-linear transmission of 1.7 times was observed (Figure 2-27). This transmission enhancement is relatively low, and we believe that the relatively high scattering rate into the satellite valley of InGaAs limits the maximum kinetic energy that electrons can gain over the whole duration of the half-cycle pulse.

2.4 TECHNIQUES FOR THE DETECTION OF THZ RADIATION

The detection of the radiated THz pulses is also significant, as is the process of THz wave generation. Therefore, in this section, we briefly outline some common techniques used for the detection of THz pulses. The detection of THz pulses requires the use of different techniques according to their specific characteristics and properties. Since it is possible to generate pulsed and coherent THz radiation, we can divide THz detectors into two categories. The detectors capable of temporally resolving the electric field, which will be experimentally associated with pulsed THz sources, and those that perform quadratic measurements (intensity) on the incident fields, and which are well suited to continuous wave or incoherent sources.

2.4.1 Coherent detection

Coherent detection provides information on the phase and intensity of radiated THz pulses. This technique consists in coupling the generation and detection processes of the radiated THz pulses using a single fs laser beam. Coherent detections require the use of a variable optical delay line to vary the delay between the THz pulse generated from the emitter and the (fs) probe

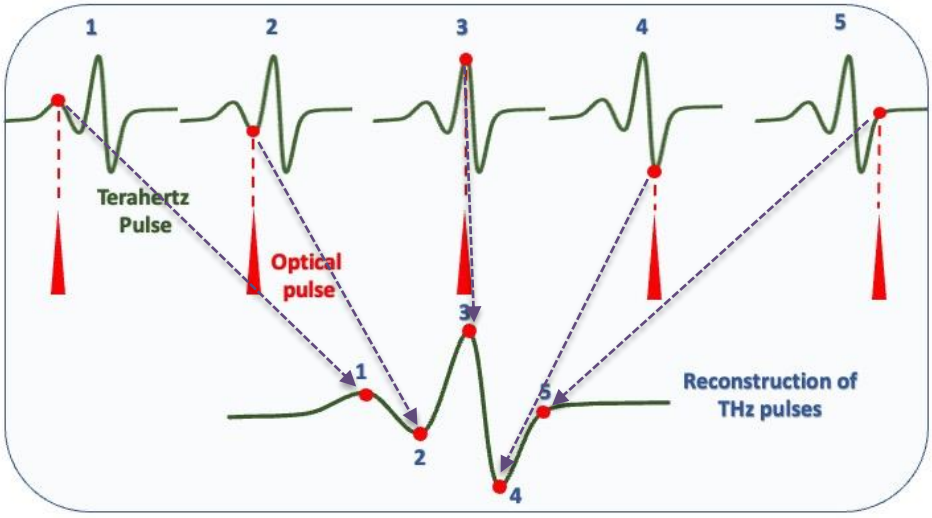

Figure 2-28 Illustration of the principle of coherent THz detection

laser pulse of the detector. This variable delay between THz and optical pulses with repeated measurements allows obtaining the whole information on the detected THz waveforms from a photoconductive detector. Figure 2-28 describes the principle of coherent detection for stationary signals. We can obtain the spectrum of THz pulses detected in the time domain by applying a Fourier transform to the acquired time-varying voltage (proportional to the THz field transient). For time-domain spectroscopy studies, these spectra are compared with and without THz absorbing material between the emitter and detector to obtain the THz absorption spectrum. We distinguish three methods for coherent detection: electro-optical sampling, photoconductive detection, and air coherent detection (ACD).

2.4.2 Photoconductive detection

Among the most conventional coherent detectors, photoconductive detection (PCD) is a widely used device for the detection of THz radiation. This technique consists of using a PCA that is similar in every respect to that used for the generation of THz pulses. The first demonstration of the detection of THz radiation using PC sampling coincides with the early 1980s [114,205–207]. In this study, two identical PCAs with Hertzian dipoles integrated into Silicon on Safire (SOS)

substrates were used symmetrically on opposite sides, and the detected electromagnetic pulses achieved an FWHM of 2.3 ps.

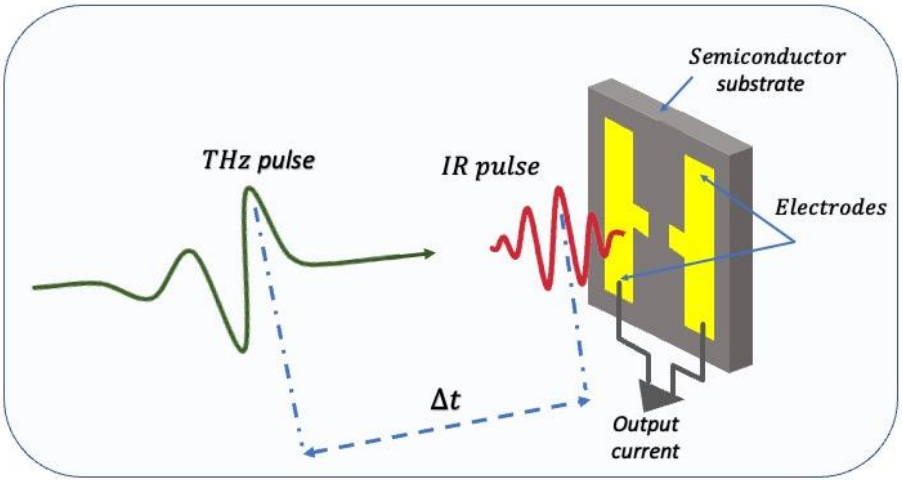

Figure 2-29 Schematic illustration of THz detection using PCA

The THz photoconductive detectors operate on the same principle as the THz wave generation process from photoconductive emitters. The optical probe pulse is focused across the gap between the electrodes. The optical photons, having higher energy than the band gap of the semiconductor crystal, are absorbed by the material. Therefore, free charge carriers are created in the conduction band, increasing the surface conductivity. In contrast to THz emission processes, the detection of THz pulses from PCAs relies on the photocurrent generated by the acceleration of free charge carriers, which is driven by the incident THz electric field. The photocurrent generated will be collected at the antenna terminals and will be proportional to the THz electric field and the charge carrier density. It should also be noted that the direction of the current depends on the polarity of the THz field. Figure 2-29 illustrates the principle of the photoconductive detection technique. The recovery of the THz waveform from PCA is given by the following equation [93].

$$\mathrm{J_s(t)} = \int_{-\infty}^{\infty} \sigma_s(\mathrm{t-t'})\, \mathrm{E_{THz}(t')dt'} \tag{2.4.1}$$

where E_{THz} the electric field of the THz pulses, σ_s is the surface conductivity and t is the time pulses and which the probe pulse enters the antenna, respectively. As illustrated in equation 2.4.1, the detected photocurrent $\mathrm{J_s}$ from the PCA is not directly proportional to the THz electric field. The temporal variation of the surface conductivity and thus the characteristics of the semiconductor of the receiver antenna and of the probe pulse play an important role in the shape

of the detected THz pulses. For the fabrication of photoconductive detectors, LT-GaAs is the most used semiconductor due to their sub-picosecond charge carrier lifetime. To minimize the influence of conductivity, for the fabrication of the THz PCA detector, it is necessary to use a material with ultra-fast charge carrier recombination time. On the other hand, the duration of the probe pulse and charge carrier lifetime are the factors influencing the bandwidth of detected THz pulses. Using a probe pulse duration of 15 fs, the bandwidth of THz pulses detected by arsenic-doped GaAs and proton-bombarded InP PCAs by ion implantation extended up to 30 THz [209,210]. Another factor influencing the detected THz pulses is the geometry of the antenna electrodes. It has been shown that as the length of the electrodes increases while keeping the inter-electrode distance constant, the amplitude of the detected signal increases. However, the peak frequency of the detected THz pulses shifted to lower frequencies with longer antenna electrodes [208].

2.4.3 Air-Biased Coherent Detection

The concept of air-biased coherent detection (ABCD) consists in focusing the THz pulses and the intense femtosecond laser beam together between two biased electrodes. By detecting the intensity of the second harmonic as well as the temporal variation of the fundamental and second harmonic beams, we can construct the amplitude of the THz pulses. The second harmonic response induced by the interaction of the fundamental laser field and the electric field of the radiated THz pulse is described as follows [211]:

$$E_{2\omega} = \chi_{air}^{(3)} E_{\omega} E_{\omega} E_{THz} \tag{2.4.2}$$

Here, $\chi_{air}^{(3)}$ third order susceptibility term of air, $E_{2\omega}$, E_{ω}, and E_{THz} are the electric field amplitude of second harmonic, the fundamental, and THz pulses, respectively. From equation 2.4.2, we can see that the electric field induced second harmonic generation is proportional to the THz electric field. However, in practice, since we are measuring the intensity or power of the second harmonic, and the intensity of the measured signal is proportional to the square of the THz electric field, the phase information cannot be extracted from the direct measurement. To achieve a coherent measurement, a method based on the mixing of the second harmonic signal with a local oscillator at a frequency of 2ω has been proposed. This local oscillator interferes with the second harmonic induced by the THz field, as expressed in the following equation:

$$I_{2\omega} = |E_{THz}|^2 = (E_{2\omega}^{THz} + E_{2\omega}^{LO})^2 = (E_{2\omega}^{THz})^2 + 2(E_{2\omega}^{THz})(E_{2\omega}^{LO}) + (E_{2\omega}^{LO})^2 \tag{2.4.3}$$

Here, $E_{2\omega}^{LO}$ is the second harmonic local oscillator created by the second harmonic of the white light produced by the laser. This local oscillator depends on the intensity of the probe beam In the case where the probe intensity is above the air ionization threshold, the local oscillator becomes strong enough and the second term in equation (2.4.3) becomes dominant, and therefore $I_{2\omega} \propto \mathrm{E}_{\mathrm{THz}}$ will lead to the coherent detection [212].

2.4.4 Electro-optic sampling detection

Electro-optic sampling (EOS) is another commonly used technique to detect THz radiation. The detection principle of the THz pulses through EO is based on the Pockels effect. Pockels effect is an optical phenomenon in which the refractive index of a non-centrosymmetric medium varies linearly with an applied static electric field. Therefore, field-induced birefringence will occur within the medium. In other words, EOS detection consists of a temporal overlapping of a femtosecond (probe) pulse and a THz pulse inside a detector crystal (such as ZnTe, CdTe, oriented <110) with non-centrosymmetric characteristics. Therefore, changing the amplitude and orientation of the THz pulse polarization will induce a change in the birefringence of the EO crystal, leading to a phase shift of the femtosecond laser pulse that changes its polarization state. The measurement of this polarization state with two crossed analyzers and a differential detector allows for finding the amplitude of the THz field. By modifying the delay between the two pulses, we can then sample the THz electric field waveform in the time domain. The schematic illustration of the detection process by the electro-optical sampling technique is depicted in Figure 2-30. As Figure 2-30 (a) illustrates, the linear polarization of the probe beam remains the same after

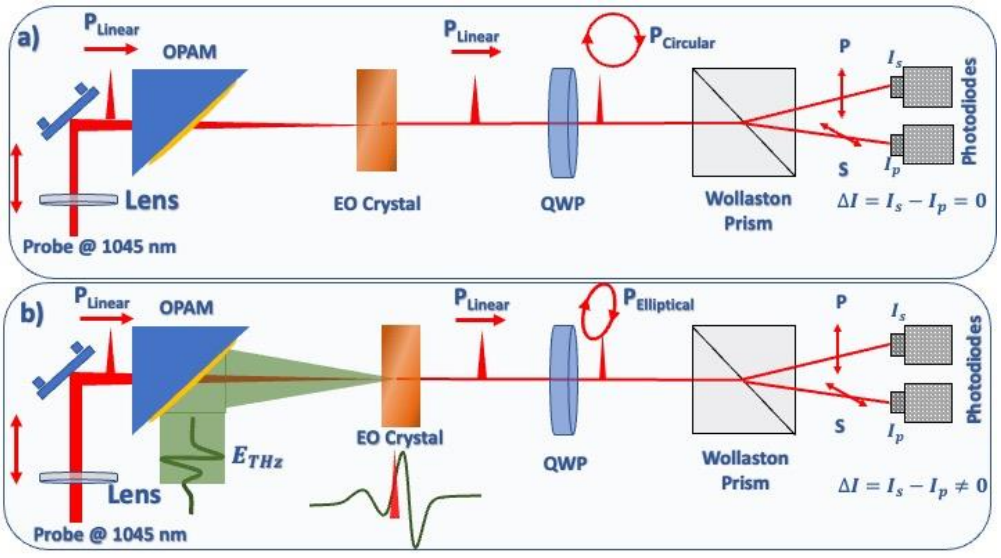

Figure 2-30 Schematic illustration of the detection of THz pulses by electro-optical sampling technique (a) in absence and (b) in presence of THz waves

propagating through the detector crystal when the THz field is absent. After the probe beam passes through the crystal, the linear polarization of the probe pulse is transformed into a circular polarization using a quarter-wave plate (QWP) oriented at 45° to the electric field associated with the probe pulse. Then, using a Wollaston prism will allow us to separate the parallel component (noted "s") and the perpendicular component (noted "p") of the circular polarization of the probe pulse. Then, two beams with orthogonal polarization states will be detected by a pair of balanced photodiodes. Without the THz pulse, since the probe pulse is circularly polarized, the intensities of the "s" and "p" components will be identical. Therefore, the differential signal at the output of the photodiodes is zero. On the other hand, when the THz pulse propagates together with the probe pulse in the crystal, the THz electric field induces a degree of birefringence that is proportional to the THz amplitude (Figure 2-30 (b)). Such a birefringence will induce a rotation to the linear polarization of the probe beam. Therefore, the angle between the electric field of the probe pulse and the neutral lines of the QWP will be different from 45°. After the propagation of the probe pulse through the QWP, the polarization state of the probe becomes elliptical, and thus the intensity difference between the " s " and " p " components is nonzero. This intensity difference will be proportional to the THz electric field. Therefore, by varying the delay between the laser probe pulse and the THz electric field, we will achieve the detection of THz pulses by EOS.

2.4.5 Incoherent THz detection techniques

Incoherent detection techniques are based on intensity-sensitive quadratic incident field detectors. Although incoherent detection is not sensitive to the phase and frequency of the detected electric fields, the obtained information on the detected THz pulses can be used for spectroscopy studies. Another advantage of incoherent detection techniques is their ease of operation compared to coherent detection. For example, using local oscillators such as the QCL or optical photomixers, it is possible to obtain the power and spectra of THz pulses detected by heterodyne mixing measurements. In addition, homodyne detection techniques such as shifted wave interference allow deducing the frequency content of detected THz pulses by Fourier transformation.

2.4.6 Bolometric detection

The bolometer consists of an absorbent element, such as a thin metallic film, which is connected to a constant heat reservoir that provides the body with a constant temperature. When incident radiation hits the absorbing layer, it will cause an increase in the temperature of that layer

compared to the temperature of the heat reservoir, thus the more power is absorbed the higher the temperature will be. The intrinsic thermal constant, which determines the speed of the detector, is equal to the ratio between the heat capacity of the absorbing element and the thermal conductance between the absorbing element and the heat source. Among the different bolometric detection systems, hot electron bolometers (HEB) and superconducting bolometers are commonly used to enable more efficient THz detection, but they require the use of complex cryogenic procedures.

2.4.7 Golay Cells

Golay cells are an optoacoustic detector commonly used in infrared and THz spectroscopy. They consist of a filled gas chamber with an absorbing substance and a flexible diaphragm or membrane. The heated gas expands inside the chamber when infrared or THz radiation is absorbed. Due to the expansion of the gas, the pressure causes the deformation of the membrane. This membrane is then illuminated, and the reflected light is measured by a photodiode. The movement of the membrane produces a variation of the reflected light, which changes the signal in the photodiode. The Golay cell promises a sensitive and flat response over a wide frequency range. However, this THz detector has several disadvantages such as a higher fragility (thin membrane) and a slow response of the order of 10 ms. In addition, its high sensitivity to mechanical vibrations, its transient response depending on the ambient pressure, as well as its high cost can be considered drawbacks of these detectors.

2.4.8 Pyroelectric detectors

Pyroelectric THz detection systems are also based on the temperature change induced by the absorption of radiation. Some crystals exhibit pyroelectric behaviour when heated. As a result, a difference in temperature produces a voltage transient which provides information on the intensity of the incident radiation. This type of detection is particularly interesting in passive presence detection devices

CHAPTER 3 STUDY OF TERAHERTZ RADIATION PERFORMANCE OF YTTERBIUM-LASER-BASED OPTICAL RECTIFICATION SOURCES

3.1 EXPERIMENTAL STUDY

In this section, we present our first experimental study conducted on THz wave generation using BNA crystals. As discussed in the previous section, BNA crystals have been widely used for the generation of high-intensity THz pulses pumped by amplified lasers with repetition rates of 100 Hz to 1 kHz. However, the performance of the BNA crystal and its potential to generate THz radiation at a higher repetition rate and long pulse duration of the excitation wavelength in the range of 1μm was still unknown until now. To this end, we first studied the radiation performance of BNA with respect to crystal thickness. Therefore, the THz radiation generation using 0.63-, 0.81-, and 1.09-mm thick BNA crystals was studied when pumped by an Ytterbium laser with a central wavelength of 1045 nm. Then, the THz radiation performance of the most efficient BNA crystal will be compared to that of a 0.8 mm thick CdTe crystal under optimum excitation conditions in a nitrogen-purified environment.

3.1.1 Setup for the generation and detection of THz pulses

For the generation and detection of THz pulses, in this study, we used a conventional THz-TDS setup using an Yb-doped oscillator laser with pulse duration and repetition rate, respectively, of 238 fs and 63 MHz (HighQ-2, Spectra-Physics). As depicted in Figure 3-1, the main laser beam with an input power of 520 mW is first divided into two parts using a UV fused silica (UVFS) beam splitter, and 90% of the total power is used for the THz wave generation process, with the remaining 10% used to probe the generated THz pulses. Then the pump beam is focused onto the emitter crystal by an antireflection (AR) coating lens with a focal length of 50 mm. Free-space-generated THz pulses from the crystal are first collected by a pair of 2-inch off-axis parabolic mirrors (OAPMs) and then guided by a pair of 3-inch OAPMs onto the EO detector crystal. The THz pulses are detected by a double-sided polished 1 mm thick CdTe crystal with a size of (5x5mm) using a standard electro-optical (EO) sampling technique. The emitted THz radiation was chopped with a mechanical chopper at a frequency of 230 Hz, and the output signal from a pair of homemade photodetectors is amplified using a Stanford Research RG-830 lock-in amplifier.

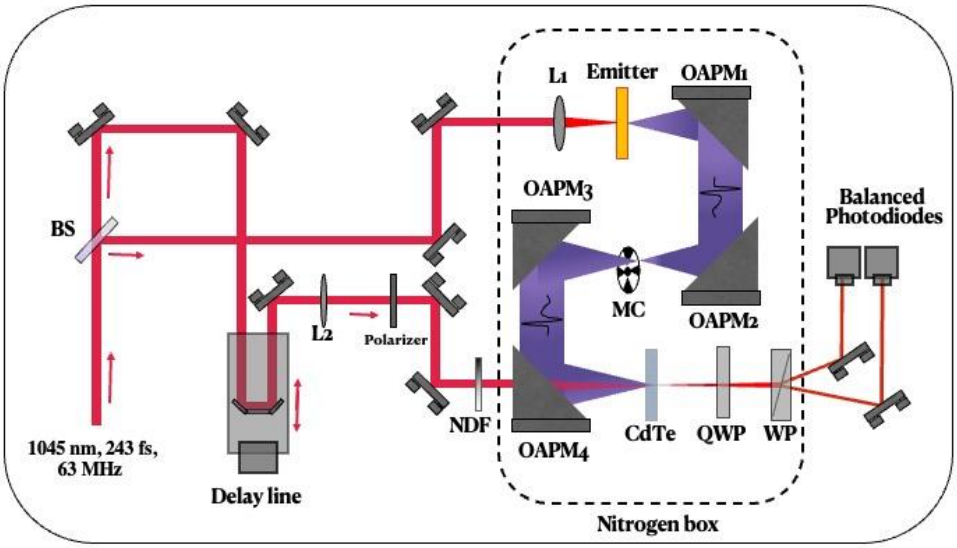

Figure 3-1 The scheme of the experimental setup used for the THz wave generation from the BNA and CdTe crystals

3.1.2 Results and Discussion

The waveforms and spectra of the THz pulses radiated by the BNA crystals are shown in Figure 3-2. To ensure a fair comparison of the radiation performance, all crystals were studied under the same conditions, when illuminated at the average pump power of 450 mW while holding the probe power constant at 27 mW by controlling the intensity with a metallic neutral density filter during all measurements. Due to the weakness of the THz pulses generated by the crystal emitters, precise measurement of their intensity using infrared or pyroelectric sensors is challenging. Consequently, the amplitude scales used to quantify THz radiation in this study are expressed in arbitrary units. As we can see in Figure 3-2 (a), the main THz pulses radiated from BNA crystals have the same single-cycle waveform, which is followed by long-lasting oscillations extending to 8 ps, originating from water vapor absorption and absorption of phonon. The duration of the main pulse is ~640 fs (intensity FWHM). Thus, THz pulses radiated from the 1.09 mm thick BNA have 1.5- and 2.1 times higher efficiency than the 0.81- and 0.63-mm thick BNA crystals, respectively. In addition, the respective THz power spectra calculated by Fourier transform show that the bandwidth of the radiated THz pulses broadens as the crystal thickness is increased (Figure 3-2 (b)). A larger bandwidth extending beyond 2.5 THz was observed from the crystal with a thickness of 1.09 mm. However, all the spectra have main dips around 1.8THz, and 2.3THz, which can be attributed to phonon absorptions in BNA. These typical dips in BNA crystals have also been observed in previous studies which are one of the main limiting factors to the performance of BNA for the application in spectroscopy [213].

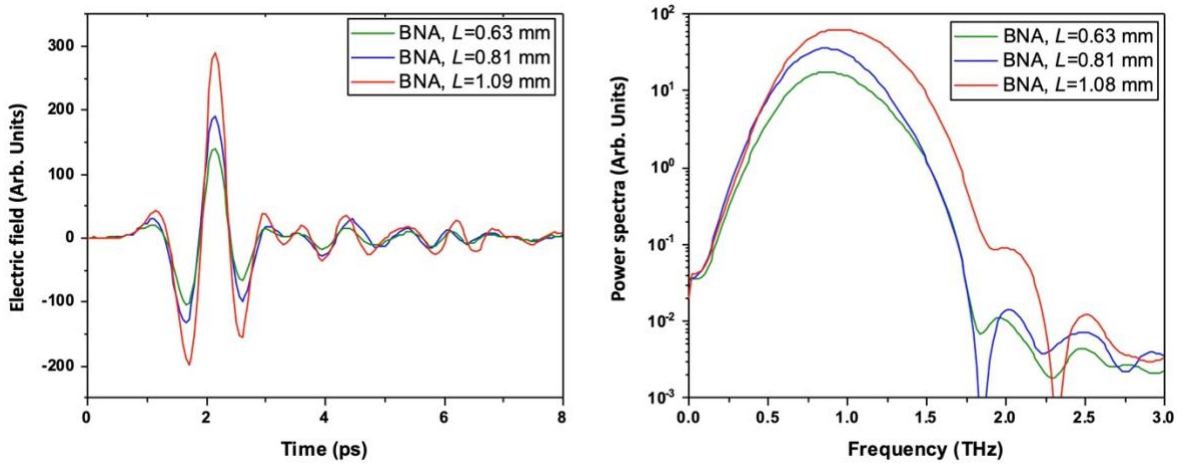

Figure 3-2 (a) waveforms and (b) FFT spectra of THz pulses emitted by BNA crystals

On the other hand, following this previous comparative study, the optical-to-THz conversion efficiency of the 1.09-mm-thick BNA crystal was also compared to that of a 0.80-mm-thick CdTe crystal under a purged nitrogen environment. To this end, after optimizing the transmitter and detector crystals, the experimental setup was purged using a photo chamber, and ultra-dry nitrogen was injected under pressure to remove moisture and water vapor. Then the THz signals were recorded in the optimal condition with a humidity level below 3%. As shown in Figure 3-2 (a), the decrease in humidity significantly improved the signal-to-noise ratio and a more than twofold improvement of the peak amplitude in the radiated THz pulses was observed from the 1.09-mm-thick BNA crystal. In addition, the THz radiation efficiency of the BNA was 1.8 times higher than that of the THz pulses radiated by CdTe. However, with a monocycle waveform, the main THz pulse emitted by CdTe has a shorter duration (~2.5 ps) than the duration (~2.7ps) of THz pulses emitted by the BNA. On the other hand, the respective calculated FFT spectra show that the bandwidth of the THz radiation from CdTe extends up to 2.5 THz, while the THz spectrum corresponding to the BNA has a bandwidth larger than 3 THz. Nevertheless, it is important to note that the THz spectrum of the BNA crystal is limited to 2.1 THz due to a strong phonon mode existing around 2.3 THz (Figure 3-3) (b)). This can be attributed to the lower THz generation at this frequency, which is caused by the higher absorption coefficient of the BNA crystal at about 2.1 THz [214]. In summary, our experimental study on THz generation using BNA with different crystal thicknesses at high (63 MHz) repetition rates using 1 μm Yb lasers with relatively long (~240 fs) pulse durations showed that the intensity and bandwidth of the radiated THz pulses increase with respect to crystal thickness. This observed higher optical-to-THz conversion efficiency and the respective spectrum obtained from the larger crystal could be attributed to the optimal phase-matching condition between the group and phase velocities of the optical and THz

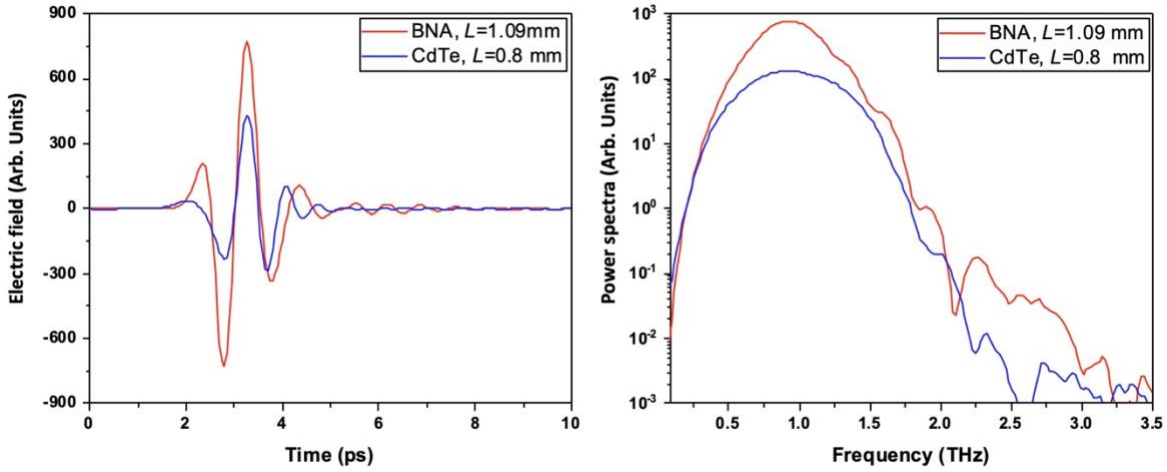

Figure 3-3 (a) waveforms and (b) FFT spectra of THz pulses emitted from BNA (red curve) and CdTe (blue curve) crystals in a nitrogen purged environment

pulses in the crystal [215]. In addition, by comparing the performance of BNA and CdTe crystals for THz generation through OR, we show that BNA has a higher potential for THz emission when using a Yb laser. This is due to BNA's better velocity matching conditions because of the relatively small difference between the optical group index and the THz refractive index. Indeed, as described in table 2-1, due to a higher d_{eff}, and n_{NIR} at 1064 nm, the calculated FOM for BNA is much higher than that of the CdTe. Therefore, achieving a wider bandwidth extending to 3.5 THz with an efficient THz generation allows the BNA to be assessed as a higher-potential THz source suitable for pumping using commercially available ultra-compact Yb-doped laser sources delivering high-quality fs pulses in the 1 μm range. However, it is worth mentioning that the bandwidth of the THz pulses generated from BNA when driven by longer pulses results in a significant narrowing in the spectrum compared to cases using shorter pump pulses [213,216]. This can be attributed to the fact that detecting THz pulses with the EO sampling using a shorter duration of the probe beam increases the maximum peak electric field and increases the detected bandwidth. In addition, lattice resonances resulting from absorption in the THz region can limit the intrinsic speed of electro-optical materials, which in turn can limit the perforation of the detected THz pulses via EOS [217].

CHAPTER 4 GENERATION OF INTENSE HALF-CYCLE ELLIPTICALLY POLARIZED THZ PULSES BY ZnSe ILAPCAs

4.1 Experimental study

In this section, we present a new experimental approach for generating intense quasi-cycle THz pulses with variable polarization [218]. This new method consists of the time delay between cross-polarizations of the radiated THz pulses using different ZnSe ILAPCA designs with horizontal and vertical electrodes. By temporally shifting two cross-polarized THz pulses with respect to each other, the polarization states of the radiated THz pulses were tuned from linear to quasi-circular over a quarter cycle. To provide this time delay between two generated THz pulses with orthogonal polarization, phase masks with various thicknesses were used to cover the horizontal and vertical electrodes. Therefore, the high-intensity THz pulses with peak field amplitude up to 70 kV/cm were generated with polarization states ranging from linear to quasi-circular polarization using the proposed method. To our knowledge, this peak field strength is the highest value achieved in quasi-elliptical THz pulses generated to date. In addition, the maximum field strength, and temporal and spectral shapes of the radiated THz pulses remain constant for all polarization states and remain collinear throughout the space propagation volume. These unique properties of the high-intensity, quasi-circular THz pulses generated by this recent technique present a great advantage for the study and continuous monitoring of the nonlinear properties of polarization-selective materials.

4.1.1 Setup for generation and detection of intense THz pulses by ZnSe ILAPCA.

The top view of the ZnSe ILAPCA and one of the respective delay masks covered by a shadow mask are shown in Figures 4-1 (a) and (b), respectively. For the fabrication of ILAPCAs, the conventional photolithography technique has been utilized. Chromium and aluminum (Cr/Al) electrodes having a thickness of 185 nm were deposited on a 3-inch diameter ZnSe substrate with a thickness of 1.5 mm. The ILAPCA used in this study consists of a 3-inch diameter ZnSe substrate with a thickness of 1.5 mm. With a total thickness of 185 nm, chromium, and aluminum (Cr/Al) electrodes were deposited on the substrate with a conventional photolithography technique. The overall diameter of the antenna consisting of 6 units of alternating horizontal and vertical electrodes is 62 mm. Each antenna has the same inter-electrode distance of 0.8 mm, which is large enough to avoid the space charge screening effect. The total illuminated area of

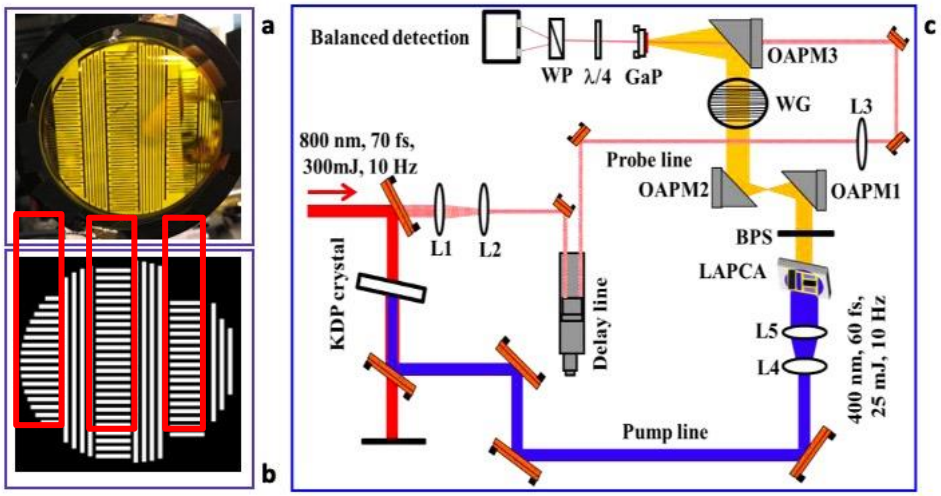

Figure 4-1 Photography of ZnSe ILAPCA (a), its shadow mask (b), the schematic representation of the experimental setup. The rectangular area with the red line represents the area covered by the shadow mask [218]

the vertical and horizontal electrodes is about 4.3 cm^2, after covering the antenna with a shadow mask, which is almost the same area as the vertical electrode units. To avoid destructive interference of the THz pulses generated in the far field, it is necessary to use a shadow mask on the delayed mask to cover the adjacent electrodes (vertical tree units) of the antenna. Various delay masks with thicknesses of 0.12, 0.20, 0.25, and 1 mm separately used to cover the horizontal electrodes allow changing the polarization states of the generated quasi-half cycle THz pulses with equal amplitude from linear to quasi-circular corresponding to the thickness of the masks. The experimental setup for generating THz pulses from ZnSe ILAPCA is shown in Figure 4-2 (c). The ZnSe ILAPCA is excited by 15 mJ laser pulses with a duration and repetition rate of 60 fs and 10 Hz, respectively, at 400 nm. The ILAPCA is operated with maximum high-voltage pulses up to 2.25 kV, with a duration of 50 ns. The generated THz pulses were collected and guided to the detectors using two 3-inch and one 4-inch diameter off-axis parabolic mirrors (OAPMs). To control the time-dependent polarization component of the measured THz pulses, a metal grid polarizer is placed between the second and third OAPMs. The THz pulses were detected by a 300 μm thick (100) GaP crystal using the standard EO sampling technique by overlapping the probe pulses at 800 nm on the crystal.

4.1.2 Results and Discussion

The 3D waveforms of the radiated THz fields and their projections on the different axis for various mask thicknesses are shown in Figure 4-2. As shown in Figure 4-2, the use of the

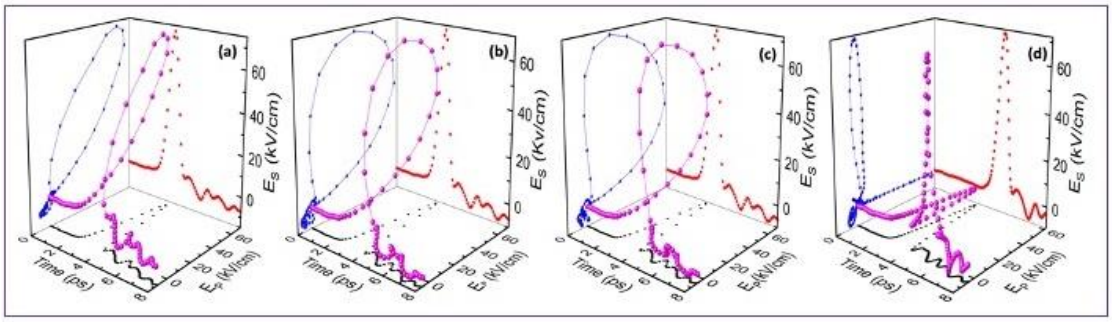

Figure 4-2 3D waveform of the THz pulses from ZnSe ILAPCA when pumped at 400 nm. Ep, and Es are the THz electric field with the horizontal and vertical polarizations and their projection Es as a function of Ep with the different thicknesses phase masks [218].

delay masks with increased thickness from 0.12 to 1.0 mm allows the vertically and horizontally polarized THz pulses to be time-shifted by 0.2 to 1.7 ps, respectively. By increasing the time delay between vertically and horizontally polarized THz pulses from 0.4 ps to 0.5 ps, the polarization state becomes more elliptical, while by increasing the time delay between two orthogonally polarized THz pulses from 3.1 ps to 3.7 ps, the polarization state becomes more circular over a period of a quarter cycle. By replacing the shadow masks with a binary mask of 0.25 mm thickness, we can generate quasi-circularly polarized THz pulses over a half cycle. In our study, since only the vertical electrodes were covered by the delay masks, the rotation of the plane of polarization is left-handed. On the other hand, by changing the covering of the horizontal electrodes to vertical electrodes, we can change the rotation of the polarization from left to right. Figure 4-3 (a) illustrates the temporal waveforms (inset) and respective spectra of the horizontally and vertically polarized THz pulses generated by the ZnSe ILAPCA when covered by the 0.25 mm shadow mask. Calculated peak fields corresponding to horizontally and vertically polarized THz pulses are 68 and 71 kV/cm, respectively. The small difference between measured peak THz fields is due to a slight misalignment of the shadow mask in front of the antenna. As shown in Figure 4-2 (c), the combination of these two vertical and horizontally polarized pulses gives us a quasi-circular polarized THz pulse with a maximum field amplitude of 81 kV/cm at 3.4 ps. Since the peak field of radiated THz pulses from PCAs increases linearly with the applied bias field, we estimate a maximum peak field generated from ZnSe ILAPCAs of roughly 115 kV/cm for THz pulses with quasi-circular polarisation from the source provided in this work. Figure 4-3 (b) illustrates the dependence of the spectral phase difference between vertically and horizontally polarized THz pulses as a function of frequency when the ILAPCA is covered with 0.12-, 0.20-, and 0.25-mm thick delay masks. Since the thinner mask causes a slight difference in phase shift, the relative THz pulses have almost linear polarization. Likewise, a small difference was observed in the phase shift between the vertically and horizontally polarized THz pulses when the antenna

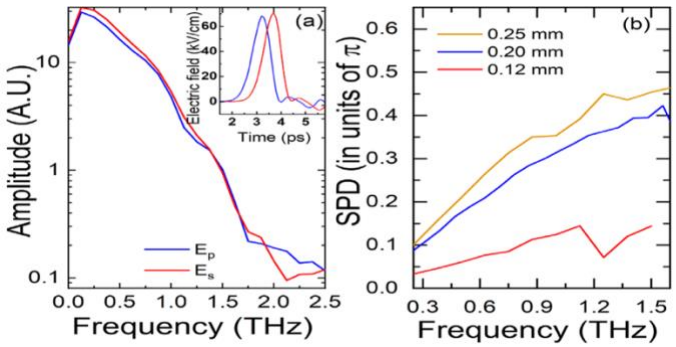

Figure 4-3 (a) spectra and waveforms (inset) of the radiated THz pulses with horizontal and vertical polarization from ZnSe ILAPCA (b) and spectral phase differences (SPD) between horizontal and vertical polarized THz pulses (b) The ILAPCA is covered with 0.25 mm delay mask and pumped at 400 nm [218].

is covered by the 0.20- and 0.25-mm thick delay masks. In addition, it is worth mentioning that, surprisingly, the spectral difference corresponding to the 0.25 mm thick delay mask is not π/2 across the entire spectrum compared to the same thickness of the binary mask (Figure 4-2 (c)). This can be attributed to the nature of our sub-cyclic THz pulses, which is significantly different from the circular polarization behavior of quasi-monochromatic light [219].

CHAPTER 5 FABRICATION AND CHARACTERIZATION OF YTTERBIUM-LASER-BASED TERAHERTZ PHOTOCONDUCTIVE SOURCES

This chapter outlines our experimental studies on the generation of THz radiation from microstructured dipole PCAs fabricated on SI-GaAs and CdTe substrates using the SHG of a mode-locked Yb-doped laser at 522 nm. In addition, the design and fabrication process we used to manufacture the PCAs will also be briefly introduced.

As mentioned in the previous chapter, due to their superior properties GaAs is a widely used material for THz wave generation and detection as a substrate for PCAs. CdTe is another compound semiconductor that has recently gained interest in THz technology. Recently, CdTe has become a popular material for solar cell fabrication due to its high absorption efficiency of ~97.3 % in the visible range, higher photon-to-charge conversion performance, and low production cost [220]. With its direct band gap of 1.44 eV at room temperature and maximum conversion efficiency of 32%, CdTe meets the requirements for efficient energy conversion in solar cells [221]. Another common application of CdTe is its use in the fabrication of certain optoelectronic devices such as Pockels cells [222,223], infrared and THz detectors [6], as well as gamma-ray [225] and X-ray detectors [226,227]. In addition, this crystal has also been widely used for generating THz radiation via OR under the excitation of Ti:Sapphire lasers [228] and optical parametric oscillators delivering optical pulses at 800 nm and 710-970 nm, respectively [229,230]. The recent study on THz generation and detection using a CdTe crystal pumped by an Yb amplifier and oscillator at wavelengths of 1025 nm and 1045 nm, respectively, showed that it exhibits 5- and 3-fold higher efficiency than the GaP crystal under optimal conditions [95]. However, the authors also demonstrated that two-photon absorption (2PA) in CdTe crystals could significantly limit THz generation via OR, even at low optical fluences when pumped by an amplified laser. Since the scaling of THz radiation from PCAs depends on bias voltage rather than pump fluence, they can be the most suitable sources for THz applications because of their relatively high optical-to-THz conversion efficiency when pumped by low-intensity laser pulses delivered by high repetition rate laser oscillators. Therefore, owing to its shorter carrier lifetime, ranging from 10's of ps to a few ns [231,232], high dark resistivity > 10^9 Ωcm [233], and relatively superior carrier mobility of > 1000 $cm^2V^{-1}s^{-1}$ [234], CdTe crystals have been studied, for the first time, for the generation of the THz pulses, as a substrate for PCA. Since CdTe and GaAs have almost the same direct band gap of ~1.44 eV, the THz emission of both

PCAs with the same metallic electrode design will be compared under the same condition pumped by the second harmonic of the Yb-doped oscillator at 522 nm, with a photon energy of 2.37 eV.

5.1 EXPERIMENTAL STUDY

5.1.1 Design and fabrication of PCAs

Figure 5-1 (a) and (b) shows the top optical microscopy view of one of the studied CdTe PCAs. For the fabrication of the antennas, we used the traditional photolithography method. Both the CdTe and SI-GaAs PCAs were fabricated with the same dipole-type geometry by depositing H-shaped metal electrodes directly on the readily available commercial substrates using a standard e-beam evaporation technique. We used <110> double-sided polished undoped CdTe substrates (from ACROTEC, Japan) with dimensions and thicknesses of 10 x 10 mm and 800 ± 50 µm, respectively. On the other hand, SI-GaAs PCAs were made of 500 µm thick commercial double-sided polished crystals (from MTI, Corporation, CA, USA), with a high resistivity and carrier mobility of 3.16 x10^8 Ωcm, and 4890 cm^2/Vs, respectively. The undoped 2-inch wafers with crystal orientation of <100> were cut into 10 x 10 mm pieces before the two-step cleaning process. The initial cleaning step was performed with organic solvents, using acetone, isopropanol, and methanol alternately for 10 min in an ultrasonic oven before rinsing with deionized water. The second step consists of acid cleaning, using the nanostrip for 5 minutes. Subsequently, the substrates were preheated at 180 ºC for 5 minutes and thermally annealed for 10 minutes at room temperature. This common thermal treatment allows removing the surface contaminants and terracing of the surface morphology of the substrates. As the following step, we used the Brewer CEE100 programmable spin-coater to deposit ~400 nm thick photoresists on the substrates and baked them at 115 ºC for 5 min before using the laser beam exposure process. Afterward, we

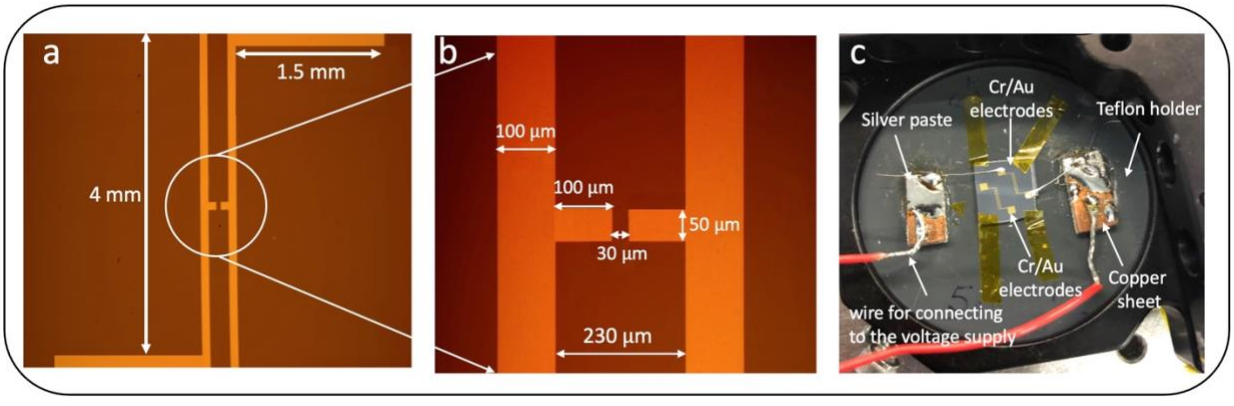

Figure 5-1 Optical microscopy image of the CdTe PCA (a) the top view of the antennas (b) 10 times magnification of the image (a) on the photoconductive gap, (c) Photography of one of SI-GaAs PCAs before testing

used a maskless lithography system (Heidelberg DWL-66 FS) to achieve high-resolution patterns on the substrates. H-shaped patterns with an interelectrode spacing of 30 μm with a width and length of 100 μm and 4 mm were exposed directly at the etching wavelength of 405 nm. Next, the samples were processed in a plasma chamber (Asher Gas-sonics Aura 1000) to remove polymers and organic contaminants using oxygen ions. Then 5 nm chromium (Cr) and 80 nm gold (Au) layers were deposited onto the substrate by the standard electron beam evaporation technique using the K. J. Lesker AXXIS tool. As the final step, we made a standard lift-off process to remove the photoresist and overlying the antenna electrodes. Before their characterization, each PCA was carefully placed on a center-perforated Teflon holder and then mounted on a 2-inch kinematic mirror mount, as shown in Figure 5-1 (c). Then the antenna electrodes were bonded to the external bias voltage source through the copper plates fixed on the Teflon holder using silver paste. Finally, the PCA was mounted on a compact three-axis macro-block bending stage (MBT602, Thorlabs) that allows precise three-dimensional alignment of the emitter through the focus of the pump excitation beam.

5.1.2 Experimental setup

The experimental setup for the generation of free-space THz pulses is presented in Figure 5-2. The THz pulses have been generated and detected using conventional transmission-mode THz-TDS. This setup allows the generation of THz pulses by PCAs and their detection by EOS. The laser source is a compact air-cooled Yb laser oscillator that generates pulses at a wavelength

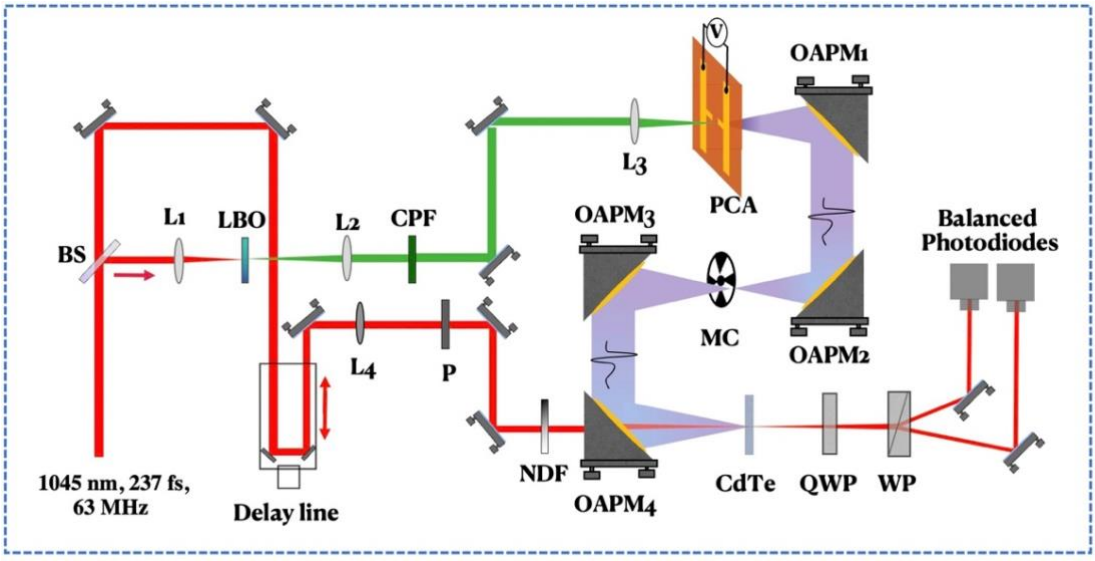

Figure 5-2 Schematic diagram of the THz-TDS experimental setup used for characterizing CdTe and Si-GaAs micro-dipole PCAs CPF coloured band pass filter, PCA photoconductive antenna, PM parabolic mirror, MC mechanical chopper, QWP quarter waveplate, PD

of 1045 nm, with an average power of 1.5 W, a duration of 238 fs, and a repetition rate of 63 MHz. For our experiments, we used 40% of the total laser power. Therefore, the laser beam at the fundamental wavelength of 1045 nm, with an average power of 620 mW, was first split by a UV-fused silica plate beam splitter, and 90% of the total laser beam was focused on a 3.7 mm thick (LBO) lithium triborate crystal (Eksma Optics, Vilnius, Lithuania) to generate the 522-nm pump beam, and the remaining 10% of the laser beam at 1045 nm is used to probe the THz pulses. After collimation, the pump beam was filtered using a colored bandpass filter (FGB37-A, Thorlabs, USA) and focused with a maximum power of 75 mW on the PCAs using an uncoated lens (f=50 mm, N-BK7, Thorlabs). The THz pulses emitted by the antennas were collected and guided by

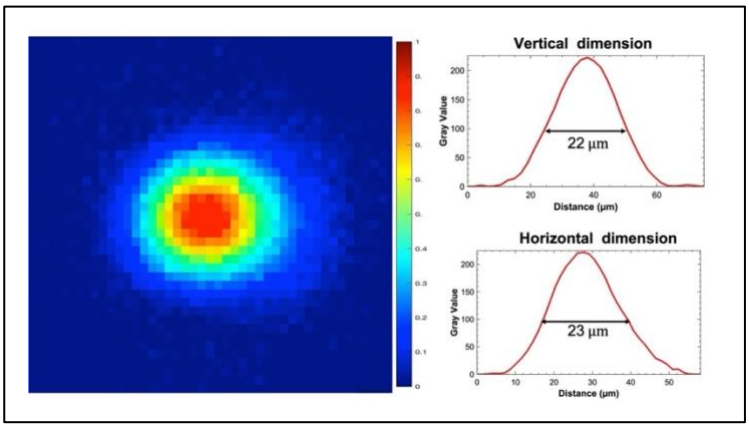

Figure 5-3 Spatial profile of the pump beam at 522 nm in the focus

two pairs of 2-inch off-axis parabolic mirrors onto the 1-mm- thick CdTe detector crystal, and their THz electric field was measured using balanced photodetectors via conventional EO- sampling technique. To make a synchronous detection and improve the signal-to-noise ratio of the THz pulses detected we used an SR830 lock-in amplifier. The antenna electrodes are biased by an external voltage source (Stanford Research Systems, model PS310/1250V-25) providing several hundred volts. To modulate THz pulses and stimulate the signal-to-noise ratio of the detected signal, we used a mechanical chopper at the focus of the THz beam with a frequency of 225 Hz for lock-in detection. The radiated THz pulses were detected at a time constant of 1s from the lock-in amplifier by controlling the probe-to-pump beam delay with a waiting time and step size of 3s and 0.1ps, respectively. The emitters are placed at the focus of the laser pump beam, whose optical spot sizer has been measured to be 22 µm using a Teledyne DALSA high-speed CCD camera (Genie HM640). Figure 5-3 shows the spatial intensity profile of the 522 nm SHG beam at focus. The calculated beam area at the focus is 3.45×10^{-6} cm^2.

5.1.3 Temporal waveforms and spectra of THz pulses by SI-GaAs and CdTe micro-dipole PCAs

Figures 5-4 shows the temporal waveforms and their associated Fast Fourier spectra of the radiated THz pulses when the SI-GaAs and CdTe PCAs were excited at the same pump power of 45 mW and biased at maximum external fields of 25 kV/cm and 58.3 kV/cm at 522 nm, respectively. Generated THz pulses from both antennas have similar monocycle waveforms,

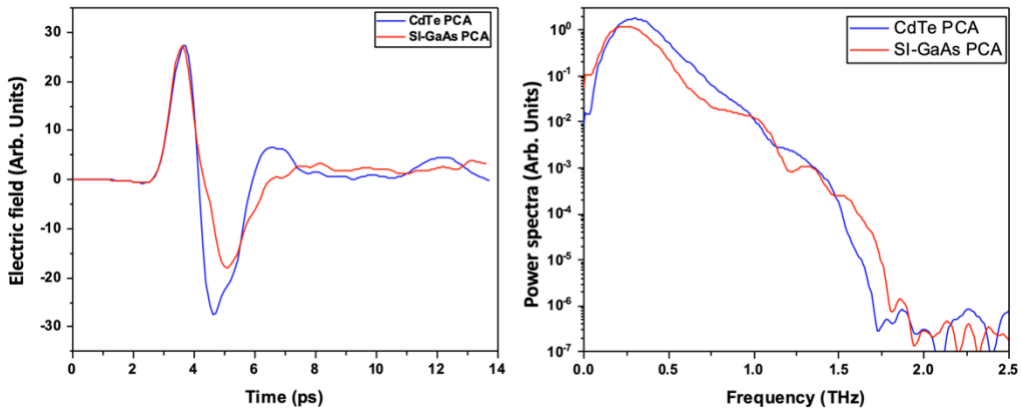

Figure 5-4 Waveforms and spectra of the THz pulses radiated from CdTe- and SI-GaAs PCAs

consisting of a main positive peak with a full width at 1/e maximum of 800 fs, followed by a long peak with opposite polarity. The width of the main THz pulse is estimated at around 3.7 ps. In addition, the negative amplitude of the THz pulses radiated from the CdTe PCA has 1.53 times higher field than that of the amplitude of the THz pulses radiated from SI-GaAs PCA when excited at the same pump power of 45 mW, biasing the external fields of 58.3 kV/cm and 25 kV/cm, respectively. The long duration of the THz pulses generated from the antennas can be attributed to the longer duration (~240 fs) of the optical pulses delivered by the pump beam at 522 nm. Indeed, the wavelength of 522 nm corresponds to an electron energy of 2.37 eV. This energy is large enough for electrons to be scattered in the X and L valleys. This is like previous studies when GaAs PCA is pumped to the SHG of the Ti:Sapphire laser at 400 nm. Compared to the waveform of THz pulses generated at 800 nm, the temporal profile of the electric field broadened from asymmetric to symmetric when pumping GaAs PCA at 400 nm [235,236]. Similarly, in our study, it can be assumed that since the PCAs are excited by the optical pulses with a photon energy of 2.37 eV, the hot carriers generated at the top of the valence band will gain sufficiently high energy to disperse into the side valleys. Therefore, the reduced mobility of photoexcited carriers in these adjacent valleys decreases the conductivity, resulting in the broadening of the time duration of the THz pulses radiated from the antennas. Since both waveforms have almost

the same temporal duration, the corresponding spectra have almost the same bandwidth, extending up to 2 THz.

5.1.4 Study of THz radiation properties as a function of the pump power

This section presents the fluence dependence of the peak THz electric field from CdTe and SI-GaAs PCAs. Since the emitted THz pulses from the PCAs are very weak, it is difficult to accurately measure their intensity using infrared or pyroelectric sensors. Therefore, THz radiation amplitude scales in this study are given in arbitrary units. Figure 5-5 (a) shows the peak-to-peak THz field dependence on the optical pump power. To plot the peak-to-peak THz electric field dependence on the pump power in Figures 5-5 (a) and (b), the experimental data were fitted using the hyperbolic fitting, which follows the equation [122].

$$E_{THz} \propto \frac{F/F_0}{1 + F/F_0} \tag{4.1}$$

where F/F_0 is the normalized optical fluence. Figure 4-6 (a) shows the peak-to-peak THz electric field dependence on the pump power when both SI-GaAs and CdTe antennas are operated at the same external bias field of 11.7 kV/cm. The peak fields of the radiated THz pulses from SI-GaAs PCA are about 2.8 times higher than the peak field of the THz pulses radiated from the CdTe PCA when pumped at the highest pump power of 75 mW. However, as can be seen in Figure 5-5 (b), when the external bias field applied to the CdTe PCA is increased to the highest value of 58.3 kV/cm, the radiated THz pulses are shown to be 1.52 times higher than the peak

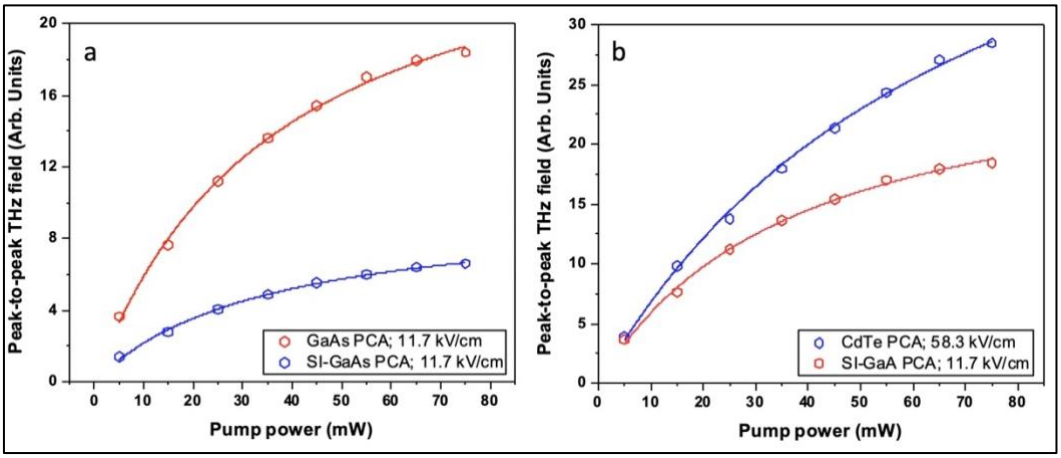

Figure 5-5 Peak-to-peak THz fields versus pump power
a) the scaling of the peak THz field versus from the CdTe and SI-GaAs PCAs when biased at the fixed external field of 11.7kV/cm; (b) the scaling of the peak field from CdTe and SI-GaAs PCAs when biased at and 58.3 kV/cm and 11.7 kV/cm, respectively

field of the THz pulses radiated from the GaAs PCA biased at 11.7 kV/cm. The higher peak field strength of the radiated THz pulses from the GaAs PCA compared to the CdTe PCA at the same bias field of 11.7 kV/cm can be attributed to the higher mobility of over 4890 cm^2/Vs of the former, compared to the mobility of CdTe (~1100 cm^2/Vcm). Indeed, higher carrier mobility will result in a higher photocurrent density leading to an improvement in the maximum conversion efficiency of PCA while improving its surface conductivity.

5.1.5 Study of the THz radiation performance as a function of external bias field

The peak-to-peak THz field amplitudes as a function of the external bias fields applied to the photoconductive antennas are shown in Figure 5-6 (a). Both SI-GaAs and CdTe PCAs were operated under the external bias fields ranging from 1.66 to 25 kV/cm, and 1.66 to 61 kV/cm, respectively, and excited at the same pump power of 28 mW at 522 nm. For bias fields from 1.66 to 25 kV/cm, the SI-GaAs PCA showed a much faster increase in the peak-to-peak THz field with an increasing bias field compared to CdTe PCAs. As a result, the peak field amplitude of the radiated THz pulses from SI-GaAs PCA was 1.32 times higher than that from CdTe-PCA for a bias field of 25 kV/cm. This higher efficiency in the field strength of the radiated THz pulses can be attributed to the relatively higher carrier mobility of SI-GaAs. However, the external bias field applied to the GaAs PCA electrodes is limited due to corona discharge and antenna overheating, which led to antenna destruction. On the other hand, the higher dark resistivity of the CdTe antennas allowed the applied bias field to be increased to 61 kV/cm across the antenna electrodes without observing corona discharge. Therefore, at this higher external bias field of 61 kV/cm, the

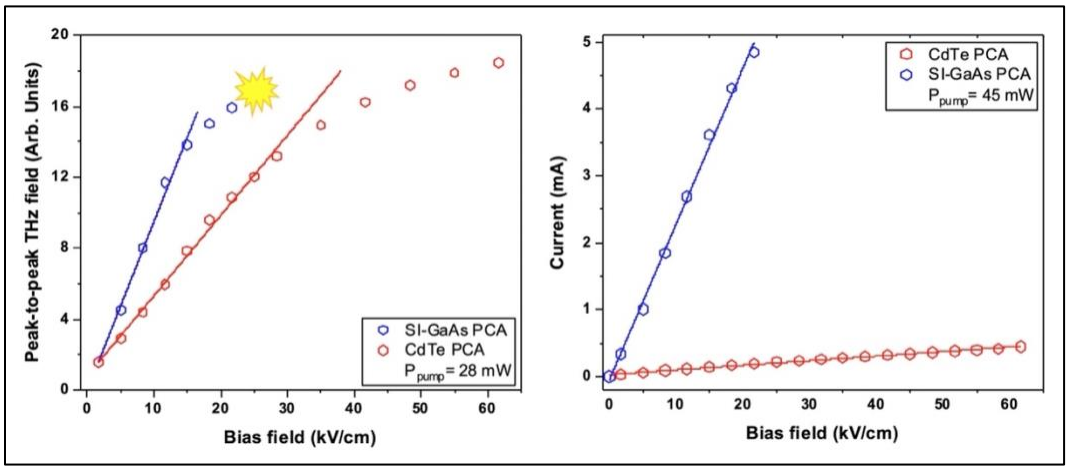

Figure 5-6 Peak to peak THz electric field as function of bias field

(a) The peak-to-peak THz electric field versus bias field from the SI-GaAs and CdTe PCAs at a fixed pump power of 28mW (b) Respective photocurrent as a function on bias fields when both antennas pumped at the fixe pump power of 45 mW

peak field strength of the THz pulses from the CdTe PCA achieved up to 1.17 times higher efficiency than that of the peak field strength of the radiated THz pulses from the SI-GaAs PCA when driven at the maximum bias field of 25 kV/cm. Indeed, as we can see in Figure 5-6 (b), the higher dark resistivity (~10^{10} Ωcm) of CdTe reduced the heating of CdTe PCAs by lower dark current, compared to the relatively low dark resistivity (10^{6}-10^{8} Ωcm) SI-GaAs substrates. As a result, antenna overheating at relatively low bias fields led to the breakdown of the SI-GaAs PCAs. It should also be mentioned that for relatively low bias fields applied to the electrodes, both antennas showed typical linear behavior in the increase of peak-to-peak THz fields. However, when the applied bias fields are increased to higher than 15 kV/cm and 28.3 kV/cm for the SI-GaAs and CdTe PCAs, respectively, the scaling of the peak-to-peak THz fields becomes saturated. This can be mainly attributed to Joule heating in the devices due to increased current densities. This was previously observed from the SI-GaAs PCAs when pumped by Ti:Sapphire laser pulses at 800 nm [237,238].

CHAPTER 6 TERAHERTZ RADIATION ENHANCEMENT OF PHOTOCONDUCTIVE EMITTERS VIA NANODECORATION OF THEIR SURFACE BY PULSED-LASER-DEPOSITED GOLD NANOPARTICLES

6.1 EXPERIMENTAL SECTION

This chapter summarizes our systematic studies on the THz radiation enhancement of PCAs decorated with nanoparticles (NPs) loaded by the pulsed laser deposition (PLD) method. To this end, H-shaped dipole micro-structured PCAs fabricated on SI-GaAs PCAs were decorated with various concentrations of NP, and their radiation performance was compared to the performance of non-decorated antennas. As a first step, we will present a systematic study on the free-space THz generation from the SI-GaAs PCAs decorated with various concentrations of metallic gold nanoparticles (Au-NPs). The peak-to-peak amplitude of the radiated THz pulses from the PCAs with various concentrations of Au-NPs corresponding to the number of laser ablation pulses such as N_{LP}=500, 1000, 1250, and 1500 will be compared to the peak THz amplitude of the radiated THz pulses from the PCAs fabricated on bare SI-GaAs substrate (N_{LP}=0). The advantages and limitations of the metallic NP particles for decorating PCAs will also be briefly discussed. Then, considering the limitations in metallic-NP decorated PCAs, we will present our preliminary work on semiconductor lead sulfide (PbS) nanoparticle-decorated PCAs. The PLD method proposed for the nanodecoration in this work allows a direct deposition of high-quality metallic and semiconductor NPs on the active area of the PCAs. This straightforward technique opens the door to a simple and relatively low-cost method to improve the efficiency of micro-antennas for pulsed THz emission and detection. In addition, the capacity to deposit a high volume of small NPs on a large surface (up to 6 inches) using PLD could be a promising solution for the development of large-aperture photoconductive antennas.

6.1.1 Antenna design and the experimental setup for the generation and detection of THz pulses

The antenna design and experimental setup presented in this study are almost identical to those presented in the previous chapter. Figure 6-1(a) and (b) show the top view photographs of two of the micro-PCAs fabricated on a SI-GaAs substrate. The structure is an H-dipole with a

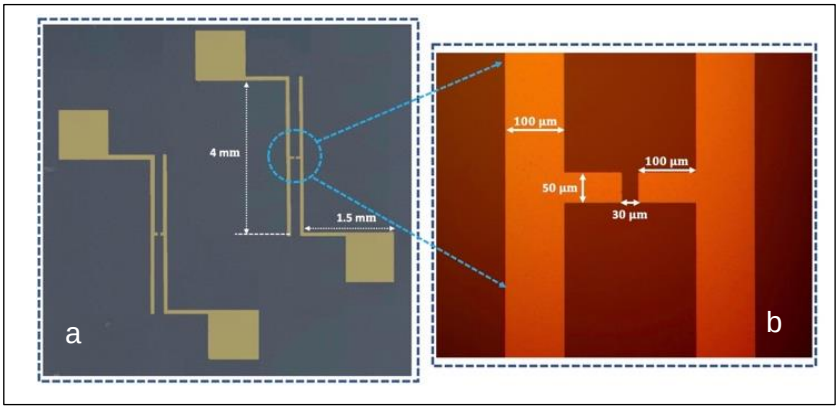

Figure 6-1 Photo of the structure of two micro-dipole PCAs fabricated on 1x1 cm wafer and (b) optical microscope top-view of the micro-fabricated SI-GaAs PCAs

gap of 30 µm and a width of 100 µm. The electrodes were 4 mm long, with on each end a pad of 1mm^2 for wire bonding the antenna. The substrate is a commercial SI-GaAs polished on both sides, with 500 µm thickness and (100) crystallographic orientation. We used a standard photolithography technique using a maskless lithography system (Heidelberg DWL-66 FS). Finally, 5 nm chromium (Cr) and 80 nm gold (Au) layers were deposited on the substrate using the standard electron beam evaporation technique.

The experimental setup for the generation and the detection of free-space THz pulses is identical to the design of the setup we used in Figure 5-2. The PCAs were illuminated using the second harmonic (SH) of a Yb-doped oscillator laser (HighQ-2, Spectra-Physics) operating at a central wavelength of 1045 nm with a pulse duration and repetition rate of 240 fs at 63 MHz, respectively. In this experiment, we used 620 mW of the driving laser at 1045 nm, which was first split into two beams using a UV-fused silica plate beam splitter, 70% of which is focused on a 3.7-mm-thick lithium triborate (LBO) crystal (EKSMA Optics) to obtain the SH at 522 nm, and the remaining 30% of the laser beam at the fundamental wavelength is used to probe the THz pulses. The fundamental wavelength in the SH beam was filtered out using a colored bandpass filter (FGB37-A, Thorlabs, USA). The maximum optical power at 522 nm before the antenna was 75 mW. Using a lens with a focal length of 50 mm, the optical beam was focused onto the gap of the PCA. The free space THz radiation was collected and refocused by two pairs of 2-inch diameter off-axis parabolic mirrors onto the electro-optic detector, which uses a 1-mm-thick CdTe detector crystal with (110) orientation. The THz electric field is measured using balanced photodetectors via conventional EO sampling using the 1045 nm laser beam as a probe and the CdTe EO crystal [95].

6.1.2 PLD-based nanodecoration of GaAs PCAs by Au -NPs

The nanodecoration of the GaAs-based PCA surface (shown in Figure. 6.1(a)) using Au-NP was achieved by the PLD technique under a controlled He background gas pressure [78–80]. First, the GaAs-PCA samples were cleaned and dried by the nitrogen gas jet. Before depositing the Au-NP, the chamber is pumped down to a base pressure of 2×10^{-5} Torr. Then, it is filled with 500 mTorr of helium. To perform the Au-NP deposition, a KrF excimer laser (248 nm wavelength, 15 ns pulse duration, 20 Hz repetition rate, and an on-target fluence of ~3.8 J/cm^2) was focused on an incidence angle of 45° on a rotating gold target (2”-diam., 1/8”-thick and 99.99% pure). The Au-target is placed parallel to the substrate holder at a distance of 7.5 cm, and the substrates were kept at room temperature. To ensure a uniform NP decoration over the surface of the 3”-diameter substrate-holder, the latter is rotated (at ~7 rpm) while the laser beam is continuously swept across the target surface. The PLD of Au-NPs was performed simultaneously onto GaAs-PCAs, silicon, and quartz substrates. While the GaAs-PCAs are intended for the THz experiments, the Si and quartz substrates were used to characterize the morphology of the NP (by means of field-emission-gun scanning electron microscopy (SEM)) and to measure their optical absorption spectra (via UV-Visible spectroscopy), respectively. To control the size of the Au-NP and their density on the GaAs surface (*i.e.,* the surface loading), the number of laser ablation pulses (N_{LP}) for PLD was varied from 500 to 3000. The Au-NPs are thus deposited over the entire GaAs antenna surface, including the 30 μm wide gap of the PCAs. We have studied the THz radiation performance of PCAs with N_{LP} = 500, 1000, 1250, and 1500. We note that when the PCAs are loaded with Au-NP at N_{LP} > 1500, the concentration of gold NP was so high that it created short circuits between the electrodes. Consequently, these antennas were not able to generate any THz radiation. In addition, all the PCAs were tested before and after NP deposition, and their performances were compared.

6.2 RESULTS AND DISCUSSION

6.2.1 Study of the THz signal amplification by Au-NPs nanodecoration

Figure 6.2 (a) shows the temporal trace of the THz electric field and (b) their respective THz spectra generated by a naked PCA and a decorated NP antenna with a concentration of N_{LP} = 1250. For this experiment, the bias voltage and the optical powers were 50 V and 45 mW, respectively. Both waveforms are of a single-cycle nature with a positive peak followed by a

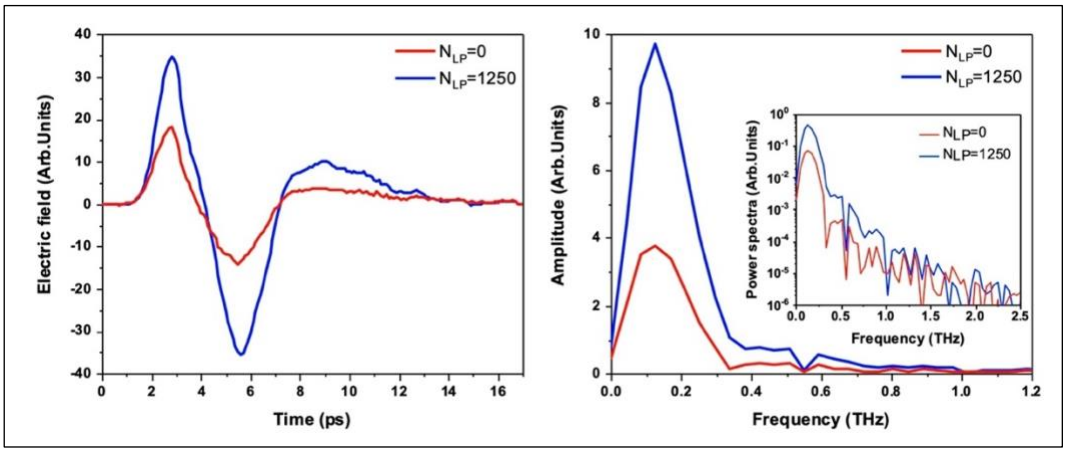

Figure 6-2 THz waveforms and (b) associated THz spectra generated by the SI-GaAs PCA when excited by 45 mW pump power at the external bias field of 16.6 kV/cm before and after decorating with Au-NPs at the N_{LP}=1250. The inset in Figure 5-2 (b) shows the power spectra of the respective THz pulses

negative peak with almost the same amplitude. The amplitude of the THz field for the antenna with NP decoration is more than 2 times higher than the one without decoration. Figure 6-3 shows the THz peak-to-peak electric field as a function of (a) the optical power and (b) the bias electric field for the N_{LP} = 0 and N_{LP} = 1250 antenna. After the decoration process, the peak field of the radiated THz pulses shows an amplification of higher than 2.06 times when the antenna is excited by a maximum pump power of 55 mW at an external bias field of 15 kV/cm, compared with a non-decorated antenna. The scaling of the THz peak field as a function of the bias voltage is linear. On the contrary, the scaling of the THz peak field as a function of optical power is hyperbolic in both cases. However, we find that the saturation regime of the THz peak field as a function of the optical power appears faster when the PCAs are pumped at 50 mW. This saturation behavior is in good agreement with the theory of peak THz electric field saturation versus optical fluence, which can be attributed to the increase in the density of injected photocarriers from the valence band to the conduction band with the increase of the driving laser power. Therefore, the higher carrier mobility of 6400 cm^2/Vs in SI-GaAs will lead to THz field saturation with higher injected optical energy.

On the other hand, the dependence of the peak-to-peak THz amplitude on the bias field follows a typical linear characteristic when the pump laser power is kept constant at 45 mW. Compared to the peak-to-peak field of the radiated THz pulses before decoration at N_{LP} = 0, a 2.24 times higher efficiency of the radiated THz pulses was obtained when N_{LP} = 1250 nano-decorated antenna was biased at a bias field of 16.6 kV/cm. We note that we were not able to apply a bias field higher than 50 V or optical pump power higher than 55 mW. Indeed, above this

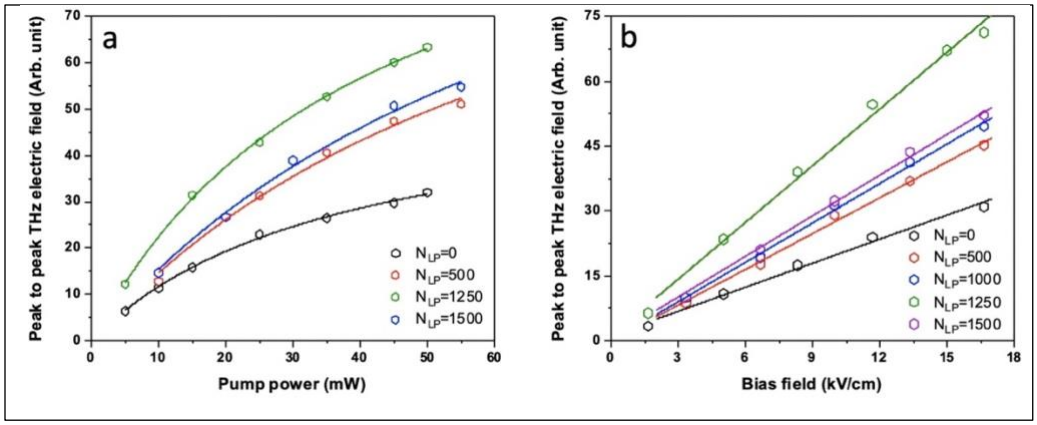

Figure 6-3 Peak-to-peak THz electric fields versus (a) pump power, (b) external bias field Variation of the generated THz signal amplitude with both (a) incident laser pump power when bias voltage is fixed to be 50V and as a function of the applied bias field (b) when the optical pump power is fixed to be 45 mW for various N_{LP}

value, all the antennas, with or without decoration, showed failure due to thermal runaway. It is well-known that most of the failures for the THz antenna are due to thermal issues, like the previous studies performed on the nanodecorated PCAs [239]. It should be noted that the Au-NP can also lead to decreased breakdown voltage between the PCA electrodes due to increased polarization fields between the NPs and the electrodes. However, in our work, the measured breakdown field for all antennas decorated with Au-NP was about 23.3 kV/cm, which is almost identical to the breakdown fields of antennas fabricated on bare substrates.

Figure 6-4 shows the ratio of the THz peak-to-peak field between the decorated antenna (N_{LP} = 500, 1000, 1250, and 1500) and the bare antenna (N_{LP} = 0) when the antennas are pumped with 45 mW and biased at 50 V. We note that this measurement has been done several times and we average the results. Further, the error bar has been calculated by using the peak-to-peak THz electric field values taken from two different antennas corresponding to each N_{LP} value. From Figure 6-4, we can clearly see that the enhancement ratio strongly depends on the NP concentration on the antenna. Between N_{LP} = 0 and N_{LP} = 500, we have ~50% enhancement, but then the enhancement between N_{LP} = 500 and 1000 is only 10%. More surprisingly, the enhancement factor between N_{LP} = 1000 and N_{LP} = 1250 is 41 %, which then decreases between N_{LP} = 1250 and N_{LP} = 1500 by 37%. This curve shows that the enhancement of the radiated peak field is strongly nonlinear.

To better understand the formation of Au-NPs, we performed the SEM and UV-Vis spectroscopy studies of the nanodecorated substrates with various N_{LP} depositions increasing up to 1500. Since the GaAs substrates have higher absorption losses at the UV-Vis ranges, we used silicon substrates for these studies. Figure 6-5(a) shows typical SEM images of the Au-NPs

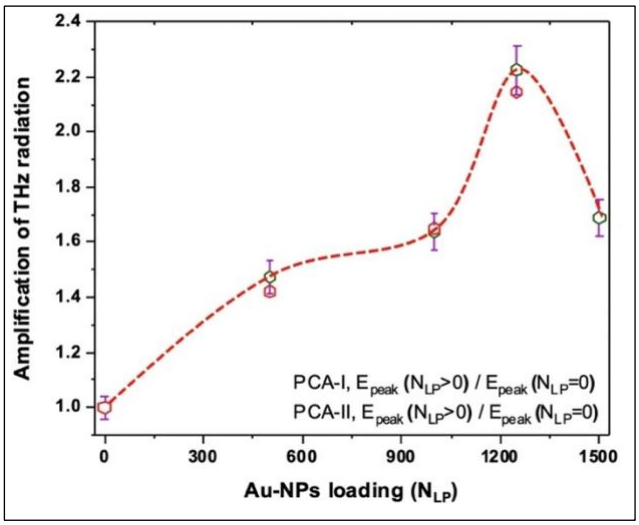

Figure 6-4 NLP dependence of the THz signal amplification by Au-NPs nanodecoration. The dashed-line is used just as a guide-eye.

deposited on silicon substrates for N_{LP} values increasing from 500 to 1500. At N_{LP} = 500, while isolated Au-NPs can be seen (yellow dashed circles), many of them are already seen to coalesce with their neighbors and form some sort of elongated "bean-like" nanoparticles. As the N_{LP} is increased, this "elongated"-coarsening of the NPs via their coalescence continues to take place, leading to a sort of Au-NP discontinuous film. These Au-NP films consist of a network of connected Au-NPs, which can be, at places, separated from each other by a few nm wide gaps (dark channels in Figure 6-5(a)). Consistently, the width and total length of these channels (red arrows) diminish with N_{LP} as the surface loading by Au-NPs is increased. From several SEM images, for each N_{LP} condition, we have estimated the average size of the Au-NPs (yellow dashed circles in Figure. 6-5(a)), along with the corresponding equivalent thickness of the Au-NPs' film. Figure 6-5(b) shows that the average size of the Au-NPs increases from ~10 nm at N_{LP} = 500 to ~15 nm at N_{LP} = 1250, and then remains unchanged for higher N_{LP} values. This NPs' size saturation is thought to result from the on-surface coarsening of the NPs (with increasing N_{LP}), which reaches its maximum when the surface is fully covered by Au-NPs. This size limit is seen to be reached around N_{LP} = 1250. On the other hand, Figure. 6-5 (b) shows that the thickness of the Au-NPs linearly increases with N_{LP}. At N_{LP} = 1250, the equivalent film thickness is ~11nm, while the NP size is ~15 nm. This indicates that the surface is not completely covered by Au-NPs (there is still some uncovered surface, as seen in the SEM images of Figure 6-5 (a); red arrows). Conversely, at N_{LP} = 2000, the thickness of the film is ~25 nm, while the average lateral size of the NPs is ~16 nm. That indicates that once the maximum lateral size of the NPs is reached, they can only grow vertically (out-of-plane) and make thicker films.

The optical properties of the Au-NP films (deposited on quartz substrates) were characterized by measuring their UV-Vis transmittance and reflectance. Figure 6-6(a) and 6-6(b) show the absorption coefficient and optical reflectance of the Au-NP films for different N_{LP} values. The optical absorption of the Au-NP films at 522 nm wavelength is seen to decrease from ~5.6×10^5 cm^{-1} to ~3.8×10^5 cm^{-1} when N_{LP} is increased from 750 to 1500 and then remains almost constant at around (3.7±0.2) $\times10^5$ cm^{-1} for higher N_{LP} values. This can also be translated into the absorption depth of the Au-NP films at 522 nm, as shown in the inset of Figure 6-6(a). Indeed, the absorption depth increases linearly with N_{LP} until it reaches ~28 nm for $N_{LP} \geq 1500$. On the other hand, one can also see in the inset of Figure 6-6 (a) that the reflectance of the Au-NP films at 522 nm linearly increases from ~20% to ~30% when N_{LP} is raised from 750 to 2000. For instance, at N_{LP} = 1250, the absorption depth thickness of the Au-NPs at 522 nm is ~24 nm, thereby exceeding the film thickness of Au-NPs (~11 nm). At N_{LP} = 2000, the absorption depth is slightly larger (~26 nm), but the reflectance is much higher (30% versus 23.5%). This suggests that optimal light absorption would occur for the best trade-off between the largest absorption depth possible and the lowest optical reflectance. Based on the inset of Figure 6-6 (a), at an incident wavelength of 522 nm, such an optimal condition is expected to occur for N_{LP}= 1250 or 1500.

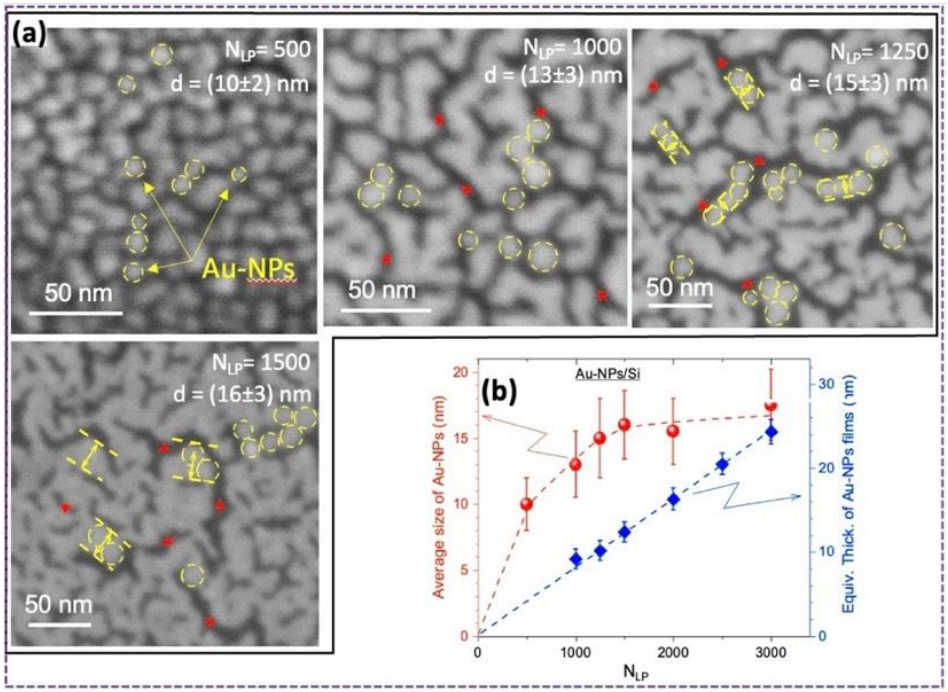

Figure 6-5 (a) SEM images of the Au-NPs deposited on Si substrates at different NLP values; (b) NLP dependence of both the average size of Au-NPs and their associated equivalent film thickness

In our study, since Au-NPs are randomly deposited on the antenna substrates rather than in periodic arrangement, we can assume that these randomly deposited NPs highly localize the pump beam's electric fields with minimal energy dissipation. Therefore, the strong near-field energy distribution in the vicinity of the Au-NP transfers the laser radiation into the host substrate. Since the size, shape, and spacing between deposited NPs are crucial factors influencing the absorption of light by LSPR (localized surface plasmon resonance), it is essential to determine these parameters according to the wavelength of the laser excitation. Indeed, depending on the density, size, and shape of the NP deposited on semiconductor surfaces, the LSPR peak absorption wavelength can be tuned. When the distance between nanoparticles varies according to the dimension of the particles, the peak absorption position of the LSPR is shifted by longer or shorter wavelengths due to the near-field coupling of electromagnetic fields between neighboring particles. Therefore, the increased density of NP in a unit of surface leads to the efficiency of the absorption via localized surface plasmon [240]. As illustrated in Figure 6-5 (b), the average size of Au-NPs varies between 10 and 15 nm, which is proportional to the generated N_{LP} values ranging from 500 to 1250, the average particle size remains almost constant at 17 nm for higher values up to N_{LP} = 3000. In addition, as previously reported [241], the peak LSPR absorption shifts from 516 to 524 nm, whereas the size of the spherical Au-NPs enlarged from 10 to 15 nm. However, since peak LSPR is very close for the Au-NPs in the range of 10-15 nm, and we are not able to individually examine every NPs deposited on the GaAs substrates, it is difficult to accurately estimate the peak LSPR value for various N_{LP}. However, as illustrated in Figure 6-6(a), the decorated substrates at N_{LP} = 1250 have shown a higher absorption depth at 522 nm, compared to relatively lower N_{LP} decorations. Therefore, we can assume these sufficiently large depths allow for the generation of higher photo-induced charge carriers that will participate in the effective generation of THz radiation. On the other hand, although the absorption depths at N_{LP} = 1500 are higher than at that of N_{LP} = 1250, we observed a lower amplification in the THz radiation from the decorated PCAs at high N_{LP} values. This can be attributed to the higher reflectivity of these PCAs due to the increased density of surface-decorated Au-NPs, which could impact their absorption capacity. In addition, when the N_{LP} increases, the interparticle distance becomes smaller. Therefore, the boundary condition of the electromagnetic field confinement in the near field will reduce the light scattering toward the host substrates [242,243]. As a result, reduced absorption from the host substrates with higher N_{LP} decorations results in a reduction in the generated photo carriers. Furthermore, as illustrated in the previous theoretical studies, the

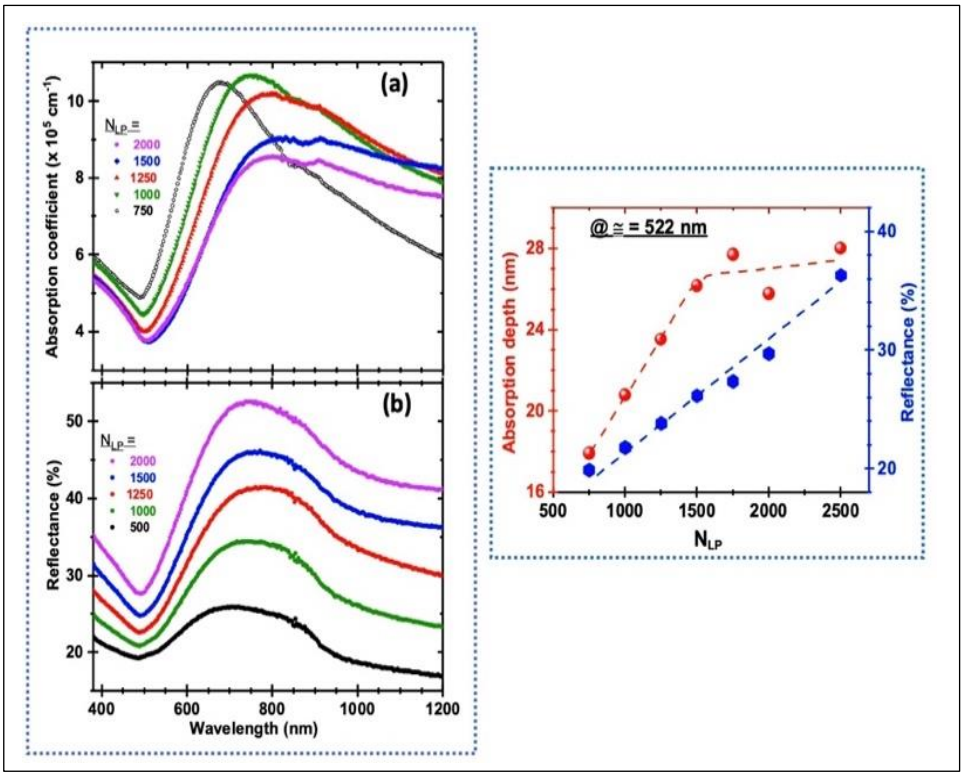

Figure 6-6 UV-Vis spectroscopy graphs of nanodecorated quartz substrates

Optical absorption coefficient of the Au-NPs films deposited at different NLP values on quartz substrates; (b) reflectance spectra of the Au-NPs films as a function of their NLP deposition condition. The inset of figure (a) shows the NLP dependence of both absorption depth and reflectance at the 522 nm wavelength

reduction of inter-particle space (a few nm) leads to a strong increase in temperature during irradiation by the laser light source, and Au-NPs tend to change their shape under pump laser illumination [244]. This nonlinear optical and thermal change can potentially influence the overall plasmonic behavior of the decorated substrates. It can be assumed that the subsequent change in plasmonic behavior could also be a factor in influencing the absorption and extinction cross-section of Au-NP decorated substrates with high N_{LP} values [245]. Finally, our experimental observations indicate that the Au-NPs decorated PCAs exhibit higher thermal stability than their non-decorated counterparts. Since the excessive heating of substrates under high pump powers is one of the main drawbacks of conventional PCAs, which often leads to their thermal breakdown, the use of metal NPs was found to not only enhance the emitted THz field but also improve their thermal stability, contributing thereby to overcome the thermal associated drawbacks. Indeed, Figure 6-7 shows typical I-V characteristics of both non-decorated (N_{LP}=0) and decorated PCAs (at N_{LP}=1000 and N_{LP}=1250). For a constant laser pump power of 45 mW, the photocurrent is seen to increase linearly with the applied voltage. More interestingly, for a given applied voltage of 50V (or a bias field of 16.7 kV/cm), the photocurrent carried by the decorated PCAs (at

N_{LP}=1250, for instance) is 1.5 times higher than for the non-decorated ones (~3 versus 2 mA, respectively). Moreover, when the voltage is increased beyond 50V, the photocurrent of the non-decorated PCAs starts to show more fluctuations (larger error bars), and ultimately breakdown at an applied voltage of 65V (or a breakdown field of 21.6 kV/cm). At such breakdown bias, the PCA is destroyed with apparent material melting (as shown in the inserted image of Figure 6-7). In fact, it is known that generating high photocurrent through the PCA gap leads to the heating of the underlying GaAs substrate and ultimately to its thermal breakdown. Conversely, the NP-decorated PCAs (at the optimal condition of N_{LP}=1250) were found to withstand biasing voltages as high as 70V with much smaller fluctuations in the photocurrent. The apparent electrical resistance (that can be derived from the I-V curves of Fig. 7) of the NP-decorated PCA devices is seen to be significantly lower than that of undecorated ones. Thus, the Joule effect-induced heating is reduced when the PCAs are PLD-decorated with Au-NPs (N_{LP}=1000 and 1250). The presence of gold hexagonal nanostructures within the gap of THz photoconductive antennas has been reported to improve their resistance to thermal breakdown. The enhanced resistance to thermal breakdown of our PCAs decorated with Au-NPs is believed to be due to the improvement of the overall thermal conductivity of the NPs/PCAs hybrid devices. Indeed, the thermal conductivity of gold (3.14 W/cm×K for the bulk, even if a lesser conductivity is expected for discontinuous Au-NPs thin films) is several times higher than that of GaAs substrates (0.55 W/cm×K) [246].

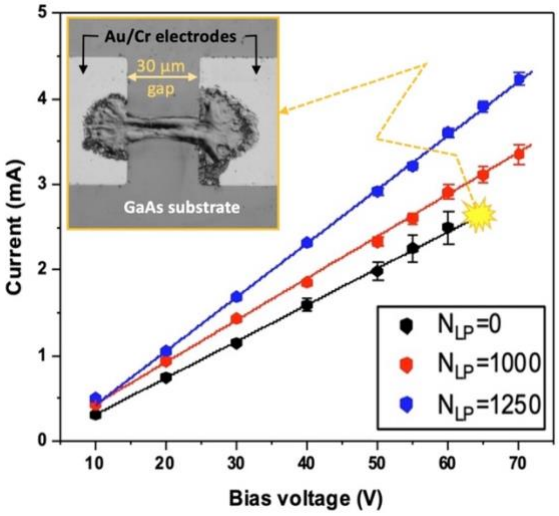

Figure 6-7 Typical I-V characteristics of non-decorated (black curve) and decorated PCAs at NLP=1000, and 1250 (red and blue curves, respectively) when pumped at 45 mW. The errors bars reflect the fluctuations between minimum and maximum photocurrent values at a given applied bias voltage. The inset shows an optical microscopy image of a non-decorated (N_{LP}=0) antenna after its breakdown.

However, apart from these aforementioned advantages, Au-NP deposited PCAs have shown a critical drawback of short circuits when the antennas are overloaded with metal nanoparticles, which leads to an excessive drop in dark resistivity across the antenna electrodes, limiting the external bias field applied. Indeed, our experiments have indicated that when the Au-NP density is increased to over N_{LP}=1500 on the surface of the SI-GaAs PCAs, the resistivity decreases sharply to a few 10s of Ω, which limits the applicable external bias field. To this end,

we propose to replace the metal NPs on the PCA's active excitation area with semiconductor NPs, which could be a promising solution to overcome this limitation.

6.3 GaAs-PCAs DECORATED WITH LEAD SULFIDE NPs

6.3.1 Results and discussion

This section briefly summarises our preliminary studies on the SI-GaAs PCAs deposited with PbS-NPs. We believe that the decoration of PCAs with these semiconductor NPs will improve their THz radiation efficiency compared to metallic NPs deposited antennas by increasing the applied external bias field due to the significant enhancement in the limitation of the short-circuit current. Having a direct band gap of 0.41 eV and a shorter carrier lifetime, ranging between 10's of ps to several ns, PbS-NPs could be an alternative material for decorating PCAs [247]. Among other semiconductors-NPs, the deposition of narrow bandgap PbS-NPs on SI-GaAs PCAs will

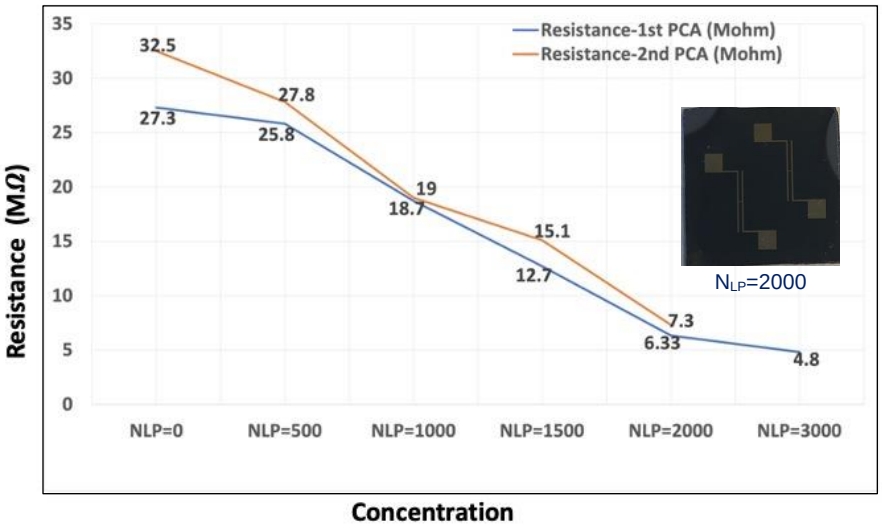

Figure 6-8 Concentration dependent resistance of PbS-NPs decorated GaAs PCAs with various NLPs
Orange and blue curves describe the measured resistances from the 1st and 2nd PCAs on the same substrates without laser illumination. Inset shows the top view of a PCA decorated with PbS-NPs with N_{LP}=2000

allow them to be excited with a relatively higher photon energy of the pump beam at 522 nm. In addition, typical UV-NIR spectroscopy of PbS NPs deposited on quartz substrates using PLD shows that with increasing density of N_{LP} from 500 to 5000, these NPs showed a high absorption behavior in the Vis-NIR region [248]. Therefore, we present our early studies on the SI-GaAs PCAs decorated with PbS NPs.

Figure 6-7 depicts the measured resistance of GaAs PCAs decorated with PbS NPs, without laser illumination. When the concentration of deposited PbS-NPs in the active excitation area is increased from N_{LP}=0 to 3000, the antenna resistance decreases from 27.3 to 4.3 MΩ. To study the THz radiation performance of PbS-NP decorated antennas, we used the same

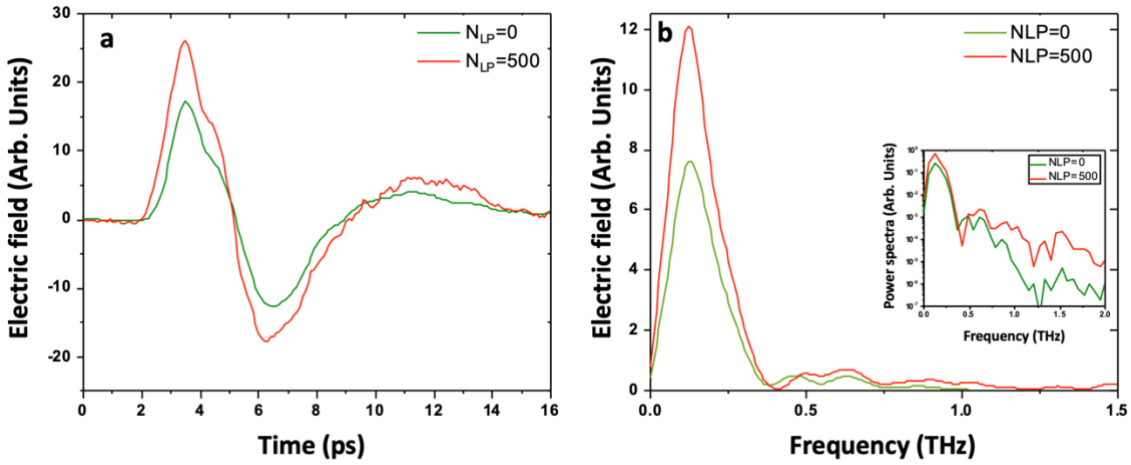

Figure 6-9 (a) Waveforms and (b) respective spectra of the THz pulses radiated from SI-GaAs PCA before and after deposition of PbS-NPs with NLP=500 The inset in the figure (b) shows the power spectra of emitted THz pulses before and after decoration

experimental setup described in Figure 6-2. Under the same optimum condition, an H-dipole Si-GaAs PCA with a gap, width, and length of 30 μm,100 μm, and 4 mm, respectively was studied before and after N_{LP}=500 decoration. The antenna was biased at a 15 kV/cm external field by illuminating 35 mW pump power at 522 nm. Since the results obtained with other higher N_{LP} values require more additional experiments to be confirmed, we present only our results obtained from PCAs decorated with PbS-NPs at N_{LP}=500.

Figure 6-8 shows the waveforms and respective amplitude spectra of the PbS-NP decorated SI-GaAs PCA before and after the N_{LP}=500 decoration. As can be seen in Figure 6-8(a), the THz pulses radiated from the SI-GaAs PCA have almost the same asymmetric bipolar waveforms before and after decoration with PbS-NPs. The peak field strength of the THz pulses radiated from the antenna after the decoration of PbS-NPs with NLP=500 has an efficiency almost 1.52 times higher than that of the peak field strength of the THz pulses radiated before the decoration. The Fourier transform shows that with the spectral peak located at about 120 GHz, both THz waveforms of the radiated signal before and after decoration have almost the same frequency spectrum extending to over 1 THz (Figure 6-8 (b)).

Peak-to-peak THz field strength dependence on the external bias fields shows that the radiated THz pulses from the emitter before and after N_{LP}=500 decoration have linear behavior when excited at a fixed pump power of 45 mW by increasing the bias field from 0 to 17 kV/cm (Figure 6-9(a)). The peak THz amplitude as a function of the 522 nm pump power shows typical peak-to-peak scaling behavior for both cases when the antenna is biased at a fixed DC field of 15 kV/cm (Figure 6-9). The results show that linear dependencies are only found at low pump powers and that the THz radiation power saturates at higher pump powers.

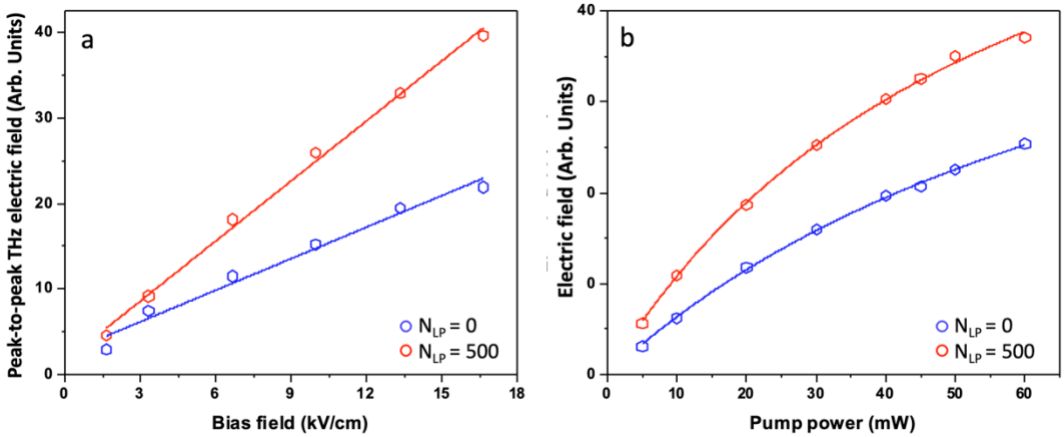

Figure 6-10 (a) Peak to peak electric field dependence on the external bias field, and (b) the excitation pump beam power from SI-GaAs PCAs before and after decoration of NLP=500

These preliminary studies have shown that PbS-NPs have the potential to increase the radiation performance of PCAs. However, detailed studies are needed to determine the efficiency of the radiated THz pulses for higher concentrations of PbS-NPs.

CHAPTER 7 CONCLUSION AND FUTURE WORK

In this thesis, we presented the results of our investigations on various THz sources driven by femtosecond Yb laser pulses and its second harmonic generation (SHG) at 1045 and 522 nm central wavelengths. In addition, two novel approaches are proposed for the development of photoconductive emitters, which provide an important solution for controlling the density of the deposited NPs on the antenna surface, and the polarization states of the radiated THz pulses. To this end, in Chapter 3, we examined a comparative study on the THz radiation performance of two organic BNA and inorganic CdTe crystals by the OR method using optical pulses delivered by a Yb laser at the fundamental wavelength of 1045 nm. Then the novel approach to the generation of high-intensity THz pulses with variable polarization was presented in chapter 4. The experimental results conducted on the generation of high-intensity THz pulses with variable polarization from a ZnSe ILAPCA with specific interdigitated electrodes were presented in this section. Next, the implementation of an early study of the THz radiation performance of CdTe and GaAs PCAs using the SHG of Yb laser at 522 nm was presented in Chapter 5. Subsequently, chapter 6 devotes a systematic study of the THz radiation performance of nanodecorated SI-GaAs PCAs. The early (PLD) method presented in this work for the nanodecoration allowed for adjustment of the THz radiation performance of PCAs by gradually changing the density of the NPs in the active illuminated area. To this end, the radiation performance of GaAs PCAs decorated with different concentrations of metal (Au) and semiconductor (PbS) nanoparticles was compared with the performance of those fabricated on bare GaAs substrates. The simple laser-based nanodecoration PLD method enables to deposit of uniformly sized NPs on large-area substrates, which is a very promising solution for the processing of large-aperture photoconductive emitters. In addition, this simple and relatively low-cost method opens the door to improving the efficiency of micro-structured antennas for pulsed THz emission and detection.

Since the short-circuit current density is one of the main limiting factors in metal NPs decorated PCAs, semiconductor NPs could be an alternative solution to overcome this limitation. Indeed, our experimental studies have shown that when the Au-NPs concentration increases in the photoconductive gap of SI-GaAs emitters corresponding to the N_{LP} values higher than 1500, the variation of the NPs density leads to a strong decrease of the resistivity (from several MΩ to a few 10's Ω), which limits the external bias field applied to the electrodes. Therefore, with a narrow band gap and a shorter carrier lifetime, ranging between 10's of ps to several ns, PbS-NPs could be an alternative solution for decorating PCAs. Our preliminary studies have shown

that when the density of PbS-NPs is gradually increased in the gap of SI-GaAs PCAs from N_{LP}=500 to N_{LP}=3000, the resistivity decreased from 25.8 to 4.8 MΩ due to increased absorption of antennas. Indeed, a direct comparison of the peak field strength shows that radiated THz pulses have almost 1.5 times higher efficiency when decorated with PbS-NPs at NLP=500 compared to bare substrates. However, a detailed study on the performance of PbS-NPs decorated photoconductive antennas and THz radiation efficiency as a function of NP density is needed. In addition, since the size, shape, interparticle spacing, composition of NPs, and refractive index of the particle-semiconductor interface are the main factors influencing surface resonance plasmon absorption, some theoretical studies are needed to define an effective photocarrier generation efficiency for a given laser wavelength. Furthermore, since the laser-based straightforward PLD method can deposit uniformly sized NPs on large-area over 6 inches substrates, it can be used for processing current promising LAPCAs embedded in the wide bandgap semiconductors having superior thermal and electrical properties. From this perspective, nanodecoration of various LAPCAs embedded onto 6H-SiC, 4H-SiC ZnO, and GaN substrates can improve their limited photon absorption performance and boost their potential to be used with the SHG of conventional Ti:Sapphire laser amplifiers at 400 nm. Finally, our preliminary experiments on semi-large gap SI-GaAs PCAs have shown that encapsulation of antenna electrodes with a high-resistivity epoxy layer (Bisphenol-A) improves by more than two times the antenna air breakdown limits. Therefore, encapsulation of nanodecorated LAPCAs with high resistivity anti-reflective epoxy layers could be another solution for the enhancement of the amplitude of the radiated THz pulses.

CHAPTER 8 RÉSUMÉ DE LA THÈSE (FRANÇAIS)

8.1 Introduction générale et motivation de la thèse

Depuis la première démonstration expérimentale dans les années 1980, la science et la technologie térahertz (THz) ont connu de grands progrès. Grâce aux progrès rapides des lasers accordables de haute puissance et de la technologie des détecteurs sensibles, le domaine THz a considérablement progressé au cours des dernières années. Le domaine THz couvre l'ensemble du spectre électromagnétique compris entre les longueurs d'onde de l'infrarouge et des micro-ondes (10 μm- 300 μm), ce qui correspond à une gamme de fréquences variant entre 0.1 et 10 THz. En d'autres termes, la période associée à 1 THz est égale à 1 picoseconde (ps), ce qui correspond à une longueur d'onde de 300 μm, un nombre d'onde de 33 cm^{-1}, une énergie de photon de 4.1 meV, et une température équivalente de 47.6 K [2].

Aujourd'hui, la technologie THz est très exigeante dans une large gamme d'applications, allant des sciences fondamentales telles que la spectroscopie biochimique [249], les matériaux solides [250], l'astronomie [251] et la science des nanomatériaux [49], à des domaines pratiques tels que la science environnementale [252], les produits pharmaceutiques, l'agriculture et la sécurité [1]. Les avantages de l'onde THz incluent sa capacité à transmettre la lumière visible à travers des objets opaques avec une énergie de photon correspondante de 1-100 meV, qui est un spectre de l'énergie important pour divers matériaux et biomolécules. En outre, les ondes THz sont non-destructive et ne risquent pas d'endommager les objets par rapport aux rayons-X. Ces caractéristiques permettent diverses applications d'imagerie et de spectroscopie utilisant les ondes THz et rendent ainsi les mesures THz un outil puissant pour les contrôles non destructifs [7-9]. En outre, comme le rayonnement THz a des longueurs d'onde plus courtes que les micro-ondes, il offre une résolution spatiale plus élevée et une meilleure résolution spectrale des empreintes digitales. Grâce à cette caractéristique spectrale unique, les impulsions THz associées aux énergies de photons inférieures au seuil d'ionisation offre une grande opportunité pour les études des vibrations du réseau, des rotations moléculaires, des ondes de spin, des excitations internes des paires électron-trou et des vibrations des phonons dans les cristaux solides et des états d'hydratation dans les systèmes biologiques [11-13]. Les technologies de l'information et de la communication, l'informatique ultrarapide, la surveillance de l'environnement et l'évaluation non destructive sont d'autres domaines d'application importants du rayonnement THz, en raison de sa nature transitoire, directionnelle et à haute cohérence [14-19]. En outre,

d'autres applications industrielles, agricultures, et biomédicales rendent la technologie THz primordiale pour le contrôle de la qualité et l'imagerie [4,253–256].

Le développement de la plupart des sources de rayonnement THz coïncide avec l'émergence des lasers ultrarapides, notamment le laser Ti:Sapphire, qui a capable de générer des impulsions femtosecondes à une longueur d'onde centrale de ~ 800 nm [257]. Depuis plus de 20 ans, la technologie THz s'est considérablement améliorée grâce à la disponibilité commerciale de ces sources lasers femtosecondes. Depuis lors, il existe nombreuse sources THz pouvant être pilotées par des lasers Ti:Sapphire avec des longueurs d'onde fondamentales et de seconde harmonique [179,237,258,259]. Cependant, récemment, les systèmes laser à fibre Yb avec une longueur d'onde centrale de ~1030 nm sont devenus le principal concurrent des lasers Ti : Sapphire en raison de leurs divers avantages pratiques tels que la simplicité, la compacité, la rentabilité et la facilité de maintenance [260–262]. En outre, des puissances moyennes supérieur avec un taux de répétition flexible pouvant atteindre jusqu'à 10 MHz et la capacité de transfert rapide la chaleur du milieu actif à l'air rendent ces lasers particulièrement attirants par rapport aux lasers Ti : Sapphire traditionnels . Grâce à l'émergence des technologies de disques minces et de fibres optiques, les systèmes laser Yb conventionnels modernes sont capables de générer des impulsions ultrarapides avec une puissance moyenne de l'ordre du kilowatt à la fréquence de répétition de MHz . Par conséquent, les lasers à fibre Yb ont suscité un intérêt considérable dans de nombreuses applications fondamentales et industrielles [40,41,263,264]. La capacité d'atteindre une puissance moyenne élevée avec des taux de répétition relativement élevés rend ces sources particulièrement intéressantes pour les mesures THz en raison de l'amélioration du rapport signal-sur-bruit. Par conséquent, il existe un fort besoin de développer des sources THz efficaces pouvant fonctionner avec les lasers dopés à l'Yb. À cette fin, cette thèse vise à étudier et à développer plusieurs émetteurs THz qui peuvent être exploités par un oscillateur laser à fibre dopée à l'Yb à haut taux de répétition, fonctionnant à des longueurs d'onde SH- et fondamentales de 522 nm et 1045 nm, respectivement.

Les antennes photoconductrices (APCs) sont les dispositifs les plus répandues pour la génération et la détection de THz [48,54]. Grâce à leurs caractéristiques uniques de grande stabilité d'impulsion crête-à-crête, les sources photoconductrices THz présentent une efficacité de conversion optique-THz supérieure, nécessitant une puissance de la pompe optique relativement faible. Comme l'efficacité de conversion optique-THz supérieure des APCs dépend principalement des champs de polarisation externes appliqués plutôt que de la puissance de la fluence de pompe, ces sources peuvent être de meilleurs candidats pour réaliser des systèmes

THz-TDS fonctionnant avec des impulsions optiques à taux de répétition élevé et à puissance de pompe relativement faible générées par des oscillateurs laser ultracompacts. À cette fin, plusieurs antennes photoconductrices à l'échelle micrométrique capables de fonctionner aux longueurs d'onde fondamentales des lasers à fibre d'Ytterbium et d'Erbium ont récemment été proposées [265–267]. Malgré ces progrès impressionnants, la conversion optique-THz de cette antenne reste toujours faible, et il existe un intérêt particulier pour renforcer l'intensité de champ maximale des impulsions THz émises par les APCs pompées par des oscillateurs laser femtoseconde.

L'insertion des nanoélectrodes plasmoniques dans la zone active d'excitation de l'antenne est l'une des solutions avancées pour améliorer l'efficacité de la conversion optique-THz des APCs. Le renforcement de la puissance du rayonnement THz par ces antennes peut être attribuée à l'augmentation considérables des porteurs de charges photo-générés dans la zone active de l'antenne avec la concentration parfaite du faisceau de pompe à proximité des électrodes. Par conséquent, ces antennes photoconductrices sont considérées comme les sources les plus efficaces à ce jour, avec une efficacité de conversion optique-THz pouvant atteindre 7,5 % [115]. Malgré ces performances exceptionnelles, les antennes nanoplasmoniques nécessitent un processus de fabrication très complexe combinant plusieurs étapes utilisant la lithographie par faisceau d'électrons, le dépôt chimique en phase vapeur et la lithographie optique, ce qui rend ces antennes très coûteuses et réduit leur productivité. Par conséquent, il est important de trouver de nouvelles méthodes relativement moins chères visant à améliorer les performances des APCs adaptées aux longueurs d'onde fondamentales et de seconde harmonique des lasers conventionnels.

Le dépôt de nanoparticules (NPs) sur la surface des APCs est l'une des approches prometteuses actuelles pour l'amélioration de l'intensité du rayonnement THz par ces sources. L'augmentation du nombre de porteurs photogénérée dans les substrats photoconducteurs recouverts par des NPs peut être attribuée à l'amélioration locale du champ électrique du faisceau de la pompe femtoseconde à proximité des particules déposées. Par conséquent, les plasmons atteignant des champs proches suffisamment forts arrachent les électrons de valence de leur liaison de valence, ce qui entraîne la génération de paires électron-trou dans les bandes de conduction et de valence du substrat hôte. Ainsi, l'augmentation de la densité des photo-porteurs générés contribue à l'amélioration de l'efficacité du rayonnement THz de l'ACP en raison de la densité de courant accrue. Pour cette fin, récemment l'efficacité du rayonnement THz des APCs GaAs on été étudié en déposant des différentes NPs déposées sur leurs surfaces [69,71,72,268].

L'amplitude des impulsions THz rayonnées par les ACPs nanodécorées a présenté une amplification entre 1,4 et 2 fois par rapport aux antennes GaAs intégrées au substrat nu lorsqu'elles ont fonctionné dans les mêmes conditions optimales à une longueur d'onde de laser de pompe de 800 nm. Bien que ces études préliminaires fournissent une solution importante pour améliorer les performances des ACP conventionnelles, l'efficacité du rayonnement THz a été étudiée de manière aléatoire selon la densité des NPs. De plus, les méthodes précédentes proposées pour la préparation et le dépôt de NPs nécessitent certains traitements thermiques et chimiques. Ces traitements présentent certains inconvénients essentiels tels que la distribution non uniforme et le contrôle de la concentration des NPs déposées, ce qui est très important pour les surfaces de petites dimensions telles que l'espace photoconducteur des ACPs [76,77]. En outre, les méthodes chimiques utilisées pour la nanodecoration nécessitent la précipitation de produits chimiques toxiques sur les substrats et un processus supplémentaire de purification des nanoparticules après le processus de dépôt, ce qui est difficile pour la fabrication à grande échelle, le temps de traitement long et le coût élevé de l'équipement pour le traitement. Nous présentons donc pour la première fois la décoration de nanoparticules d'or (Au-NPs) sur des APCs de GaAs par dépôt par laser pulsé (PLD), qui permet la formation relativement simple et efficace de NPs en utilisant des impulsions laser.

La PLD est une méthode physique très efficace pour la nanodecoration in-situ de toute surface de matériau par des NPs métalliques ou semi-conductrices très pures [80,248,269]. Par rapport aux méthodes chimiques (comme le sol-gel), la technique PLD se distingue par sa capacité à produire des films ou des nanoparticules de grande pureté (sans recourir à des précurseurs chimiques et donc sans contamination résiduelle), une bonne contrôlabilité de la quantité déposée de matériau décoratif. La possibilité de contrôler la taille et la densité de surface des nanoparticules déposées par PLD permet un transfert de composition congruent (CST) de la cible ablatée vers les NPs dans des conditions d'ablation spécifiques, et une meilleure fixation des NPs déposées sur le substrat (en raison de la haute énergie des espèces ablatées impliquées dans le processus d'ablation laser). De plus, cette méthode simple basée sur le laser permet de déposer des NP de taille uniforme sur des substrats de grande surface, ce qui est une solution très importante pour le traitement des APCGOs.

De ce point de vue, cette thèse implique des études préliminaires systématiques de la performance du rayonnement THz par des APCs décorées par des nanoparticules d'or dans la zone active illuminée par un laser femtoseconde Ytterbium. À cette fin, nous avons étudié la performance du rayonnement THz de deux sources de redressement optique dans les mêmes

conditions optimales excitées par le laser dopé à l'Yb à la longueur d'onde fondamentale dans un environnement purgé à l'azote. Cette étude nous a permis d'optimiser notre montage expérimental de THz-TDS, ainsi que développé des sources de redressement optique intégrées au laser Yb à la longueur d'onde centrale à 1045 nm. Ensuite, la fabrication et l'étude des performances du rayonnement THz des sources photoconductrices excitées par le SH du laser femtoseconde dopé à l'Yb ont été présentées. Finalement, les performances du rayonnement THz par les APCs nano décorés seront étudiées en fonction de la densité des NPs d'or dans l'espace photoconducteur en utilisant un laser Yb femtoseconde. La méthode PLD nous a permis de contrôler progressivement la densité des NPs déposées dans la région d'excitation active permettrait de régler les performances d'absorption des photons des émetteurs photoconducteurs à grande ouverture, ce qui permettrait de surmonter l'une des principales limitations actuelles de la génération d'impulsions THz intenses. En outre, une nouvelle méthode pour ajuster les états de polarisation des impulsions THz de haute intensité provenant de l'émetteur photoconducteur à grande ouverture avec une structure interdigitée spécifique sera également présentée.

8.2 RÉSUMÉ

Cette section présente le résumé des études expérimentaux présentées dans cette thèse. En tenant compte des études susmentionnées, cette thèse est organisée comme suit. Le *Chapitre 1* est consacré à l'introduction générale et la frontière du domaine THz. Au *Chapitre 2*, nous avons brièvement présenté les méthodes de génération et de détection des impulsions THz au moyen de lasers femtosecondes compacts. Dans ce chapitre, nous présenterons également nos résultats expérimentaux comparatifs sur le rendement du rayonnement THz par les cristaux de tellurure de cadmium (CdTe) et de N -benzyl-2-méthyl-4-nitroaniline (BNA) réalisés par rectification optique. Ensuite, la théorie de la génération d'ondes THz à partir des APCs est présentée dans *Chapitre 3*. Nous avons passé en revue la théorie de la génération, les progrès récents ainsi que les limites actuelles dans la génération d'ondes THz par les antennes photoconductrices. Nous avons discuté également des antennes photoconductrices à grande ouverture (APCGOs) et des émetteurs photoconducteurs à grande ouverture interdigités, qui sont les principales sources de génération d'ondes THz intenses. Nous avons présenté ensuite nos résultats expérimentaux sur la génération d'impulsions THz sous-cycliques de haute intensité avec une polarisation elliptique variable à partir d'APCGO. Ensuite, le processus de fabrication des APCs de type microdipole par la méthode de photolithographie sans masque, ainsi que

l'étude de leurs performances dans le montage de THz-TDS sont présentés dans *Chapitre 4*. Dans ce but, deux APCs de type dipôle à l'échelles micrométrique fabriquées sur des substrats SI-GaAs et CdTe ont été étudiées sous excitation GSH d'un laser femtoseconde dopé Yb à 522 nm. Le *chapitre 5* présente des détails supplémentaires sur la méthode PLD utilisée pour décorer les PCA avec des NPs, ainsi que la théorie expliquant l'amélioration de l'efficacité du rayonnement THz des antennes décorées avec des Au-NPs. Les résultats expérimentaux de l'efficacité du rayonnement THz des antennes nano-décorées avec différentes densités d'Au-NPs seront également présentés dans ce chapitre. En outre, l'avantage et les études préliminaires réalisées sur les NPs semi-conducteurs tels que le PbS sont démontrés dans ce chapitre. Enfin, *Chapitre 6* est résumé les résultats obtenus au cours de cette recherche, les perspectives et les propositions de nouveaux types de NPs, ainsi que l'intérêt de la nanodecoration des APCGOs par la méthode PLD pour augmenter leurs performances en matière de rayonnement THz.

8.2.1 Étude de la génération d'ondes THz dans des cristaux de CdTe et BNA sous l'excitation d'un laser femtoseconde dopé à l'Yb à des taux de répétition de MHz (Chapitre-2)

Nous présentons notre première étude expérimentale menée sur la génération d'ondes THz par les cristaux de CdTe et BNA utilisant la méthode de redressement optique. Les cristaux de BNA ont été largement utilisés pour la génération d'impulsions THz de haute intensité pompée par des lasers amplifiés avec des taux de répétition de l'ordre de 100 Hz à 1 kHz. Cependant, la performance du cristal BNA et son potentiel pour générer un rayonnement THz à un taux de répétition élevé et une longue durée d'impulsion de la longueur d'onde d'excitation dans la gamme de 1µm était encore inconnu jusqu'à présent. À cette fin, nous avons d'abord étudié le rendement du rayonnement THz par BNA avec différentes épaisseurs du cristal. Ainsi, l'efficacité du rayonnement THz par les cristaux de BNA avec des épaisseurs de 0.63-, 0.81- et 1.09-mm a été démontrée lorsqu'ils sont pompés par un laser Ytterbium avec la longueur d'onde centrale de 1045 nm. Ensuite, les performances du rayonnement THz du cristal BNA le plus efficace est comparées à celles d'un cristal CdTe de 0.8 mm d'épaisseur dans des conditions d'excitation optimales dans un environnement purifié à l'azote. Pour la génération et la détection des impulsions THz, nous avons utilisé dans cette étude un montage THz-TDS conventionnel utilisant un laser oscillateur dopé à l'Yb avec une durée d'impulsion et une fréquence de répétition, respectivement, de 238 fs et 63 MHz (HighQ-2, Spectra-Physics). Comme le montre la Figure 8-1, le faisceau laser principal du laser femtoseconde à 1045 nm, d'une puissance d'entrée de 520

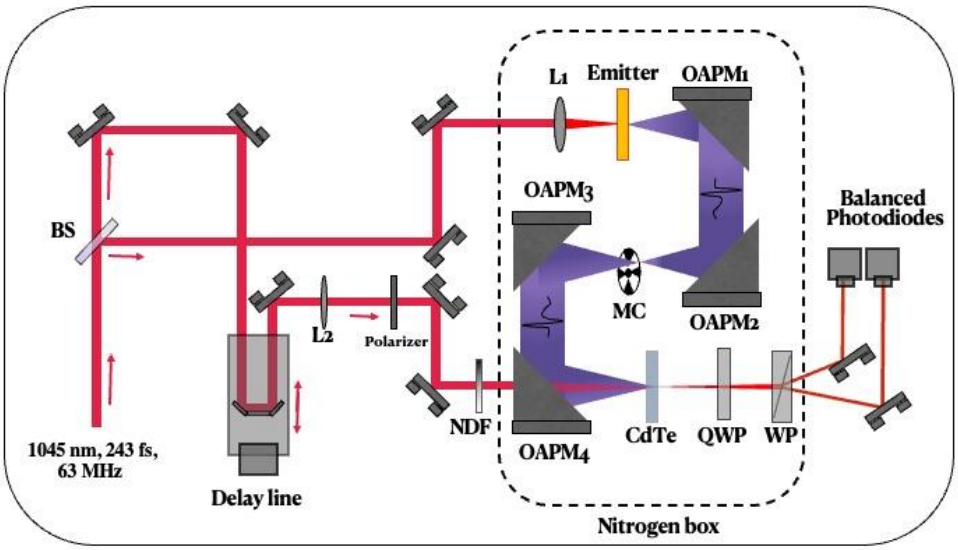

Figure 8-1 Le schéma expérimental de montage utilisé pour la génération d'onde THz par les cristaux de BNA et CdTe par redressement optique

mW, est d'abord divisé en deux parties à l'aide d'un séparateur de faisceau UVFS, et 90 % de la puissance totale est utilisée pour le processus de génération d'ondes THz, les 10 % restants étant utilisés pour sonder les impulsions THz générées. Le faisceau de pompe est ensuite focalisé sur le cristal émetteur par une lentille plan-convexe à une distance focale de 50 mm. Les impulsions THz générées en espace libre par le cristal sont d'abord collectées par une paire de miroirs paraboliques hors axe (OAPM) de 2 pouces, puis guidées par une paire d'OAPM de 3 pouces sur le cristal du détecteur électrooptique (EO). Les impulsions THz sont détectées par un cristal CdTe de 1 mm d'épaisseur, poli sur les deux faces et d'une taille de (5x5mm), en utilisant une technique d'échantillonnage électro-optique (EO) standard. Le rayonnement THz émis a été modulé avec un hacheur mécanique à une fréquence de 230 Hz, et le signal de sortie d'une paire de photodétecteurs est amplifié à l'aide d'un amplificateur à verrouillage (RG-830 de Stanford Research).

Les formes d'onde et les spectres des impulsions THz rayonnées par les cristaux BNA sont illustrés à la Figure 8-2. Pour assurer une comparaison équitable des performances de rayonnement, tous les cristaux ont été étudiés dans les mêmes conditions optimales, lorsqu'ils sont illuminés par un laser de pompe moyenne de 450 mW tout en maintenant la puissance de la sonde constante à 27 mW en contrôlant l'intensité avec un filtre métallique à densité neutre pendant toutes les mesures. Comme nous pouvons le voir sur la Figure 8-2(a), les principales impulsions THz rayonnées par les cristaux de BNA ont la même forme d'onde monocyclique qui est suivie d'une série de petites oscillations s'étendant jusqu'à 8 ps, provenant de l'absorption de

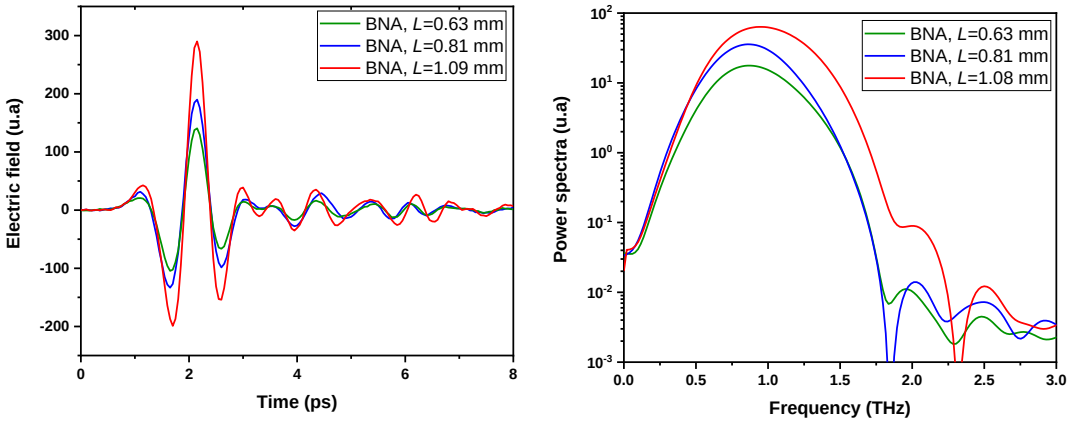

Figure 8-2 (a) Formes d'onde et (b) les spectres respectifs d'impulsions THz émises par les cristaux de BNA

la vapeur d'eau. La durée de l'impulsion principale est de ~640 fs (intensité FWHM). Ainsi, les impulsions THz rayonnées par le BNA de 1.09 mm ont une efficacité 1.5 et 2.1 fois supérieure à celle des cristaux de BNA de 0.81 et 0.63 mm d'épaisseur, respectivement. En outre, les spectres de puissance THz respectifs calculés par transformée de Fourier montrent que la largeur de bande des impulsions THz rayonnées s'élargit avec l'augmentation de l'épaisseur du cristal (Figure 8-2(b)). La largeur de bande supérieur s'étendant supérieur s'étendant de 2.5 THz a été observée pour le cristal d'une épaisseur de 1.09 mm. Cependant, tous les spectres présentent des creux principaux autour de 1.8 THz et 2.3 THz, qui peuvent être attribués aux absorptions de phonons dans le cristal BNA. Ces creux typiques dans les cristaux BNA ont également été observés dans des études précédentes et constituent l'un des principaux facteurs limitant les performances de BNA pour les applications en spectroscopie.

D'autre part, par suite de cette dernière étude comparative, les performances du cristal BNA de 1.09 mm d'épaisseur ont été comparées à celle de l'efficacité du rayonnement THz par un cristal CdTe de 0.80 mm d'épaisseur dans un environnement d'azote purgé. À cette fin, après avoir optimisé les cristaux de l'émetteur et du détecteur, le montage expérimental a été purgé à l'aide d'une chambre sensible à la lumière, et de l'azote ultra sec est injecté sous pression pour éliminer l'humidité et la vapeur d'eau. Ensuite, le rayonnement THz ont été enregistrés dans les conditions optimales avec un taux d'humidité inférieur à 3%. Comme nous pouvons le voir sur la Figure 8-3 (a), la diminution de l'humidité a amélioré de manière significative le rapport signal/bruit, et une amélioration de plus de deux fois de l'amplitude du pic dans les impulsions THz rayonnées a été observée à partir du cristal BNA de 1.09 d'épaisseur. En outre, le champs crête des impulsions THz générés par le BNA est 1.8 fois supérieure à celle de champs crête des

impulsions THz rayonnées par le CdTe. Cependant, avec une forme d'onde monocyclique, l'impulsion THz principale émise par le CdTe a une durée relativement plus courte (~540 fs FWHM) que celle des impulsions THz émises par le BNA. D'autre part, les spectres de la transformation Fourier calculées montrent que le largueur de bande de THz du CdTe s'étend jusqu'à 2.5 THz, tandis que le spectre THz correspondant à la BNA a une bande passante

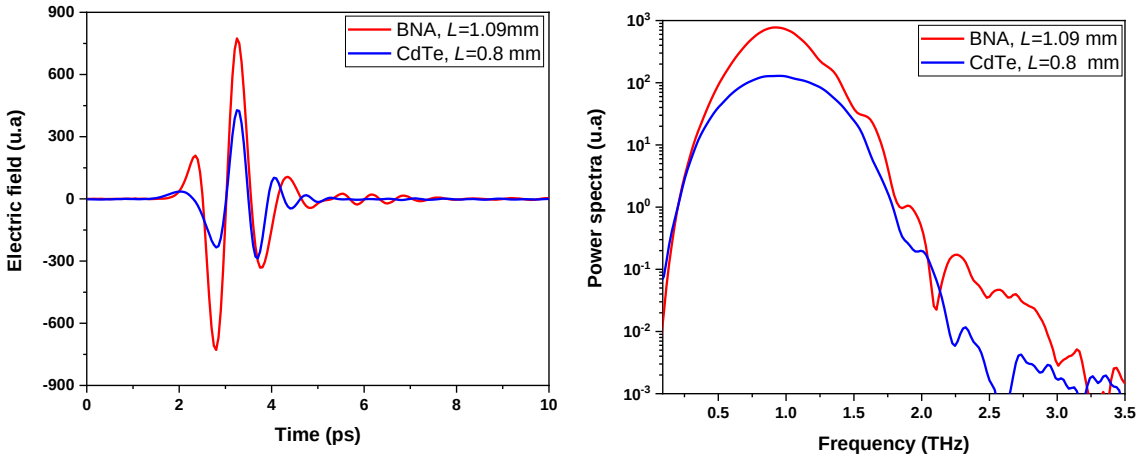

Figure 8-3 (a) waveforms and (b) FFT spectra of THz pulses emitted from BNA (red curve) and CdTe (blue curve) crystals in a nitrogen purged environment.

supérieure à 3 THz. Néanmoins, il est important de noter que la gamme dynamique du cristal BNA est limitée à 2.1 THz à cause d'un mode phonon fort existant autour de 2.3 THz (Figure 8-3 (b)) [214].

8.2.2 Génération d'impulsions THz intenses à polarisation elliptique en demi-cycle par des ILAPCA de ZnSe (Chapitre-3).

Cette nouvelle méthode expérimentale consiste à générer des impulsions THz quasi-cycliques intenses avec des états de polarisation variables par décalage temporel d'impulsions THz à polarisation croisée en utilisant une série d'antennes photoconductrices de grande ouvertures interdigitées (APCGOI) avec des électrodes horizontales et verticales. En faisant un décalage temporel entre deux impulsions THz à polarisation verticale et horizontale l'une par rapport à l'autre, les états de polarisation des impulsions THz rayonnées ont été variées de linéaire à quasi-circulaire sur un quart de cycle [218].

Afin d'obtenir un délai entre deux impulsions THz générées avec une polarisation orthogonale, différentes épaisseurs de masques de phase ont été utilisées pour couvrir les

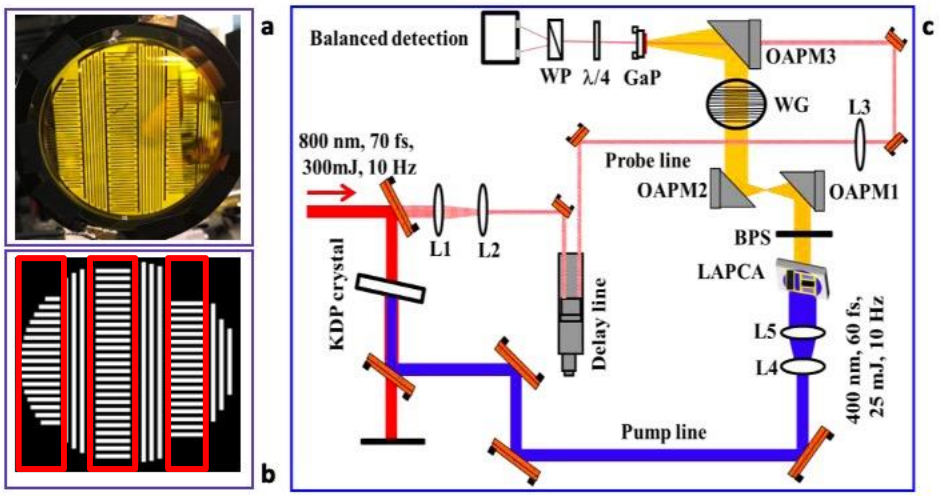

Figure 8-4 Image de l'APCGOI (a), son masque d'ombre, (b) le schéma de montage expérimentale. La zone rectangulaire entourée par les lignes rouges représente le masque d'ombre

électrodes horizontales et verticales. Par conséquent, les impulsions THz de haute intensité avec une amplitude de champ de pointe allant jusqu'à 70 kV/cm ont été générées avec des états de polarisation allant de la polarisation linéaire à la polarisation quasi-circulaire en utilisant la méthode proposée. L'une des principaux avantages de cette méthode est que l'amplitude et la forme temporelle, ainsi que les spectrales des impulsions THz rayonnées restent constantes pour tous les états de polarisation et demeurent colinéaires dans tout le volume de propagation spatiale. Ces propriétés uniques des impulsions THz quasi-circulaires de haute intensité générées par cette technique récente présentent un grand avantage pour l'étude et la surveillance continue des propriétés non linéaires des matériaux sélectifs en polarisation.

Les image de l'APCGOI de ZnSe et l'un des masques à retard respectifs recouvrant sa surface sont présentés sur les Figures 8-4 (a) et (b), respectivement. Pour la fabrication de l'APCGOI de ZnSe, la technique de photolithographie conventionnelle a été utilisée. Les électrodes de chrome et d'aluminium (Cr/Al) d'une épaisseur de 185 nm ont été déposées sur le substrat de ZnSe de 3 pouces de diamètre et d'une épaisseur de 1.5 mm. L'APCGO utilisée dans cette étude consiste en un substrat ZnSe de 3 pouces de diamètre et de 1.5 mm d'épaisseur. Des électrodes de chrome et d'aluminium (Cr/Al) d'une épaisseur totale de 185 nm ont été déposées sur le substrat par une technique de photolithographie classique. Le diamètre total de l'antenne composée de 6 unités d'électrodes horizontales et verticales alternées est de 62 mm. Chaque antenne présente la même distance inter-électrodes de 0.8 mm, ce qui est suffisant pour éviter l'effet de l'écrantage des charges spatiales. La surface totale éclairée par les électrodes verticales et horizontales est d'environ 4.3 cm^2, après avoir recouvert l'antenne d'un masque

d'ombre, soit presque la même surface que les unités d'électrodes verticales. Pour éviter les interférences destructives des impulsions THz générées dans le champ lointain, il est nécessaire d'utiliser un masque d'ombre sur le masque de retard pour couvrir les électrodes adjacentes de

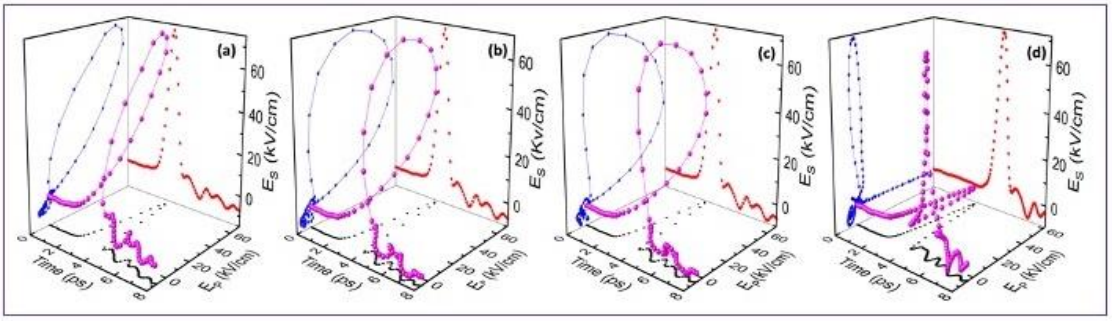

Figure 8-5 (a) Représentation 3D des formes d'onde des impulsions THz générées par les APCGOs interdigitées à 400 nm. La projection du champ électrique de l'impulsion THz avec une polarisation verticale et horizontale est indiquée par E_p et E_s, respectivement.

l'antenne. Les différents masques de retarde avec épaisseurs de 0.12, 0.20, 0.25 et 1 mm utilisées séparément pour couvrir les électrodes horizontales permettent de changer les états de polarisation des impulsions THz quasi-demi-cycles générées avec une amplitude égale, de linéaire à quasi-circulaire, correspondant à l'épaisseur des masques. Le montage expérimental permettant de générer des impulsions THz à partir de l'APCGOI de ZnSe est illustré dans la Figure 8-4 (c). Afin de générer des impulsion THz, l'APCGOI de ZnSe est illuminée par des impulsions laser de 15 mJ avec une durée et une fréquence de répétition de 60 fs et 10 Hz, respectivement, à 400 nm. La tension de polarisation maximale appliquée aux bornes de l'APCGOI a atteint jusqu'à 2,25 kV, avec une durée de 50 ns. Les impulsions THz générées ont été collectées et guidées vers les détecteurs à l'aide de deux miroirs paraboliques hors axe (OAPM) de 3 et 4 pouces de diamètre. L'état de polarisation des impulsion THz mesurées a été contrôlé par un polariseur à grille métallique positionné entre la deuxième et troisième mirrore parabolique. Les impulsions THz ont été détectées par la technique d'échantillonnage électro-optique en utilisant un cristal GaP avec une orientation cristallographique de (100) et une épaisseur de 300 µm en superposant des ondes THz avec les impulsions de la sonde à 800 nm sur le cristal. Les formes d'onde 3D des champs THz rayonnés et leurs projections sur les différents axes pour diverses épaisseurs de masque sont présentées sur la Figure 8-5. Comme le montre la Figure 8-5, l'utilisation des masques à retard avec les épaisseurs accrus de 0.12 à 1.0 mm nous permet de décaler temporellement de 0.2 à 1.7 ps les impulsions THz polarisées verticalement et horizontalement, respectivement. En augmentant le délai entre les impulsions THz polarisées verticalement et horizontalement de 0.4 ps à 0.5 ps, l'état de polarisation devient plus elliptique, tandis qu'en augmentant le délai entre deux impulsions THz polarisées

orthogonalement de 3.1 ps à 3.7 ps, l'état de polarisation devient circulaire sur une période d'un quart de cycle. En outre, l'utilisation d'un masque binaire d'une épaisseur de 0.25 mm, nous pouvons générer des impulsions THz quasi-circulaires sur un demi-cycle. Il est essentiel de noter que dans cette étude comme le masque de retard a été utilisé seulement sur les électrodes verticales, la rotation du plan de la polarisation est gauche. Nous pouvons changer la rotation de la polarisation de gauche à droite en changeant le recouvrement des électrodes horizontales par des électrodes verticales. Figure 8-6 (a) illustre les formes d'onde temporelles et les spectres respectifs des impulsions THz polarisées horizontalement et verticalement générées par l'APCGOI de ZnSe lorsqu'il est recouvert par le masque d'ombre de 0.25 mm. Les champs de crête calculés correspondant aux impulsions THz polarisées horizontalement et verticalement sont de 68 et 71 kV/cm, respectivement. La petite différence entre les champs THz crête mesurés est due à un désalignement léger du masque d'ombre sur l'antenne. Comme on peut le voir sur la Figure 8-6(a), la combinaison de ces deux impulsions polarisées verticalement et horizontalement nous donne une impulsion THz polarisée quasi-circulaire avec une amplitude de champ maximale de 81 kV/cm à 3.4 ps. Puisque le champ de crête des impulsions THz rayonnées par les APCs a un comportement linéaire en fonction du champ de polarisation appliqué, nous estimons un champ de crête maximal généré par les APCGOI de ZnSe d'environ 115 kV/cm pour les impulsions THz à polarisation quasi-circulaire de la source fournie dans ce travail. Figure 8-5 (b) illustre la dépendance de la différence de phase spectrale entre les impulsions THz polarisées verticalement et horizontalement en fonction de la fréquence lorsque l'APCGOI est recouvert de masques à retard avec les épaisseurs de 0.12, 0.20 et 0.25 mm. Comme le masque le plus fin entraîne une légère différence dans le déphasage, les impulsions THz relatives ont une polarisation presque linéaire. De même, une petite différence a été observée dans le déphasage entre les impulsions THz polarisées verticale et horizontale lorsque

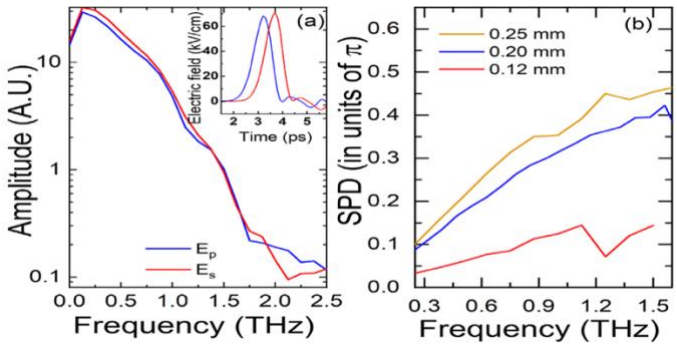

Figure 8-6 (a) Les bandes spectrales correspondant aux formes d'onde (encart) des impulsions THz polarisées horizontalement et verticalement rayonnées par le ZnSe ILAPCA (b) et les différences de phase spectrale entre les impulsions THz à polarisation horizontale et verticale lorsque le ZnSe ILAPCA est couvert par le masque à retard de 0,25 mm et pompé à 400 nm

l'antenne est couverte par les masques à retard de 0.20 et 0.25 mm d'épaisseur. En outre, il convient de mentionner que, par comparaison, la bande spectrale THz est différente lorsqu'on utilise des masques à retard opaques et des masques binaires de la même épaisseur de 0.25 mm (Figure 8-5 (c)). Cela peut être attribué à la nature des impulsions de sous-cycle THz, qui est différente de celle du comportement de polarisation circulaire de la lumière quasi-monochromatique.

8.3 FABRICATION ET LA CARACTERISATION DES ANTENNES PHOTOCONDUCTRICES MICRO-STRUCTURES PILOTÉES PAR DES IMPULSIONS DE SH DU LASER YTTERBIUM (CHAPITRE-4).

Ce chapitre présente nos études expérimentales sur la fabrication et la caractérisation des APCs de dipôle-H à l'échelle micrométrique déposées sur les substrats de CdTe et SI-GaAs. À cette fin, les performances du rayonnement THz des APCs de CdTe et de SI-GaAs fabriquées dans les mêmes conditions expérimentales avec des structures des électrodes identiques sont illuminées par les impulsions de GSH de laser Yb à 522 nm. Avant de présenter les résultats expérimentaux, nous démontrons brièvement le processus de conception et de fabrication des antennes.

La Figure 8-7 montre la vue par microscope optique de l'une des APCs fabriquées sur le substrat de CdTe. Toutes les antennes de CdTe et SI-GaAs présentées dans cette étude ont été fabriquées de même structure d'électrodes en utilisant de la méthode photolithographie standarde. Pour la fabrication des APCs de CdTe, nous avons utilisé des substrats commerciaux (ACROTEC, Japon) à double face polie avec une orientation cristallographique de <110>. La taille et l'épaisseur de ces substrats sont respectivement de 10 x 10 mm et de 800 ± 50 µm.

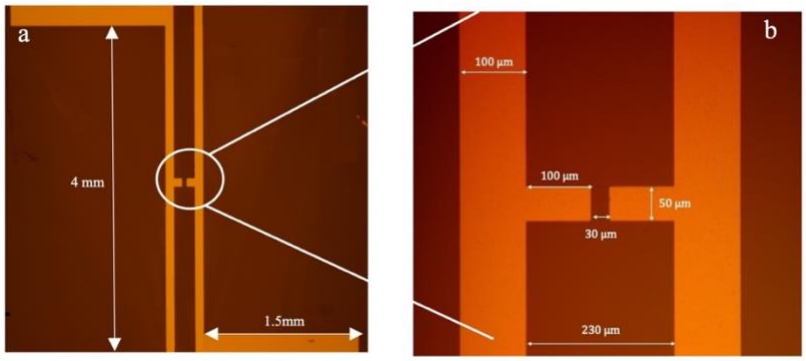

Figure 8-7 Image au microscope optique d'un APC en CdTe : (a) Vue de dessus de l'antenne ; (b) Agrandissement de 10x de la zone de l'écarte de l'antenne.

D'autre part, les APCs de SI-GaAs sont fabriquées sur des substrats avec une orientation cristallographique de <100> et une épaisseur de 500 µm obtenus commercialement par MTI, Corporation, CA, USA. Ces substrats possèdent d'une résistivité et de la mobilité de porteurs de charge de $3.16 \cdot 10^8$ Ω·cm, et 6180 cm^2/Vs, respectivement. Avant de procédé de fabrication, les substrats ont été nettoyés en deux étapes. La première étape de nettoyage a été réalisée avec des solvants organiques, en utilisant alternativement de l'acétone, de l'isopropanol et du méthanol pendant 10 min dans un four à ultrasons, avant de les rincer avec de l'eau désionisée. La deuxième étape consiste en un nettoyage à l'acide, en utilisant la nanostripe pendant 5 minutes. Ensuite, les substrats ont été préchauffés à 180C pendant 5 minutes et recuits thermiquement pendant 10 minutes à température ambiante. Ce traitement thermique commun permet d'éliminer les contaminants de surface et d'améliorer la morphologie de la surface des substrats. Dans l'étape suivante, nous avons déposé des photo-résistes ayant une épaisseur de ~400 nm sur et nous l'avons cuit à 115C pendant 5 minutes avant d'utiliser le processus d'exposition par faisceau laser. Ensuite, nous avons utilisé un système de lithographie sans masse (Heidelberg DWL-66 FS) pour réaliser des motifs à haute résolution sur les substrats. Des motifs de lignes droites en forme de H ayant une distance inter-électrodes de 30 µm avec une largeur et une longueur de 100 µm et 4 mm respectivement ont été exposés directement à la longueur d'onde de gravure de 405 nm. Les échantillons sont ensuite traités dans une chambre à plasma (Asher Gasonics Aura 1000) pour éliminer les polymères et les contaminants organiques avec des ions oxygène. Par la suite, les APC sont métallisés avec des couches de chrome (Cr) de 5 nm et d'or (Au) de 80 nm en les déposant sur les substrats par la technique d'évaporation par faisceau d'électrons standard en utilisant l'outil AXXIS de K. J. Lesker. Nous avons effectué un processus standard de lift-off pour enlever des couches photo-résine et recouvrir les électrodes d'antenne, comme la dernière étape de procédé de la fabrication des antennes. Avant la caractérisation des APCs, chacun d'eux a été soigneusement placé sur un support en Téflon perforé au centre, et ensuite monté sur un support de miroir cinématique de 2 pouces. Les électrodes de l'antenne ont ensuite été reliées à la source de tension externe par deux plaques de cuivre intermédiaires. Enfin, les antennes ont été montées sur un stage compact à 3 axes de haute précision (MBT602, Thorlabs) qui permet un alignement précis de l'émetteur à travers le foyer du faisceau de la pompe d'excitation.

Le montage expérimental pour la génération d'impulsions THz en espace libre par les APCs à l'échelle micrométrique est présenté sur la Figure 8-8. Les impulsions THz ont été générées et détectées en utilisant d'un montage de THz-TDS classique en mode transmission. Ce montage permet de générer des impulsions THz par des APCs et de les détecter par

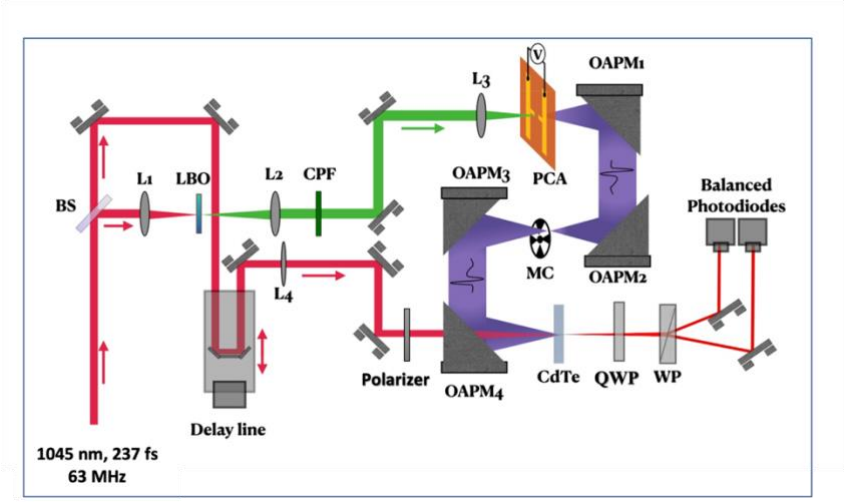

Figure 8-8 Schéma du montage expérimental pour la génération et la détection d'ondes THz par les APCs de CdTe et SI-GaAs de l'échelle micrométriques. CPF- le filtre passe-bande, OAPM-miroir parabolique hors axe, MC-hacheur mécanique, QWP- lame quart d'onde

échantillonnage électro-optique. La source de laser utilisée dans notre expérience est l'oscillateur HighQ-2 qui délivre des impulsions optiques d'une durée et le taux de répétition de 238 fs et 63 MHz, respectivement à la longueur d'onde fondamentale de 1045 nm. Le faisceau du laser d'une puissance moyenne de 620 mW est d'abord divisé par une lame séparatrice (UVFS), et 70% de la puissance totale a été utilisée pour la GSH par un cristal LBO d'une épaisseur de 3.7 mm. La puissance résiduelle de 30% est utilisée pour sonder les impulsion THz. Après la GSH, le faisceau ayant une puissance maximale de 75 mW à 522 nm est collimaté et filtré par un verre passe-bande en plastique coloré (FGB37-A, Thorlabs, USA), et ensuite focalisé sur l'APC par une lentille à une distance focale de 50 mm.

Les impulsions THz émises par les antennes ont été collectées et guidées par deux paires de miroirs paraboliques de 2 pouces hors d'axe vers le cristal détecteur CdTe de 1 mm d'épaisseur, associé à des photodétecteurs équilibrés en utilisant la technique EO classique. Le rapport signal-sur-bruit des impulsions THz détectées est amplifié par une détection synchrone utilisant l'amplificateur de verrouillage SR-830. Nous avons utilisé d'une source de la tension pour appliquer le champ de polarisation aux antennes. Les électrodes de l'antenne ont été liées par la peinture d'argent à la source de la tension. Comme nous avons réalisé une expérience de détection par amplificateur à verrouillage, les impulsions THz ont été hachées à une fréquence de 225 Hz. Les impulsions THz rayonnées ont été détectées à une constante de temps de 1s à partir de l'amplificateur à verrouillage en contrôlant le délai entre la sonde et le faisceau de la pompe avec un temps d'attente et un pas de 3s et 0,1s, respectivement. Les émetteurs sont placés au foyer du faisceau de pompe laser, dont le diamètre a été mesuré à 22 µm à l'aide d'une caméra CCD (Teledyne DALSA Genie HM640).

Figure 8-9 montre les formes d'onde temporelles et les spectres associés des impulsions THz rayonnées lorsque les APCs de SI-GaAs et en CdTe ont été excités à la même puissance de pompage de 45 mW et polarisés aux champs externes maximums de 25 kV/cm et 58,3 kV/cm à 522 nm respectivement. Les formes d'onde temporelles des impulsions THz émises par les APCs de CdTe et de SI-GaAs. Comme l'illustre la Figure 8-9 les impulsions THz générées par les deux émetteurs ont des formes d'onde monocycliques similaires, consistant en un pic positif principal d'une durée de 798 fs (1/e), qui est suivi d'un pic long de polarité opposée. La durée des impulsions THz générées est estimée à environ 4,3 ps. Puisque la durée de l'impulsion laser du faisceau de pompe exerce une forte influence sur la durée de l'impulsion THz émise par les APCs, les impulsions THz plus longues observées peuvent être principalement attribuées à la longue durée d'impulsion de notre laser à 522 nm. En effet, une durée d'impulsion plus longue induit un temps d'injection plus long des porteurs libres, ce qui crée un transitoire de courant plus lent. Par conséquent, l'impulsion THz émise par les APCs aura une durée plus longue et un champ électrique de pointe plus faible. Comme les deux formes d'onde ont presque la même durée temporelle, les spectres correspondants ont presque la même largeur de bande, s'étendant jusqu'à 2 THz (Figure 7-11(b)).

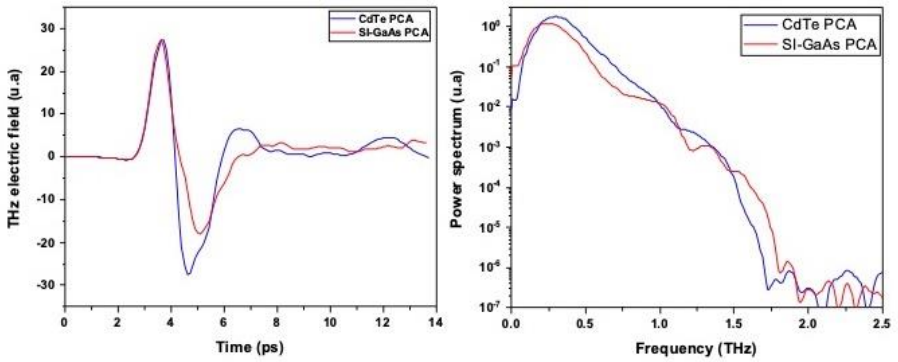

Figure 8-9 Formes d'onde et les spectres de l'impulsion THz émises par les APCs de CdTe- and SI-GaAs.

Pour tracer la dépendance du champ électrique THz de crête à crête en fonction de la puissance de la pompe dans les figures 8-10 (a) et (b), les données expérimentales ont été ajustées à l'aide de l'ajustement hyperbolique, nous avons utilisé l'équation suivante:

$$E_{THz} \propto \frac{F/F_0}{1 + F/F_0} \tag{8.1}$$

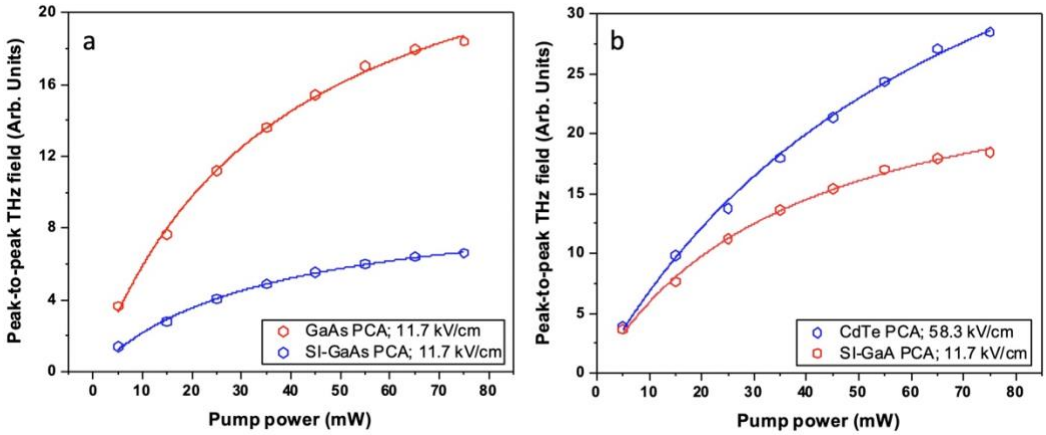

Figure 8-10 La dépendance de champs THz crête-à-crête en fonction de la puissance de la pompe du laser

(a) La dépendance de champs crête-à-crête des impulsions THz en fonction de la puissance de pompe émises par les APCs de CdTe (bleu) et de SI-GaAs (rouge) polarisées par une tension externe fixée à 11.7 kV/cm. (b) dépendance de champs crête-à-crête des impulsions THz en fonction de la puissance de pompe lorsque les APCs de CdTe (bleu) et de SI-GaAs (rouge) polarisées par les tensions externes maximales à 58.3 kV/cm et 11.7 kV/cm, respectivement

où F/F_0 est la puissance optique normalisée. La figure 7-12 (a) montre la dépendance du champ électrique THz de crête à crête par rapport à la puissance de pompage lorsque les antennes SI-GaAs et CdTe fonctionnent au même champ de polarisation externe de 11.7 kV/cm. Les champs crête des impulsions THz rayonnées par l'APC de SI-GaAs sont environ 2,8 fois plus élevés que le champ de crête des impulsions THz rayonnées par l'APC de CdTe lorsqu'elles sont pompées par la même puissance de 75 mW. Cependant, comme on peut le voir sur la figure 4-6 (b), lorsque le champ de polarisation externe appliqué à l'APC de CdTe est augmenté jusqu'à la valeur la plus élevée de 58,3 kV/cm, les impulsions THz rayonnées sont 1,52 fois plus élevées que le champ de crête des impulsions THz rayonnées par l'APC de GaAs polarisé à 11,7 kV/cm. Le champ crête plus élevée des impulsions THz générées par l'APC de GaAs à celle de champ crête des impulsions émises par l'APC de CdTe à la même condition de champ externe de 11,7 kV/cm peut être attribuée à la mobilité de porteurs supérieure (>4890 cm^2/Vs) de GaAs, par rapport à la mobilité du CdTe (~1100 cm^2/Vcm). En effet, la grande mobilité des porteurs entraînera plus grande densité de photocourant conduisant à une amélioration de l'efficacité de conversion maximale de l'APC tout en améliorant sa conductivité de surface.

Les amplitudes de champ THz crête à crête en fonction des champs de polarisation externes appliqués aux antennes photoconductrices sont présentées à la Figure 8-11 (a). Les APCs de SI-GaAs et CdTe ont été exploitées sous des champs de polarisation externes allant de 1,66 à 25 kV/cm et de 1.66 à 61 kV/cm, respectivement, et excitées à la même puissance de la pompe de 28 mW à 522 nm. Pour des champs de polarisation de 1.66 à 25 kV/cm, l'APC de SI-GaAs a

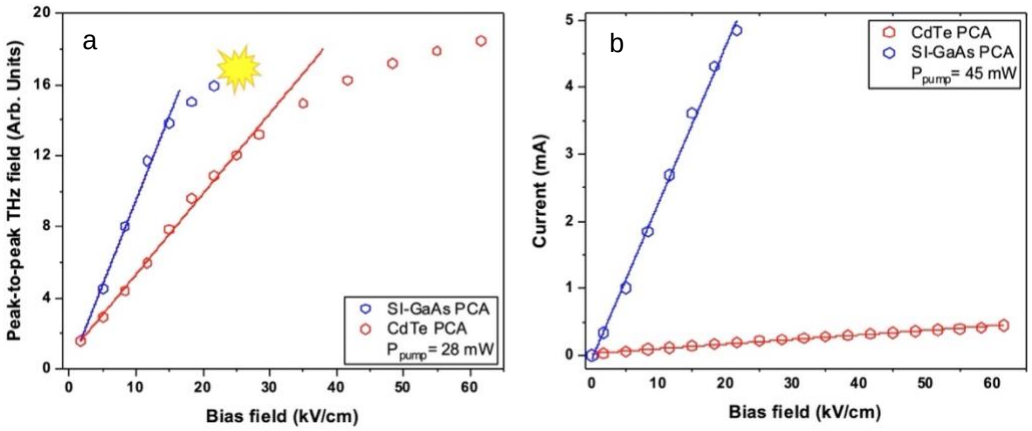

Figure 8-11(a) Champ électrique THz crête à crête en fonction du champ de polarisation des APCs de SI-GaAs et CdTe à une puissance de pompage fixe de 28mW (b) Photocourant respectif en fonction des champs de polarisation lorsque les deux antennes sont pompées à la puissance de pompage fixe de 45 mW

montrée une augmentation beaucoup plus rapide du champ THz crête à crête avec un champ de polarisation croissant par rapport aux APCs de CdTe. Par conséquent, l'amplitude du champ de crête des impulsions THz rayonnées par l'APC de SI-GaAs était 1.32 fois supérieure à celle du PCA en CdTe pour un champ de polarisation de 25 kV/cm. Cette efficacité supérieure de l'intensité de champ des impulsions THz rayonnées peut être attribuée à la mobilité relativement plus élevée des porteurs de SI-GaAs. Cependant, le champ de polarisation externe appliqué aux électrodes APC de GaAs est limité en raison de la décharge par effet corona et de la surchauffe de l'antenne, ce qui a conduit à sa destruction. D'autre part, la résistivité foncée plus élevée des antennes en CdTe a permis d'augmenter le champ de polarisation appliqué à 61 kV/cm à travers les électrodes de l'antenne sans observer de décharge corona. Par conséquent, à ce champ de polarisation externe plus élevé de 61 kV/cm, l'intensité de champ de crête des impulsions THz provenant de l'APC de CdTe a atteint une efficacité jusqu'à 1,17 fois supérieure à celle de l'intensité de champ de crête des impulsions THz rayonnées par l'APC de SI-GaAs lorsqu'il est piloté au champ de polarisation maximal de 25 kV/cm. En effet, comme nous pouvons le voir sur la Figure 8-11 (b), la résistivité foncée plus élevée (~10^{10} Ω cm) du CdTe a réduit l'échauffement des PCA en CdTe par un courant fondu plus faible, par rapport aux substrats SI-GaAs à résistivité foncée relativement faible (10^6-10^8 Ω cm). Par conséquent, l'échauffement thermique de l'antenne à des champs de polarisation relativement faibles a conduit à la rupture des APCs de SI-GaAs. Il convient également de mentionner que pour des champs de polarisation relativement faibles appliqués aux électrodes, les deux antennes ont montré un comportement linéaire typique dans l'augmentation des champs THz de crête à crête. Cependant, lorsque les champs de polarisation appliqués sont augmentés à plus de 15 kV/cm et 28,3 kV/cm pour les APCs de SI-GaAs et CdTe,

respectivement, l'échelle des champs THz crête à crête devient saturée. Cela peut être principalement attribué à l'échauffement par effet Joule dans les dispositifs en raison de l'augmentation des densités de courant. Ce phénomène a été observé précédemment sur les PCAs en SI-GaAs lorsqu'ils sont pompés par des impulsions laser Ti:Sapphire à 800 nm [238,270].

8.4 OPTIMISATION DES PERFORMANCES DU RAYONNEMENT THZ DES APCs PAR DEPOT DE NANOPARTICULES SUR LEURS SURFACES PAR L'ABLATION DU LASER PULSÉE (CHAPITRE-5).

Ce chapitre résume nos études systématiques sur l'amélioration du rayonnement THz par les APCs décorées avec des nanoparticules (NPs) remplies par la méthode de dépôt par une ablation laser pulsée (PLD). À cette fin, des APCs de dipôle H à l'échelle micrométriques fabriquées sur les substrats de SI-GaAs sont décorées avec différentes concentrations de NPs, et leurs performances de rayonnement ont été comparées à celles d'antennes non-décorées. Dans un premier temps, nous présentons une étude systématique de la génération de THz dans l'espace libre par des APCs de SI-GaAs décorés avec différentes concentrations de nanoparticules d'or métalliques (Au-NPs). L'amplitude crête-à-crête des impulsions THz rayonnées par les APCs avec différentes concentrations d'Au-NPs correspondant au nombre d'impulsions d'ablation laser telles que NLP=500, 1000, 1250, et 1500 sera comparée à l'amplitude THz crête des impulsions THz rayonnées par les APCs fabriquées sur le substrat SI-GaAs nu (NLP=0). Les avantages et les limites des particules de NP métalliques pour la décoration des APCs seront également brièvement discutés. Ensuite, compte tenu des limites des APCs décorées de NP métalliques, nous présenterons notre travail préliminaire sur les APCs décorés de NPs de sulfure de plomb semi-conducteur (PbS). La méthode PLD proposée pour la nanodécoration dans ce travail permet un dépôt direct de NPs métalliques et semi-conducteurs de haute qualité sur la zone active des APCs. Cette technique directe ouvre la porte à une méthode simple et relativement moins-cher pour améliorer l'efficacité des micro-antennes pour l'émission et la détection THz pulsée. En outre, la capacité de la déposition d'une grande quantité de NPs uniformes sur une grande surface (jusqu'à 6 pouces) par la méthode PLD peut ouvrir d'une opportunité prometteuse pour le développement des APCGOs.

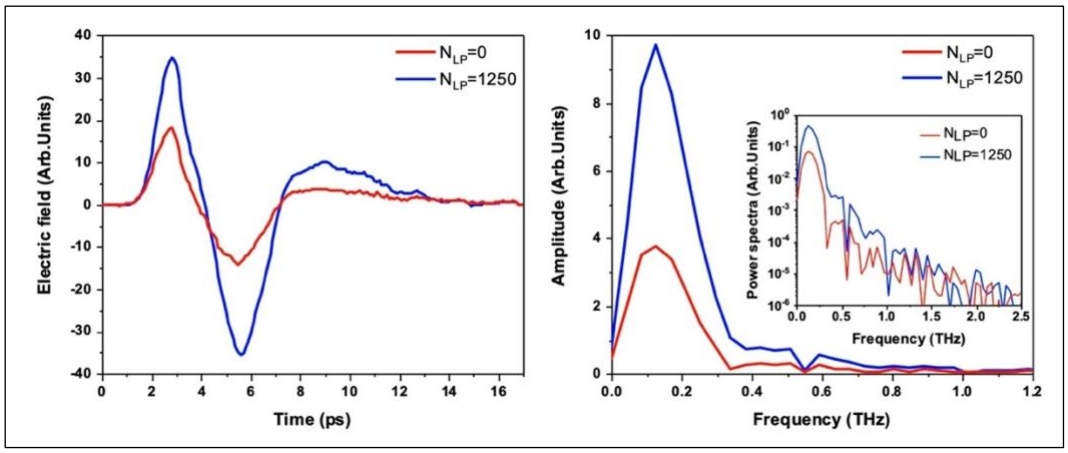

Figure 8-12 (a) Formes d'onde THz et (b) spectres THz associés générés une APC de SI-GaAs lorsqu'il est excité par une puissance de pompe de 45 mW au champ de polarisation externe de 16,6 kV/cm avant et après la décoration avec des Au-NPs au NLP=1250. L'encart de la figure 5-2 (b) montre les spectres de puissance des impulsions THz respectives.

Les formes d'onde et les spectres respectives des impulsions THz générées par les APCs de SI-GaAs non-décorées et décorées par des Au-NPs à N_{LP}=1250 ont été présentées dans la Figure 8-12. Dans cette étude, les antennes sont étudiées dans la même condition expérimentale pompées par une puissance de laser à 45 mW à 50V. Les deux formes d'onde sont de nature monocyclique avec un pic positif suivi d'un pic négatif avec presque la même amplitude. L'amplitude du champ THz pour l'antenne avec décoration NP est plus de 2 fois supérieure à celle de l'antenne non-décorée. Figure 8-12 montre le champ électrique THz de crête à crête en fonction (a) de la puissance optique et (b) du champ électrique de polarisation pour l'antenne NLP = 0 et NLP = 1250. Après le processus de décoration, le champ de crête des impulsions THz rayonnées présente une amplification supérieure à 2,06 fois lorsque l'antenne est excitée par une puissance de pompage maximale de 55 mW à un champ de polarisation externe de 15 kV/cm, par rapport à une antenne non décorée. L'échelle du champ THz de crête en fonction de la tension de polarisation est linéaire. Au contraire, l'échelle du champ de crête THz en fonction de la puissance optique est hyperbolique dans les deux cas. Cependant, nous constatons que le régime de saturation du champ de crête THz en fonction de la puissance optique apparaît plus rapidement lorsque les APCs sont pompés à 50 mW. Ce comportement de saturation est en bon accord avec la théorie de la saturation du champ électrique THz de pointe en fonction de la fluence optique, qui peut être attribuée à l'augmentation de la densité des porteurs photo-générées injectés de la bande de valence à la bande de conduction avec l'augmentation de la puissance du laser de commande. Par conséquent, la mobilité supérieure des porteurs de 6400 cm^2/Vs dans le SI-GaAs conduira à la saturation du champ THz avec une énergie plus élevée.

D'autre part, la dépendance de l'amplitude THz crête à crête par rapport au champ de polarisation suit une caractéristique linéaire typique lorsque la puissance du laser de pompe est maintenue constante à 45 mW. La comparaison des champs crête-à-crête des impulsions THz

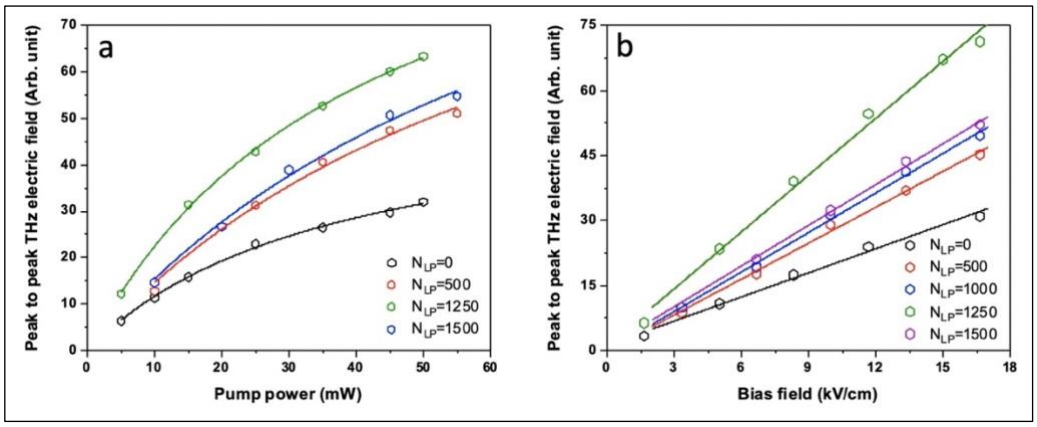

Figure 8-13 Variation of the generated THz signal amplitude with both (a) incident laser pump power when bias voltage is fixed to be 50V and as a function of the applied bias field when the optical pump power is fixed to be 45 mW for various N_{LP}

rayonnées après la décoration à N_{LP}=1250 est montrée un rendement 2,24 fois supérieur des impulsions THz rayonnées a été obtenu lorsque l'antenne nano-décorée N_{LP}= 0 a été polarisée à un champ de polarisation de 16,6 kV/cm. Nous notons que nous n'avons pas été en mesure d'appliquer un champ de polarisation supérieur à 50 V ou une puissance de pompe optique supérieure à 55 mW. En effet, au-delà de cette valeur, toutes les antennes, avec ou sans décoration, ont présenté des défaillances dues à une rupture thermique. Il est bien connu que la plupart des défaillances des antennes THz sont dues à des problèmes thermiques, comme les études précédentes réalisées sur les PCA nanodécorés. Il convient de noter que l'Au-NPs peuvent également entraîner une diminution de la tension de claquage entre les électrodes du PCA en raison de l'augmentation des champs de polarisation entre les NPs et les électrodes. Cependant, dans notre travail, le champ de claquage mesuré pour toutes les antennes décorées avec Au-NP était d'environ 23,3 kV/cm, ce qui est presque identique aux champs de claquage des antennes fabriquées sur des substrats nus.

Figure 8-14 montre le rapport du champ THz crête à crête entre les antennes décorées par différentes N_{LP} tels que 500, 1000, 1250 et 1500 et l'antenne non-décorée à N_{LP} = 0 lorsqu'elles sont pompées par une puissance fixe à 45 mW à une tension de polarisation constante de 50 V. Nous devons noter que cette mesure a été effectuée plusieurs fois et nous faisons la moyenne des résultats. De plus, la barre d'erreur a été calculée en utilisant les valeurs de champ électrique THz crête à crête prises sur deux antennes différentes correspondant à chaque valeur N_{LP}. Figure 8-14 montre clairement que le taux d'amplification dépend fortement de la concentration de NP sur l'antenne. Entre N_{LP} = 0 et N_{LP} = 500, nous avons une amélioration de ~50%, mais l'amélioration entre N_{LP} = 500 et 1000 n'est que de 10%. Plus surprenant, le facteur d'amélioration

entre N_{LP} = 1000 et N_{LP} = 1250 est de 41 %, qui diminue ensuite entre N_{LP} = 1250 et N_{LP} = 1500 de 37 %. Cette courbe montre que l'amélioration du champ de crête rayonné est fortement non linéaire.

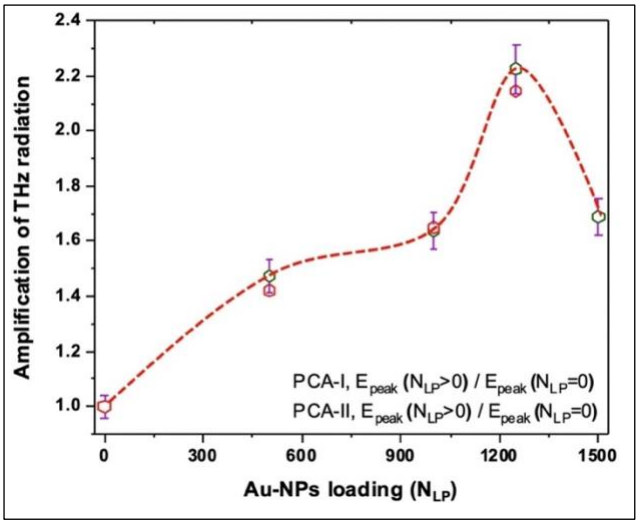

Figure 8-14 Dépendance de l'amplification de champs crête de THz en fonction de la densité des Au-NPs selon N_{LP}. La ligne en pointillés est utilisée comme un œil de guidage.

Afin de comparée l'amplification du rayonnement THz par les APCs décorrées avec différentes valeurs de N_{LP}, les propriétés optiques des films Au-NP (déposés sur des substrats de quartz) ont été caractérisées en mesurant leur transmittance et leur réflectance UV-Vis. Les Figures 8-15 (a) et 8-15(b) montrent le coefficient d'absorption et la réflectance optique des films Au-NP pour différentes valeurs de N_{LP}. L'absorption optique des films Au-NP à la longueur d'onde de 522 nm diminue de ~$5,6\times10^5$ cm^{-1} à ~$3,8\times10^5$ cm^{-1} lorsque le N_{LP} passe de 750 à 1500, puis reste presque constante à environ (3,7±0,2) $\times10^5$ cm^{-1} pour des valeurs de N_{LP} plus élevées. Ceci peut également être traduit par la profondeur d'absorption des films Au-NP à 522 nm, comme le montre l'encart de la Figure 8-15 (a). En effet, la profondeur d'absorption augmente linéairement avec le N_{LP} jusqu'à atteindre ~28 nm pour un $N_{LP} \geq 1500$. D'autre part, on peut également voir dans l'encart de la Figure 8-15 (a) que la réflectance des films Au-NP à 522 nm augmente linéairement de ~20% à ~30% lorsque le N_{LP} passe de 750 à 2000. Par exemple, à N_{LP} = 1250, l'épaisseur de la profondeur d'absorption des Au-NP à 522 nm est de ~24 nm, dépassant ainsi l'épaisseur du film de Au-NP (~11 nm). Pour N_{LP} = 2000, la profondeur d'absorption est légèrement plus importante (~26 nm), mais la réflectance est beaucoup plus élevée (30% contre 23,5%). Cela suggère que l'absorption optimale de la lumière se produirait pour le meilleur compromis entre la plus grande profondeur d'absorption possible et la réflectance optique la plus faible. D'après

l'encart de la figure 8-15(a), à une longueur d'onde incidente de 522 nm, une telle condition optimale devrait se produire pour NLP= 1250 ou 1500.

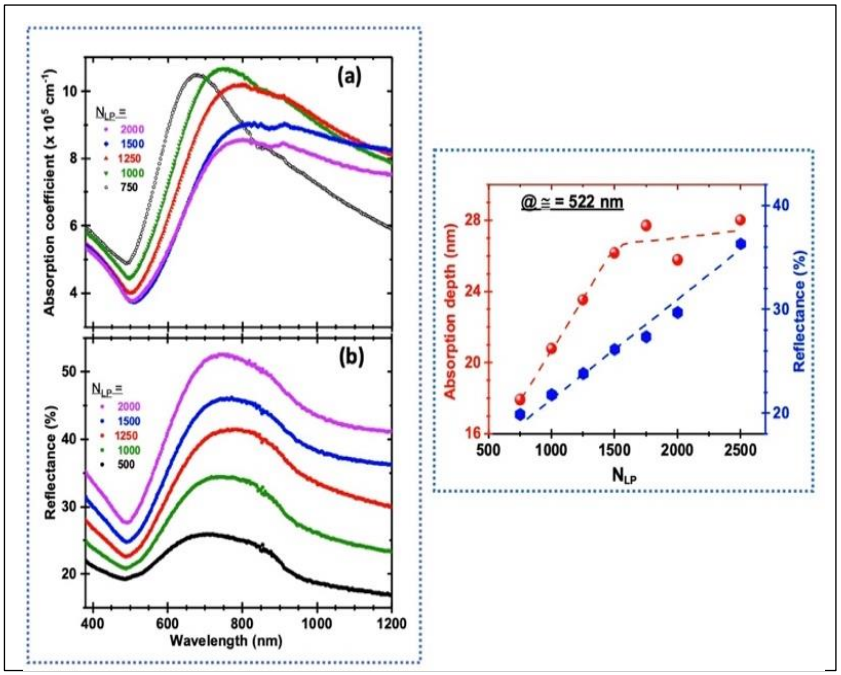

Figure 8-15(a) Coefficient d'absorption optique des films Au-NPs déposés à différentes valeurs de N_{LP} sur des substrats de quartz; (b) les spectres de réflectance des films Au-NPs en fonction de leur condition de dépôt N_{LP}. L'encart de la figure (a) montre la dépendance du N_{LP} à la fois de la profondeur d'absorption et de la réflectance à la longueur d'onde de 522 nm.

Enfin, nos observations indiquent que les APCs fabriquées sur des substrats nanodécorés présentent une plus grande stabilité thermique que ceux intégrés dans les substrats nus (données supplémentaires). Étant donné que l'échauffement excessif des substrats sous une puissance de pompage élevée est l'un des principaux inconvénients des APCs conventionnelles et conduit à leur dégradation thermique, l'utilisation de NPs métalliques pourrait être une solution importante pour surmonter cette limitation. L'amélioration de la stabilité thermique des APCs déposées par Au-NP peut être attribuée à l'amélioration de la conductivité thermique totale des substrats décorés de NPs par la conductivité thermique plus élevée des Au-NP métalliques. En effet, la conductivité thermique des Au-NP est de 3,14 W/cm×K, ce qui est six fois supérieur à la conductivité thermique des substrats GaAs (0,55 W/cm×K) [12].

Finalement, il faut noter que malgrès ces avantanges exceptionneles des APCs décorées par des Au-NPs montrent un inconvénient critique de courts-circuits lorsque les antennes sont surchargées de nanoparticules métalliques, ce qui conduit à une chute excessive de la résistivité sombre à travers les électrodes de l'antenne, limitant le champ de polarisation externe appliqué.

En effet, nos expériences ont indiqué que lorsque la densité de Au-NP est augmentée jusqu'à plus de NLP=1500 à la surface des APCs de SI-GaAs, la résistivité diminue fortement jusqu'à quelques dizaines d'Ohm, ce qui limite le champ de polarisation externe appliqué aux bornes des antennes. A cet effet, nous proposons de remplacer les NPs métalliques sur la zone d'excitation active des APCs par des PbS-NPs semi-conductrices, ce qui pourrait être une solution prometteuse pour surmonter cette limitation. Avec une bande interdite directe de 0,41 eV et une durée de vie des porteurs plus courte, allant de quelques dizaines de ps à plusieurs ns, les PbS-NPs pourraient être un matériau alternatif pour la décoration des PCAs. Parmi les autres semi-conducteurs-NP, le dépôt de PbS-NP à bande interdite étroite sur des PCA en SI-GaAs leur permettra d'être excités avec une énergie de photon relativement plus élevée du faisceau de pompe à 522 nm. De plus, la spectroscopie UV-NIR typique des NPs de PbS déposées sur des substrats de quartz à l'aide de la PLD montre qu'avec une densité croissante de NLP de 500 à 5000 indique que ces NPs présentent de l'absorption de photon élevé dans la région Vis-NIR. En tenant compte ces dernières, nous anvons réalisé une série des études préliminaires sur les APCs de SI-GaAs décorée avec les PbS-NPs.

Figure 8-16 montre les mesures de la résistance aux bornes des APCs de SI-GaAs décorées avec différentes N_{LP} des PbS NPs, sans illumination laser. Lorsque la concentration de

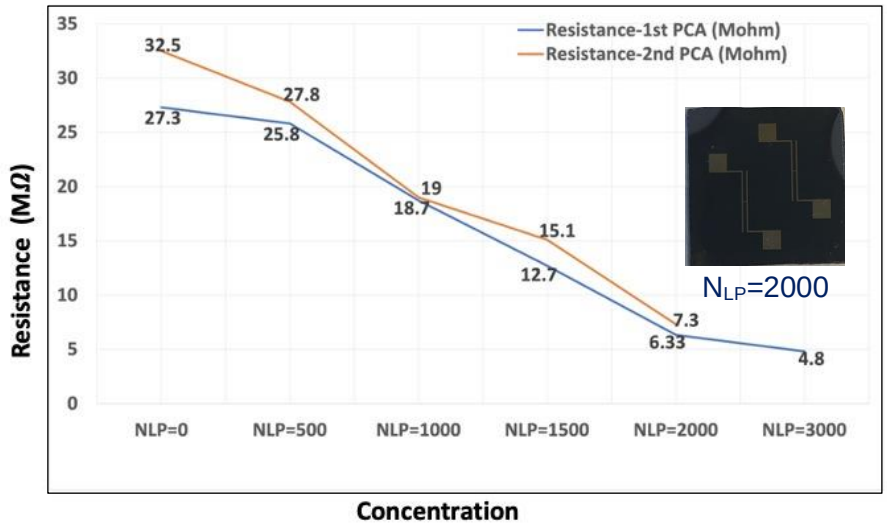

Figure 8-16 Résistance dépendante de la concentration des APCs de GaAs décorées par PbS-NPs avec différents N_{LP}. Le courbes orange et bleue décrivent les résistances mesurées aux bornes APC-1 et APC-2 déposées sur les mêmes substrats sans illumination laser. L'encart montre la vue de dessus des APCs décorées par des PbS-NPs avec N_{LP}=2000.

PbS-NPs dans la zone d'excitation active est augmentée de NLP=0 à 3000, la résistance de l'antenne diminue de 27,3 à 4,3 MΩ. Pour étudier les performances de rayonnement THz des antennes décorées de PbS-NP, nous avons utilisé le même montage expérimental décrit dans la

figure 8-8. Dans la même condition optimale, une Si-GaAs à dipôle en H avec un espace, une largeur et une longueur de 30 µm,100 µm et 4 mm, respectivement (Figure 8-7) a été étudiée avant et après la décoration NLP=500. L'antenne a été polarisée à un champ externe de 15 kV/cm en illuminant une puissance de pompe de 35 mW à 522 nm. Puisque les résultats obtenus par les autres APCs décorées par des PbS-NPs avec N_{LP} >500 nécessitent des expériences supplémentaires pour la confirmation, nous présentons uniquement nos résultats obtenus à partir de N_{LP} décorés avec des PbS-NPs à NLP=500 qui est confirmé par plusieurs antennes.

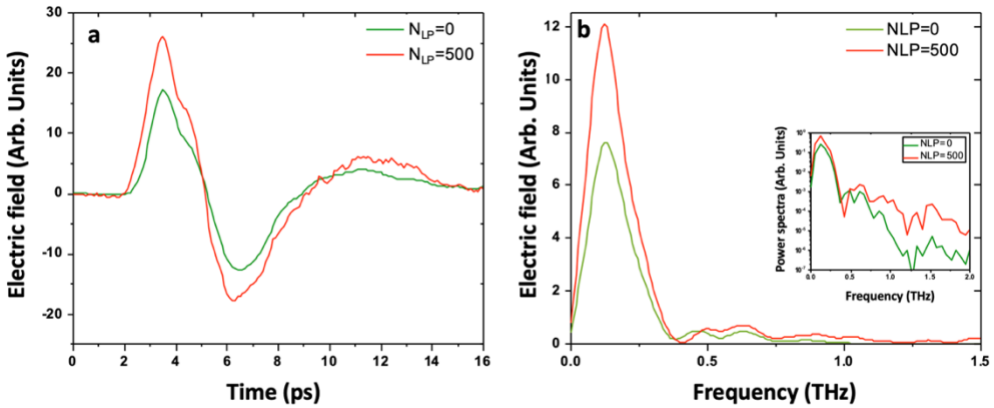

Figure 8-17 (a) Formes d'onde et (b) amplitudes spectres respectifs des impulsions THz rayonnées par une APC de SI-GaAs avant et après le dépôt par des PbS-NPs avec N_{LP}=500. L'encart de la figure (b) montre les spectres de puissance des impulsions THz émises avant et après la décoration.

La figure 8-17 montre les formes d'onde et les amplitudes spectrales respectives d'une APC de SI-GaAs décorée par des PbS-NP avant et après la nanodécoration par N_{LP}=500. Comme on peut le voir sur la figure 8-17 (a), les impulsions THz émises ont presque les mêmes formes d'onde mono-cycle asymétriques avant et après la décoration avec des PbS-NPs. L'intensité de champ maximale des impulsions THz rayonnées par l'antenne après la décoration des PbS-NP avec N_{LP}=500 a une efficacité presque 1,52 fois supérieure à celle de l'intensité de champ maximale des impulsions THz rayonnées avant la décoration à N_{LP}=0. La transformée de Fourier des formes d'onde dans le domaine temporelle montre qu'avec un pic spectral situé à environ 120 GHz, les spectres de THz dans la domaine fréquentielle restent à l'inferieur de 1 THz (Figure 8-17 (b)).

La dépendance de champ crête-à-crête de THz en fonction de champs de polarisation externes montre que les impulsions THz rayonnées par l'émetteur avant et après la décoration NLP=500 ont un comportement linéaire lorsqu'elles sont excitées à une puissance de pompe fixe de 45 mW en augmentant le champ de polarisation de 0 à 17 kV/cm (Figure 8-18(a)). Le champs crête-à-crête THz en fonction de la puissance de la pomp optique de 522 nm montre un comportement d'échelle typique de crête à crête pour les deux cas lorsque l'antenne est polarisée

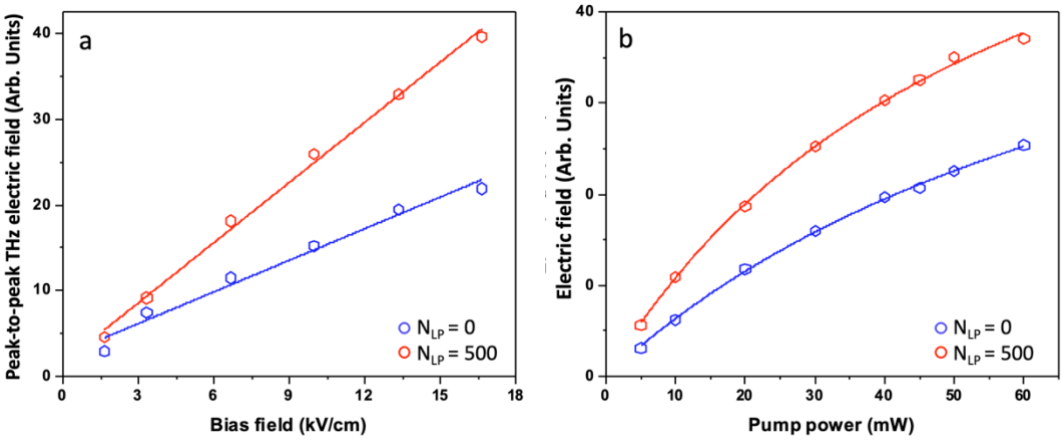

Figure 8-18 Le champ crête-à-crête de THz en fonction de champs de polarisation (a), et la puissance de la pompe optique (b).

à un champ continu fixe de 15 kV/cm (Figure 8-18). Les résultats montrent que des dépendances linéaires ne sont trouvées qu'à de faibles puissances de pompe et que la puissance de rayonnement THz sature à des puissances de pompe plus élevées.

Ces études préliminaires ont montré que les PbS-NPs ont le potentiel d'augmenter la performance de rayonnement des PCAs. Cependant, des études détaillées sont nécessaires pour déterminer l'efficacité des impulsions THz rayonnées pour des concentrations plus élevées de PbS-NPs.

REFERENCES

1. J. H. Schut, "Terahertz is Making Waves in the Plastics Sector," Plast. Eng. **73**, 18–24 (2017).
2. M. Tonouchi, "Cutting-edge terahertz technology," Nat. Photonics **1**, 97–105 (2007).
3. L. Yu, L. Hao, T. Meiqiong, H. Jiaoqi, L. Wei, D. Jinying, C. Xueping, F. Weiling, and Z. Yang, "The medical application of terahertz technology in non-invasive detection of cells and tissues: opportunities and challenges," RSC Adv. **9**, 9354–9363 (2019).
4. E. Pickwell and V. P. Wallace, "Biomedical applications of terahertz technology," J. Phys. D. Appl. Phys. **39**, R301 (2006).
5. M. C. Kemp, P. F. Taday, B. E. Cole, J. A. Cluff, A. J. Fitzgerald, and W. R. Tribe, "Security applications of terahertz technology," https://doi.org/10.1117/12.500491 **5070**, 44–52 (2003).
6. P. H. Siegel, "Terahertz technology," IEEE Trans. Microw. Theory Tech. **50**, 910–928 (2002).
7. P. H. Siegel, "Terahertz technology in biology and medicine," IEEE Trans. Microw. Theory Tech. **52**, 2438–2447 (2004).
8. Q. Sun, Y. He, K. Liu, S. Fan, E. P. J. Parrott, and E. Pickwell-MacPherson, "Recent advances in terahertz technology for biomedical applications," Quant. Imaging Med. Surg. **7**, 345 (2017).
9. C. Yu, S. Fan, Y. Sun, and E. Pickwell-MacPherson, "The potential of terahertz imaging for cancer diagnosis: A review of investigations to date," Quant. Imaging Med. Surg. **2**, 33 (2012).
10. D. H. Auston, K. P. Cheung, and P. R. Smith, "Picosecond photoconducting Hertzian dipoles," Appl. Phys. Lett. **45**, 284 (1998).
11. S. Maehrlein, A. Paarmann, M. Wolf, and T. Kampfrath, "Terahertz Sum-Frequency Excitation of a Raman-Active Phonon," Phys. Rev. Lett. **119**, 127402 (2017).
12. N. Fuse, R. Sato, M. Mizuno, K. Fukunaga, K. Itoh, and Y. Ohki, "Observation and analysis of molecular vibration modes in polylactide at terahertz frequencies," Jpn. J. Appl. Phys. **49**, 1024021–1024028 (2010).
13. K. Shiraga, Y. Ogawa, N. Kondo, A. Irisawa, and M. Imamura, "Evaluation of the hydration state of saccharides using terahertz time-domain attenuated total reflection spectroscopy," Food Chem. **140**, 315–320 (2013).
14. J. A. Zeitler, P. F. Taday, D. A. Newnham, M. Pepper, K. C. Gordon, T. Rades, P. F. Taday, and J. A. Zeilter, "Terahertz pulsed spectroscopy and imaging in the pharmaceutical setting - a review," J. Pharm. Pharmacol. **59**, 209–223 (2007).
15. P. Han, X. Wang, Y. Zhang, P. Han, X. Wang, and Y. Zhang, "Time-Resolved Terahertz Spectroscopy Studies on 2D Van der Waals Materials," Adv. Opt. Mater. **8**, 1900533 (2020).
16. T. F. Nova, A. Cartella, A. Cantaluppi, M. Först, D. Bossini, R. V. Mikhaylovskiy, A. V. Kimel, R. Merlin, and A. Cavalleri, "An effective magnetic field from optically driven phonons," Nat. Phys.

13, 132–136 (2017).

17. J. Walowski and M. Münzenberg, "Perspective: Ultrafast magnetism and THz spintronics," J. Appl. Phys. **120**, 140901 (2016).

18. Z. Dai, M. Manjappa, Y. Yang, T. Cai Wei Tan, B. Qiang, S. Han, L. Jie Wong, F. Xiu, W. Liu, R. Singh, Z. Dai, M. Manjappa, T. C. W Tan, S. Han, R. Singh, W. Liu, Y. Yang, F. Xiu, B. Qiang, and L. J. Wong, "High Mobility 3D Dirac Semimetal (Cd3As2) for Ultrafast Photoactive Terahertz Photonics," Adv. Funct. Mater. **31**, 2011011 (2021).

19. Y. Hu, T. Jiang, J. Zhou, H. Hao, H. Sun, H. Ouyang, M. Tong, Y. Tang, H. Li, J. You, X. Zheng, Z. Xu, and X. Cheng, "Ultrafast terahertz transmission/group delay switching in photoactive WSe2-functionalized metaphotonic devices," Nano Energy **68**, 104280 (2020).

20. H. A. Hafez, X. Chai, A. Ibrahim, S. Mondal, D. Férachou, X. Ropagnol, and T. Ozaki, "Intense terahertz radiation and their applications," J. Opt. **18**, 093004 (2016).

21. Y. Zhang, K. Li, and H. Zhao, "Intense terahertz radiation: generation and application," Front. Optoelectron. 2020 141 **14**, 4–36 (2020).

22. H. Hirori and K. Tanaka, "Dynamical Nonlinear Interactions of Solids with Strong Terahertz Pulses," http://dx.doi.org/10.7566/JPSJ.85.082001 **85**, (2016).

23. L. Razzari, F. H. Su, G. Sharma, F. Blanchard, A. Ayesheshim, H. C. Bandulet, R. Morandotti, J. C. Kieffer, T. Ozaki, M. Reid, and F. A. Hegmann, "Nonlinear ultrafast modulation of the optical absorption of intense few-cycle terahertz pulses in n -doped semiconductors," Phys. Rev. B - Condens. Matter Mater. Phys. **79**, 193204 (2009).

24. X. Chai, X. Ropagnol, S. M. Raeis-Zadeh, M. Reid, S. Safavi-Naeini, and T. Ozaki, "Subcycle Terahertz Nonlinear Optics," Phys. Rev. Lett. **121**, 143901 (2018).

25. H. Y. Hwang, J. Hebling, K.-L. Yeh, K. A. Nelson, and M. C. Hoffmann, "THz-pump/THz-probe spectroscopy of semiconductors at high field strengths [Invited]," JOSA B, Vol. 26, Issue 9, pp. A29-A34 **26**, A29–A34 (2009).

26. J. Hebling, M. C. Hoffmann, H. Y. Hwang, K. Lo Yeh, and K. A. Nelson, "Observation of nonequilibrium carrier distribution in Ge, Si, and GaAs by terahertz pump-terahertz probe measurements," Phys. Rev. B - Condens. Matter Mater. Phys. **81**, 035201 (2010).

27. M. C. Hoffmann, J. Hebling, H. Y. Hwang, K. Lo Yeh, and K. A. Nelson, "Impact ionization in InSb probed by terahertz pump-terahertz probe spectroscopy," Phys. Rev. B - Condens. Matter Mater. Phys. **79**, 161201 (2009).

28. H. Y. Hwang, N. C. Brandt, H. Farhat, A. L. Hsu, J. Kong, and K. A. Nelson, "Nonlinear THz conductivity dynamics in P-Type CVD-grown graphene," J. Phys. Chem. B **117**, 15819–15824 (2013).

29. H. A. Hafez, S. Kovalev, J. C. Deinert, Z. Mics, B. Green, N. Awari, M. Chen, S. Germanskiy, U. Lehnert, J. Teichert, Z. Wang, K. J. Tielrooij, Z. Liu, Z. Chen, A. Narita, K. Müllen, M. Bonn, M.

Gensch, and D. Turchinovich, "Extremely efficient terahertz high-harmonic generation in graphene by hot Dirac fermions," Nat. 2018 5617724 **561**, 507–511 (2018).

30. R. Matsunaga, N. Tsuji, H. Fujita, A. Sugioka, K. Makise, Y. Uzawa, H. Terai, Z. Wang, H. Aoki, and R. Shimano, "Light-induced collective pseudospin precession resonating with Higgs mode in a superconductor," Science (80-.). 1145–1149 (2014).

31. R. Matsunaga, Y. I. Hamada, K. Makise, Y. Uzawa, H. Terai, Z. Wang, and R. Shimano, "Higgs amplitude mode in the bcs superconductors Nb1-xTi xN induced by terahertz pulse excitation," Phys. Rev. Lett. **111**, 057002 (2013).

32. R. Mankowsky, A. Subedi, M. Först, S. O. Mariager, M. Chollet, H. T. Lemke, J. S. Robinson, J. M. Glownia, M. P. Minitti, A. Frano, M. Fechner, N. A. Spaldin, T. Loew, B. Keimer, A. Georges, and A. Cavalleri, "Nonlinear lattice dynamics as a basis for enhanced superconductivity in YBa2Cu3O6.5," Nat. 2014 5167529 **516**, 71–73 (2014).

33. M. Först, R. I. Tobey, H. Bromberger, S. B. Wilkins, V. Khanna, A. D. Caviglia, Y. D. Chuang, W. S. Lee, W. F. Schlotter, J. J. Turner, M. P. Minitti, O. Krupin, Z. J. Xu, J. S. Wen, G. D. Gu, S. S. Dhesi, A. Cavalleri, and J. P. Hill, "Melting of charge stripes in vibrationally driven La1.875Ba0.125CuO4: Assessing the respective roles of electronic and lattice order in frustrated superconductors," Phys. Rev. Lett. **112**, 157002 (2014).

34. A. Brenier and G. Boulon, "Overview of the best Yb3+-doped laser crystals," J. Alloys Compd. **323**–**324**, 210–213 (2001).

35. R. Mary, D. Choudhury, and A. K. Kar, "Applications of Fiber Lasers for the Development of Compact Photonic Devices," IEEE J. Sel. Top. Quantum Electron. **20**, (2014).

36. F. Tian, A. Ikesue, and J. Li, "Progress and perspectives on composite laser ceramics: A review," J. Eur. Ceram. Soc. **42**, 1833–1851 (2022).

37. C. J. Saraceno, "Mode-locked thin-disk lasers and their potential application for high-power terahertz generation," J. Opt. **20**, 044010 (2018).

38. T. Seifert, S. Jaiswal, U. Martens, J. Hannegan, L. Braun, P. Maldonado, F. Freimuth, A. Kronenberg, J. Henrizi, I. Radu, E. Beaurepaire, Y. Mokrousov, P. M. Oppeneer, M. Jourdan, G. Jakob, D. Turchinovich, L. M. Hayden, M. Wolf, M. Münzenberg, M. Kläui, and T. Kampfrath, "Efficient metallic spintronic emitters of ultrabroadband terahertz radiation," Nat. Photonics 2016 107 **10**, 483–488 (2016).

39. Y. Sotsuka, S. Nishimoto, T. Tsumano, K. Kawai, H. Ishise, M. Kakibuchi, R. Shimokita, T. Yamauchi, and S. I. Okihara, "The dawn of computer-assisted robotic osteotomy with ytterbium-doped fiber laser," Lasers Med. Sci. **29**, 1125–1129 (2014).

40. C. Kong, C. Pilger, H. Hachmeister, X. Wei, T. H. Cheung, C. S. W. Lai, T. Huser, K. K. Tsia, and K. K. Y. Wong, "Compact fs ytterbium fiber laser at 1010 nm for biomedical applications," Biomed. Opt. Express **8**, 4921 (2017).

41. C. Yin, S. W. Ruzzante, and J. M. Fraser, "Automated 3D bone ablation with 1,070 nm ytterbium-

doped fiber laser enabled by inline coherent imaging," Lasers Surg. Med. **48**, 288–298 (2016).

42. K. Han, Z. Lou, X. Xi, W. Cui, and C. Song, "Low-temperature properties of the ytterbium-doped fiber laser cooled by the thermoelectric cooler," Opt. Fiber Technol. **73**, 103036 (2022).

43. S. Yin, P. Yan, and M. Gong, "End-pumped 300 W continuous-wave ytterbium-doped all-fiber laser with master oscillator multi-stage power amplifiers configuration," Opt. Express **16**, 17864 (2008).

44. H. Cheng, Y. Huang, J. Weng, H. Xu, Z. Luo, Z. Cai, B. Xu, and Z. Lin, "1.06μm Q-switched ytterbium-doped fiber laser using few-layer topological insulator Bi_2Se_3 as a saturable absorber," Opt. Express, Vol. 21, Issue 24, pp. 29516-29522 **21**, 29516–29522 (2013).

45. K. Yuksel, M. Wuilpart, V. Moeyaert, and P. Mégret, "Optical frequency domain reflectometry: A review," Ict. 2009 11th Int. Conf. Transparent Opt. Networks (2009).

46. B. N. Upadhyaya, "High-power Yb-doped continuous-wave and pulsed fibre lasers," Pramana - J. Phys. **82**, 15–27 (2014).

47. "HighQ-2^{TM} Air Cooled Femtosecond Laser," https://www.spectra-physics.com/en/f/highq-2-femtosecond-laser.

48. N. M. Burford and M. O. El-Shenawee, "Review of terahertz photoconductive antenna technology," Opt. Eng. **56**, 010901 (2017).

49. P. U. Jepsen, D. G. Cooke, and M. Koch, "Terahertz spectroscopy and imaging – Modern techniques and applications," Laser Photon. Rev. **5**, 124–166 (2011).

50. M. Tani, M. Herrmann, and K. Sakai, "Generation and detection of terahertzpulsed radiation with photoconductive antennas and its application toimaging," Meas. Sci. Technol. **13**, 1739 (2002).

51. V. Pačebutas, A. Bičiūnas, S. Balakauskas, A. Krotkus, G. Andriukaitis, D. Lorenc, A. Pugžlys, and A. Baltuška, "Terahertz time-domain-spectroscopy system based on femtosecond Yb:fiber laser and GaBiAs photoconducting components," Appl. Phys. Lett. **97**, 031111 (2010).

52. R. B. Kohlhaas, S. Breuer, L. Liebermeister, S. Nellen, M. Deumer, M. Schell, M. P. Semtsiv, W. T. Masselink, and B. Globisch, "637 μW emitted terahertz power from photoconductive antennas based on rhodium doped InGaAs," Appl. Phys. Lett. **117**, 131105 (2020).

53. J. Marian, I. Bugar, D. Lorenc, V. Szöcs, and Dusan Chorvat, "Terahertz time-domain spectroscopy of selected layered silicates," Clays Clay Miner. 2009 574 **57**, 416–424 (2009).

54. E. Isgandarov, X. Ropagnol, M. Singh, and T. Ozaki, "Intense terahertz generation from photoconductive antennas," Front. Optoelectron. 2020 141 **14**, 64–93 (2021).

55. K. Yamaguchi, M. Nakajima, and T. Suemoto, "Coherent control of spin precession motion with impulsive magnetic fields of half-cycle terahertz radiation," Phys. Rev. Lett. **105**, 237201 (2010).

56. K. Maussang, J. Palomo, J. Mangeney, S. S. Dhillon, and J. Tignon, "Large-area photoconductive switches as emitters of terahertz pulses with fully electrically controlled linear polarization," Opt. Express **27**, 14784 (2019).

57. X. Ropagnol, E. Lsgandarov, X. Chai, S. M. Raeis-Zadeh, S. Safavi-Naeini, M. Reid, F. Blanchard, and T. Ozaki, "Generation of intense sub-cycle terahertz pulses with variable elliptical polarization," Appl. Phys. Lett. **120**, 171106 (2022).

58. C. Headley, L. Fu, S. Member, P. Parkinson, X. Xu, J. Lloyd-Hughes, C. Jagadish, and M. B. Johnston, "Improved Performance of GaAs-Based Terahertz Emitters via Surface Passivation and Silicon Nitride Encapsulation," IEEE J. Sel. Top. QUANTUM Electron. **1**, (2010).

59. A. Gupta, G. Rana, A. Bhattacharya, A. Singh, R. Jain, R. D. Bapat, S. P. Duttagupta, and S. S. Prabhu, "Enhanced optical-to-THz conversion efficiency of photoconductive antenna using dielectric nano-layer encapsulation," APL Photonics **3**, 051706 (2018).

60. W. Shi, L. Hou, and X. Wang, "High effective terahertz radiation from semi-insulating-GaAs photoconductive antennas with ohmic contact electrodes," J. Appl. Phys. **110**, 023111 (2011).

61. A. Singh, M. Welsch, S. Winnerl, M. Helm, M. Helm, and H. Schneider, "Non-plasmonic improvement in photoconductive THz emitters using nano- and micro-structured electrodes," Opt. Express, Vol. 28, Issue 24, pp. 35490-35497 **28**, 35490–35497 (2020).

62. L. M. Wang, "Relationship between intrinsic breakdown field and bandgap of materials," 2006 25th Int. Conf. Microelectron. MIEL 2006 - Proc. 615–618 (2006).

63. X. Ropagnol, M. Khorasaninejad, M. Raeiszadeh, S. Safavi-Naeini, M. Bouvier, C. Y. Côté, A. Laramée, M. Reid, M. A. Gauthier, and T. Ozaki, "Intense THz Pulses with large ponderomotive potential generated from large aperture photoconductive antennas," Opt. Express, Vol. 24, Issue 11, pp. 11299-11311 **24**, 11299–11311 (2016).

64. X. Ropagnol, Z. Kovács, B. Gilicze, M. Zhuldybina, F. Blanchard, C. M. Garcia-Rosas, S. Szatmári, I. B. Földes, and T. Ozaki, "Intense sub-terahertz radiation from wide-bandgap semiconductor based large-aperture photoconductive antennas pumped by UV lasers," New J. Phys. **21**, (2019).

65. H. Yoneda, K. Tokuyama, K. Ueda, H. Yamamoto, and K. Baba, "High-power terahertz radiation emitter with a diamond photoconductive switch array," Appl. Opt. **40**, 6733 (2001).

66. O. Imafuji, B. P. Singh, Y. Hirose, Y. Fukushima, and S. Takigawa, "High power subterahertz electromagnetic wave radiation from GaN photoconductive switch," Appl. Phys. Lett. **91**, 071112 (2007).

67. S. Ono, H. Murakami, A. Quema, G. Diwa, N. Sarukura, R. Nagasaka, Y. Ichikawa, H. Ogino, E. Ohshima, A. Yoshikawa, and T. Fukuda, "Generation of terahertz radiation using zinc oxide as photoconductive material excited by ultraviolet pulses," Appl. Phys. Lett. **87**, 1–3 (2005).

68. X. Ropagnol, M. Bouvier, M. Reid, and T. Ozaki, "Improvement in thermal barriers to intense terahertz generation from photoconductive antennas," J. Appl. Phys. **116**, 043107 (2014).

69. S.-G. Park, Y. Choi, Y.-J. Oh, and K.-H. Jeong, "Terahertz photoconductive antenna with metal nanoislands," Opt. Express **20**, 25530 (2012).

70. M. Bashirpour, M. Forouzmehr, S. E. Hosseininejad, M. Kolahdouz, and M. Neshat, "Improvement

of Terahertz Photoconductive Antenna using Optical Antenna Array of ZnO Nanorods," Sci. Rep. **9**, (2019).

71. O. Abdulmunem, K. Hassoon, M. Gaafar, A. Rahimi-Iman, and J. C. Balzer, "TiN Nanoparticles for Enhanced THz Generation in TDS Systems," J. Infrared, Millimeter, Terahertz Waves 2017 3810 **38**, 1206–1214 (2017).

72. W. Lai, O. Mazin Abdulmunem, P. del Pino, B. Pelaz, W. J. Parak, Q. Zhang, and H. Zhang, "Enhanced Terahertz Radiation Generation of Photoconductive Antennas Based on Manganese Ferrite Nanoparticles," Sci. Reports 2017 71 **7**, 1–7 (2017).

73. O. Abdulmunem, K. Hassoon, M. Gaafar, A. Rahimi-Iman, and J. C. Balzer, "TiN Nanoparticles for Enhanced THz Generation in TDS Systems," J. Infrared, Millimeter, Terahertz Waves **38**, 1206–1214 (2017).

74. W. Lai, O. Mazin Abdulmunem, P. Del Pino, B. Pelaz, W. J. Parak, Q. Zhang, and H. Zhang, "Enhanced Terahertz Radiation Generation of Photoconductive Antennas Based on Manganese Ferrite Nanoparticles," Sci. Rep. **7**, 1–7 (2017).

75. M. Bashirpour, M. Forouzmehr, S. E. Hosseininejad, M. Kolahdouz, and M. Neshat, "Improvement of Terahertz Photoconductive Antenna using Optical Antenna Array of ZnO Nanorods," Sci. Reports 2019 91 **9**, 1–8 (2019).

76. E. M. MODAN and A. G. PLĂIAȘU, "Advantages and Disadvantages of Chemical Methods in the Elaboration of Nanomaterials," Ann. "Dunarea Jos" Univ. Galati. Fascicle IX, Metall. Mater. Sci. **43**, 53–60 (2020).

77. P. G. Jamkhande, N. W. Ghule, A. H. Bamer, and M. G. Kalaskar, "Metal nanoparticles synthesis: An overview on methods of preparation, advantages and disadvantages, and applications," J. Drug Deliv. Sci. Technol. **53**, 101174 (2019).

78. I. Ka, V. Le Borgne, D. Ma, and M. A. El Khakani, "Pulsed Laser Ablation based Direct Synthesis of Single-Wall Carbon Nanotube/PbS Quantum Dot Nanohybrids Exhibiting Strong, Spectrally Wide and Fast Photoresponse," Adv. Mater. **24**, 6289–6294 (2012).

79. K. Trabelsi, A. Hajjaji, M. Gaidi, B. Bessais, and M. A. El Khakani, "Enhancing the photoelectrochemical response of TiO2 nanotubes through their nanodecoration by pulsed-laser-deposited Ag nanoparticles," J. Appl. Phys. **122**, 064503 (2017).

80. M. Anouar, R. Jbilat, V. Le Borgne, D. Ma, and M. A. El Khakani, "Ag nanoparticle-decorated single wall carbon nanotube films for photovoltaic applications," Mater. Renew. Sustain. Energy **5**, 1–9 (2016).

81. K. Buse, I. Breunig, J. Kiessling, and F. Fuchs, "Pump-enhanced optical parametric oscillator generating continuous wave tunable terahertz radiation," Opt. Lett. Vol. 36, Issue 22, pp. 4374-4376 **36**, 4374–4376 (2011).

82. S. Barbieri, J. Alton, S. S. Dhillon, H. E. Beere, M. Evans, E. H. Linfield, A. G. Davies, D. A. Ritchie, R. Köhler, A. Tredicucci, and F. Beltram, "Continuous-wave operation of terahertz

quantum-cascade lasers," IEEE J. Quantum Electron. **39**, 586–591 (2003).

83. N. T. Yardimci, S. H. Yang, C. W. Berry, and M. Jarrahi, "High-power terahertz generation using large-area plasmonic photoconductive emitters," IEEE Trans. Terahertz Sci. Technol. **5**, 223–229 (2015).

84. R. Safian, G. Ghazi, and N. Mohammadian, "Review of photomixing continuous-wave terahertz systems and current application trends in terahertz domain," https://doi.org/10.1117/1.OE.58.11.110901 **58**, 110901 (2019).

85. P. Tan, J. Huang, K. F. Liu, Y. Q. Xiong, and M. W. Fan, "Terahertz radiation sources based on free electron lasers and their applications," Sci. China Inf. Sci. 2012 551 **55**, 1–15 (2011).

86. K. Reimann, "Table-top sources of ultrashort THz pulses," Reports Prog. Phys. **70**, 1597 (2007).

87. D. M. Mittleman, "Frontiers in terahertz sources and plasmonics," Nat. Photonics 2013 79 **7**, 666–669 (2013).

88. A. Rice, Y. Jin, X. F. Ma, X. C. Zhang, D. Bliss, J. Larkin, and M. Alexander, "Terahertz optical rectification from 〈110〉 zinc-blende crystals," Appl. Phys. Lett. **64**, 1324 (1998).

89. P. Gu and M. Tani, "Terahertz radiation from semiconductor surfaces," Top. Appl. Phys. **97**, 63–98 (2005).

90. B. Bartal, J. Hebling, K.-L. Yeh, K. A. Nelson, and M. C. Hoffmann, "Generation of high-power terahertz pulses by tilted-pulse-front excitation and their application possibilities," JOSA B, Vol. 25, Issue 7, pp. B6-B19 **25**, B6–B19 (2008).

91. T. Ozaki, F. Blanchard, G. Sharma, L. Razzari, X. Ropagnol, F. Vidal, R. Morandotti, J. C. Kieffer, M. Reid, and F. Hegmann, "THz imaging and spectroscopy using intense THz sources at the advanced laser light source," Phys. Procedia **5**, 119–124 (2010).

92. J. A. Fülöp, T. Balciunas, A. Baltuska, B. Monoszlai, A. Pugzlys, G. Arthur, G. Andriukaitis, J. Hebling, and G. Polónyi, "Highly efficient scalable monolithic semiconductor terahertz pulse source," Opt. Vol. 3, Issue 10, pp. 1075-1078 **3**, 1075–1078 (2016).

93. Q. Tian, Q. Tian, H. Xu, H. Xu, Y. Wang, Y. Wang, Y. Liang, Y. Liang, Y. Tan, Y. Tan, X. Ning, X. Ning, L. Yan, L. Yan, Y. Du, Y. Du, R. Li, R. Li, J. Hua, J. Hua, W. Huang, W. Huang, C. Tang, and C. Tang, "Efficient generation of a high-field terahertz pulse train in bulk lithium niobate crystals by optical rectification," Opt. Express, Vol. 29, Issue 6, pp. 9624-9634 **29**, 9624–9634 (2021).

94. L. Guiramand, J. E. Nkeck, X. Ropagnol, X. Ropagnol, T. Ozaki, and F. Blanchard, "Near-optimal intense and powerful terahertz source by optical rectification in lithium niobate crystal," Photonics Res. Vol. 10, Issue 2, pp. 340-346 **10**, 340–346 (2022).

95. X. Ropagnol, M. Matoba, J. E. Nkeck, F. Blanchard, E. Isgandarov, J. Yumoto, and T. Ozaki, "Efficient terahertz generation and detection in cadmium telluride using ultrafast ytterbium laser," Appl. Phys. Lett. **117**, 181101 (2020).

96. M. Jazbinsek, U. Puc, A. Abina, and A. Zidansek, "Organic Crystals for THz Photonics," Appl. Sci. **9**, 882 (2019).

97. M. Jazbinsek, U. Puc, A. Abina, and A. Zidansek, "Organic Crystals for THz Photonics," Appl. Sci. **9**, 882 (2019).

98. J. Hebling, A. G. Stepanov, G. Almási, B. Bartal, and J. Kuhl, "Tunable THz pulse generation by optical rectification of ultrashort laser pulses with tilted pulse fronts," Appl. Phys. B 2004 785 **78**, 593–599 (2004).

99. M. Shalaby, C. Vicario, K. Thirupugalmani, S. Brahadeeswaran, and C. P. Hauri, "Intense THz source based on BNA organic crystal pumped at Ti:sapphire wavelength," Opt. Lett. **41**, 1777 (2016).

100. H. Zhao, Y. Tan, T. Wu, G. Steinfeld, Y. Zhang, C. Zhang, L. Zhang, and M. Shalaby, "Efficient broadband terahertz generation from organic crystal BNA using near infrared pump," Appl. Phys. Lett. **114**, 241101 (2019).

101. I. C. Tangen, G. A. Valdivida-Berroeta, L. K. Heki, Z. B. Zaccardi, E. W. Jackson, C. B. Bahr, D. J. Michaelis, and J. A. Johnson, "Comprehensive Characterization of Terahertz Generation with the Organic Crystal BNA," arXiv (2020).

102. F. Roeder, M. Shalaby, B. Beleites, F. Ronneberger, and A. Gopal, "THz generation by optical rectification of intense near-infrared pulses in organic crystal BNA," Opt. Express **28**, 36274 (2020).

103. Z. B. Zaccardi, Z. B. Zaccardi, I. C. Tangen, I. C. Tangen, G. A. Valdivia-Berroeta, C. B. Bahr, K. C. Kenney, C. Rader, M. J. Lutz, B. P. Hunter, D. J. Michaelis, D. J. Michaelis, J. A. Johnson, and J. A. Johnson, "Enabling high-power, broadband THz generation with 800-nm pump wavelength," Opt. Express, Vol. 29, Issue 23, pp. 38084-38094 **29**, 38084–38094 (2021).

104. S. Mansourzadeh, T. Vogel, M. Shalaby, F. Wulf, and C. J. Saraceno, "Milliwatt average power, MHz-repetition rate, broadband THz generation in organic crystal BNA with diamond substrate," Opt. Express **29**, (2021).

105. H. Hamster, A. Sullivan, S. Gordon, W. White, and R. W. Falcone, "Subpicosecond, electromagnetic pulses from intense laser-plasma interaction," Phys. Rev. Lett. **71**, 2725 (1993).

106. T. Löffler, M. Kress, M. Thomson, and H. G. Roskos, "Efficient Terahertz Pulse Generation in Laser-Induced Gas Plasmas," AcPPA **107**, 99 (2005).

107. K. Y. Kim, J. H. Glownia, A. J. Taylor, G. Rodriguez, W. P. Leemans, C. G. R. Geddes, J. Faure, C. Tóth, J. Van Tilborg, C. B. Schroeder, E. Esarey, G. Fubiani, D. Auerbach, B. Marcelis, M. A. Carnahan, R. A. Kaindl, J. Byrd, and M. C. Martin, "Terahertz emission from ultrafast ionizing air in symmetry-broken laser fields," Opt. Express, Vol. 15, Issue 8, pp. 4577-4584 **15**, 4577–4584 (2007).

108. K. Y. Kim, J. H. Glownia, A. J. Taylor, and G. Rodriguez, "High-power broadband terahertz generation via two-color photoionization in gases," IEEE J. Quantum Electron. **48**, 797–805 (2012).

109. M. D. Thomson, M. Kreß, T. Löffler, and H. G. Roskos, "Broadband THz emission from gas plasmas induced by femtosecond optical pulses: From fundamentals to applications," Laser Photon. Rev. **1**, 349–368 (2007).

110. H. Zhong, N. Karpowicz, and X. C. Zhang, "Terahertz emission profile from laser-induced air plasma," Appl. Phys. Lett. **88**, 261103 (2006).

111. A. D. Koulouklidis, C. Gollner, V. Shumakova, V. Y. Fedorov, A. Pugžlys, A. Baltuška, and S. Tzortzakis, "Observation of extremely efficient terahertz generation from mid-infrared two-color laser filaments," Nat. Commun. 2020 111 **11**, 1–8 (2020).

112. C. Tailliez, X. Davoine, A. Debayle, L. Gremillet, and L. Bergé, "Terahertz Pulse Generation by Strongly Magnetized, Laser-Created Plasmas," Phys. Rev. Lett. **128**, 174802 (2022).

113. E. Isgandarov, X. Ropagnol, M. Singh, and T. Ozaki, "Intense terahertz generation from photoconductive antennas," Front. Optoelectron. 2020 141 **14**, 64–93 (2021).

114. D. H. Auston, K. P. Cheung, and P. R. Smith, "Picosecond photoconducting Hertzian dipoles," Appl. Phys. Lett. **45**, 284–286 (1984).

115. S. H. Yang, M. R. Hashemi, C. W. Berry, and M. Jarrahi, "7.5% Optical-to-terahertz conversion efficiency offered by photoconductive emitters with three-dimensional plasmonic contact electrodes," IEEE Trans. Terahertz Sci. Technol. **4**, 575–581 (2014).

116. D. You, D. R. Dykaar, R. R. Jones, and P. H. Bucksbaum, "Generation of high-power sub-single-cycle 500-fs electromagnetic pulses," Opt. Lett. **18**, 290 (1993).

117. J. T. Darrow, X. C. Zhang, D. H. Auston, and J. D. Morse, "Saturation Properties of Large-Aperture Photoconducting Antennas," IEEE J. Quantum Electron. **28**, 1607–1616 (1992).

118. J. Prajapati, M. Bharadwaj, A. Chatterjee, and R. Bhattacharjee, "Magnetic Field-Assisted Radiation Enhancement from a Large Aperture Photoconductive Antenna," in *IEEE Transactions on Microwave Theory and Techniques* (Institute of Electrical and Electronics Engineers Inc., 2018), Vol. 66, pp. 678–687.

119. L. Hou, W. Shi, and S. Chen, "Noise analysis and optimization of terahertz photoconductive emitters," IEEE J. Sel. Top. Quantum Electron. **19**, (2013).

120. E. Moreno, M. F. Pantoja, F. G. Ruiz, J. B. Roldán, and S. G. García, "On the numerical modeling of terahertz photoconductive antennas," J. Infrared, Millimeter, Terahertz Waves **35**, 432–444 (2014).

121. E. Castro-Camus, L. Fu, J. Lloyd-Hughes, H. H. Tan, C. Jagadish, and M. B. Johnston, "Photoconductive response correction for detectors of terahertz radiation," J. Appl. Phys. **104**, (2008).

122. M. Tani, S. Matsuura, K. Sakai, and S. Nakashima, "Emission characteristics of photoconductive antennas based on low-temperature-grown GaAs and semi-insulating GaAs," Appl. Opt. **36**, 7853 (1997).

123. S. G. Park, A. M. Weiner, M. R. Melloch, C. W. Siders, J. L. W. Siders, and A. J. Taylor, "High-power narrow-band terahertz generation using large-aperture photoconductors," IEEE J. Quantum Electron. **35**, 1257–1268 (1999).

124. A. J. Taylor, P. K. Benicewicz, and S. M. Young, "Modeling of femtosecond electromagnetic pulses from large-aperture photoconductors.," Opt. Lett. **18**, 1340 (1993).

125. L. Duvillaret, F. Garet, J. F. Roux, and J. L. Coutaz, "Analytical modeling and optimization of terahertz time-domain spectroscopy experiments using photoswitches as antennas," IEEE J. Sel. Top. Quantum Electron. **7**, 615–623 (2001).

126. E. Castro-Camus, J. Lloyd-Hughes, and M. B. Johnston, "Three-dimensional carrier-dynamics simulation of terahertz emission from photoconductive switches," Phys. Rev. B - Condens. Matter Mater. Phys. **71**, 195301 (2005).

127. J. Prajapati, M. Bharadwaj, A. Chatterjee, and R. Bhattacharjee, "Radiation field analysis of a photoconductive antenna using an improved carrier dynamics," Semicond. Sci. Technol. **34**, 24004 (2019).

128. Z. Piao, M. Tani, and K. Sakai, "Carrier dynamics and terahertz radiation in photoconductive antennas," Japanese J. Appl. Physics, Part 1 Regul. Pap. Short Notes Rev. Pap. **39**, 96–100 (2000).

129. S. Winnerl, F. Peter, S. Nitsche, A. Dreyhaupt, B. Zimmermann, M. Wagner, H. Schneider, M. Helm, and K. Köhler, "Generation and detection of THz radiation with scalable antennas based on GaAs substrates with different carrier lifetimes," IEEE J. Sel. Top. Quantum Electron. **14**, 449–457 (2008).

130. W. Shi, X. F. Sun, J. Zeng, and W. L. Jia, "Carrier dynamics and terahertz radiation in large-aperture photoconductive antenna," in *International Symposium on Photoelectronic Detection and Imaging 2007: Laser, Ultraviolet, and Terahertz Technology*, L. Zhou, ed. (SPIE, 2007), Vol. 6622, p. 662228.

131. D. Liu and J. Qin, "Carrier dynamics of terahertz emission from low-temperature-grown GaAs," Appl. Opt. **42**, 3678 (2003).

132. "Carrier dynamics and THz radiation in biased semiconductor structures | (1999) | Piao | Publications | Spie," https://spie.org/Publications/Proceedings/Paper/10.1117/12.347130?SSO=1.

133. X. Ropagnol, R. Morandotti, T. Ozaki, and M. Reid, "THz pulse shaping and improved optical-to-THz conversion efficiency using a binary phase mask," Opt. Lett. **36**, 2662 (2011).

134. L. Chen and W. Fan, "Numerical simulation of terahertz generation and detection based on ultrafast photoconductive antennas," in *International Symposium on Photoelectronic Detection and Imaging 2011: Terahertz Wave Technologies and Applications* (SPIE, 2011), Vol. 8195, p. 81950K.

135. G. Šlekas, Kancleris, A. Urbanowicz, and R. Čiegis, "Comparison of full-wave models of terahertz photoconductive antenna based on ordinary differential equation and Monte Carlo method," Eur. Phys. J. Plus **135**, 85 (2020).

136. B. Cadilhon, B. Cassany, P. Modin, J.-C. Diot, V. Bertrand, and L. Pecastaing, "Ultra Wideband Antennas for High Pulsed Power Applications," in *Ultra Wideband Communications: Novel Trends - Antennas and Propagation* (InTech, 2011).

137. S. Mahadevan, S. M. Hardas, and G. Suryan, "Electrical breakdown in semiconductors," Phys. Status Solidi **8**, 335–374 (1971).

138. M. Xu, M. Li, W. Shi, C. Ma, Q. Zhang, L. Fan, X. Shang, and P. Xue, "Temperature-Dependence of High-Gain Operation in GaAs Photoconductive Semiconductor Switch at 1.6 μj Excitation," IEEE Electron Device Lett. **37**, 67–69 (2016).

139. S. B. Qadri, D. H. Wu, B. D. Graber, N. A. Mahadik, and A. Garzarella, "Failure mechanism of THz GaAs photoconductive antenna," Appl. Phys. Lett. **101**, (2012).

140. C. Sun and A. Zhang, "Efficient terahertz generation from lightly ion-beam-treated semi-insulating GaAs photoconductive antennas," Appl. Phys. Express **10**, 102202 (2017).

141. S. Gupta, M. Y. Frankel, J. A. Valdmanis, J. F. Whitaker, G. A. Mourou, F. W. Smith, and A. R. Calawa, "Subpicosecond carrier lifetime in GaAs grown by molecular beam epitaxy at low temperatures," Appl. Phys. Lett. **59**, 3276–3278 (1991).

142. T. A. Liu, M. Tani, M. Nakajima, M. Hangyo, and C. L. Pan, "Ultrabroadband terahertz field detection by photoconductive antennas based on multi-energy arsenic-ion-implanted GaAs and semi-insulating GaAs," Appl. Phys. Lett. **83**, 1322–1324 (2003).

143. "B. Salem, D. Morris, V. Aimez, J. Beerens, J. Beauvais,... - Google Scholar," https://scholar.google.com/scholar?hl=en&as_sdt=0%2C5&sciodt=0%2C5&cites=4990333125295951852&scipsc=&q=B.+Salem%2C+D.+Morris%2C+V.+Aimez%2C+J.+Beerens%2C+J.+Beauvais%2C+D.+Houde+“Pulsed+photoconductive+antenna+terahertz+sources+made+on+ion-implanted+GaAs+substrate”+J.+Phys.+Condens.+Natter%2C+17+7327+%282005%29&btnG=.

144. B. Salem, D. Morris, Y. Salissou, V. Aimez, S. Charlebois, M. Chicoine, and F. Schiettekatte, "Terahertz emission properties of arsenic and oxygen ion-implanted GaAs based photoconductive pulsed sources," J. Vac. Sci. Technol. A Vacuum, Surfaces, Film. **24**, 774–777 (2006).

145. B. Singh, O. Imafuji, … Y. H.-2007 J. 32nd, and undefined 2007, "High power C-doped GaN photoconductive THz emitter," ieeexplore.ieee.org (n.d.).

146. M. Beck, H. Schäfer, G. Klatt, J. Demsar, S. Winnerl, M. Helm, and T. Dekorsy, "Impulsive terahertz radiation with high electric fields from an amplifier-driven large-area photoconductive antenna," Opt. Express **18**, 9251 (2010).

147. E. M. Gavrushchuk, "Polycrystalline zinc selenide for IR optical applications," Inorg. Mater. **39**, 883–899 (2003).

148. P. S. Cho, F. Peng, P.-T. Ho, J. Goldhar, and Chi H. Lee, "ZnSe photoconductive switches with transparent electrodes," in (Institute of Electrical and Electronics Engineers (IEEE), 2005), pp. 209–212.

149. P. T. Ho, F. Peng, and J. Goldhar, "Photoconductive Switching using Polycrystalline ZnSe," IEEE Trans. Electron Devices **37**, 2517–2519 (1990).

150. P. S. Cho, J. Goldhar, C. H. Lee, S. E. Saddow, and P. Neudeck, "Photoconductive and photovoltaic response of high-dark-resistivity 6H-SiC devices," J. Appl. Phys. **77**, 1591–1599 (1995).

151. J. F. Holzman and A. Y. Elezzabi, "Two-photon photoconductive terahertz generation in ZnSe," Appl. Phys. Lett. **83**, 2967–2969 (2003).

152. X. Ropagnol, R. Morandotti, T. Ozaki, and M. Reid, "Toward high-power terahertz emitters using large aperture ZnSe photoconductive antennas," IEEE Photonics J. **3**, 174–186 (2011).

153. D. Mauch, W. Sullivan, A. Bullick, A. Neuber, and J. Dickens, "High Power Lateral Silicon Carbide Photoconductive Semiconductor Switches and Investigation of Degradation Mechanisms," IEEE Trans. Plasma Sci. **43**, 2021–2031 (2015).

154. H. Shimizu, N. Watanabe, T. Morikawa, A. Shima, and N. Iwamuro, "1.2 kV silicon carbide Schottky barrier diode embedded MOSFETs with extension structure and titanium-based single contact," Jpn. J. Appl. Phys. **59**, 026502 (2020).

155. T. Kimoto and Y. Yonezawa, "Current status and perspectives of ultrahigh-voltage SiC power devices," Mater. Sci. Semicond. Process. **78**, 43–56 (2018).

156. A. Bhalla, "Status of SiC Products and Technology," in *Disruptive Wide Bandgap Semiconductors, Related Technologies, and Their Applications* (InTech, 2018).

157. L. Xiao, X. Yang, P. Duan, H. Xu, X. Chen, X. Hu, Y. Peng, and X. Xu, "Effect of electron avalanche breakdown on a high-purity semi-insulating 4H-SiC photoconductive semiconductor switch under intrinsic absorption," Appl. Opt. **57**, 2804 (2018).

158. D. Yu, J. Kang, J. Berakdar, and C. Jia, "Nondestructive ultrafast steering of a magnetic vortex by terahertz pulses," NPG Asia Mater. **12**, 1–8 (2020).

159. D. Elliott, *Ultraviolet Laser Technology and Applications* (2014).

160. F. Duarte, *Tunable Lasers Handbook* (1996).

161. S. Szatmári, B. Rácz, and F. P. Schäffer, "Bandwidth limited amplification of 220 fs pulses in XeCl," Opt. Commun. **62**, 271–276 (1987).

162. B. Dick, S. Szatmári, B. Rácz, and F. P. Schäfer, "Bandwidth limited amplification of 220 fs pulses in XeCl: Theoretical and experimental study of temporal and spectral behavior," Opt. Commun. **62**, 277–283 (1987).

163. S. Szatmári, F. P. Schäfer, E. Müller-Horsche, and W. Müchenheim, "Hybrid dye-excimer laser system for the generation of 80 fs, 900 GW pulses at 248 nm," Opt. Commun. **63**, 305–309 (1987).

164. Di. Ghindani, A. Bhattacharya, S. Samad, B. Nayak, A. P. Shah, A. A. Rahman, A. Bhattacharya, and S. S. Prabhu, "Towards Bandwidth-enhanced GaN-based Terahertz Photoconductive Antennas," in *International Conference on Infrared, Millimeter, and Terahertz Waves, IRMMW-*

THz (IEEE Computer Society, 2019), Vol. 2019-September.

165. X. Ropagnol, Z. Kovács, B. Gilicze, M. Zhuldybina, F. Blanchard, C. M. Garcia-Rosas, S. Szatmári, I. B. Földes, and T. Ozaki, "Intense sub-terahertz radiation from wide-bandgap semiconductor based large-aperture photoconductive antennas pumped by UV lasers," New J. Phys **21**, 113042 (2019).

166. S. Szatmári, "High-brightness ultraviolet excimer lasers," Appl. Phys. B Laser Opt. **58**, 211–223 (1994).

167. G. C. Loata, M. D. Thomson, T. Löffler, and H. G. Roskos, "Radiation field screening in photoconductive antennae studied via pulsed terahertz emission spectroscopy," Appl. Phys. Lett. **91**, 232506 (2007).

168. E. Budiarto, J. Margolies, S. Jeong, J. Son, and J. Bokor, "High-intensity terahertz pulses at 1-kHz repetition rate," IEEE J. Quantum Electron. **32**, 1839–1846 (1996).

169. G. H. Welsh, D. A. Turton, D. R. Jones, D. A. Jaroszynski, and K. Wynne, "200 ns pulse high-voltage supply for terahertz field emission," Rev. Sci. Instrum. **78**, 043103 (2007).

170. S. Winnerl, B. Zimmermann, F. Peter, H. Schneider, and M. Helm, "Terahertz Bessel-Gauss beams of radial and azimuthal polarization from microstructured photoconductive antennas," Opt. Express **17**, 1571 (2009).

171. M. J. Cliffe, A. Rodak, D. M. Graham, and S. P. Jamison, "Generation of longitudinally polarized terahertz pulses with field amplitudes exceeding 2 kV/cm," Appl. Phys. Lett. **105**, (2014).

172. C.-H. Editors: Mourou, Gerard A., Bloom, David M., Lee, "Picosecond Electronics and Optoelectronics," https://www.google.com/search?q=Picosecond+Optoelectronics%2C+Gerard+Mourou%2C+Editor%2C+Proc.+SPIE+439%2C+pp&oq=Picosecond+Optoelectronics%2C+Gerard+Mourou%2C+Editor%2C+Proc.+SPIE+439%2C+pp&aqs=chrome.0.69i59j69i60.484j0j4&sourceid=chrome&ie=UTF-8.

173. C. C. III, V. Diadiuk, I. Y.-… Optoelectronics, and undefined 1983, "InP optoelectronic switches and their high-speed signal-processiny applications," spiedigitallibrary.org (n.d.).

174. T. Hattori, K. Egawa, S. I. Ookuma, and T. Itatani, "Intense terahertz pulses from large-aperture antenna with interdigitated electrodes," Japanese J. Appl. Physics, Part 2 Lett. **45**, L422 (2006).

175. S. Y. Chou, Y. Liu, and P. B. Fischer, "Tera-hertz GaAs metal-semiconductor-metal photodetectors with 25 nm finger spacing and finger width," Appl. Phys. Lett. **61**, 477–479 (1992).

176. M. Awad, M. Nagel, H. Kurz, J. Herfort, and K. Ploog, "Characterization of low temperature GaAs antenna array terahertz emitters," Appl. Phys. Lett. **91**, 181124 (2007).

177. G. Acuna, F. Buersgens, … C. L.-E., and undefined 2008, "Interdigitated terahertz emitters," ieeexplore.ieee.org (n.d.).

178. X. Ropagnol, F. Blanchard, T. Ozaki, and M. Reid, "Intense terahertz generation at low frequencies using an interdigitated ZnSe large aperture photoconductive antenna," Appl. Phys. Lett. **103**, 161108

(2013).

179. A. Dreyhaupt, S. Winnerl, T. Dekorsy, and M. Helm, "High-intensity terahertz radiation from a microstructured large-area photoconductor," Appl. Phys. Lett. **86**, 1–3 (2005).

180. D. B. Go and D. A. Pohlman, "A mathematical model of the modified Paschen's curve for breakdown in microscale gaps," J. Appl. Phys. **107**, 103303 (2010).

181. P. Kirawanich, S. J. Yakura, and N. E. Islam, "Study of high-power wideband terahertz-pulse generation using integrated high-speed photoconductive semiconductor switches," IEEE Trans. Plasma Sci. **37**, 219–228 (2009).

182. A. Singh, M. Welsch, S. Winnerl, M. Helm, and H. Schneider, "Improved electrode design for interdigitated large-area photoconductive terahertz emitters," Opt. Express **27**, 13108 (2019).

183. X. Ropagnol, X. Chai, S. M. Raeis-Zadeh, S. Safavi-Naeini, M. Kirouac-Turmel, M. Bouvier, C. Y. Cote, M. Reid, M. A. Gauthier, and T. Ozaki, "Influence of gap size on intense THz generation from ZnSe interdigitated large aperture photoconductive antennas (October 2016)," IEEE J. Sel. Top. Quantum Electron. **23**, (2017).

184. C. W. Berry and M. Jarrahi, "Principles of impedance matching in photoconductive antennas," J. Infrared, Millimeter, Terahertz Waves **33**, 1182–1189 (2012).

185. R. Emadi, R. Safian, and A. Z. Nezhad, "Theoretical modeling of terahertz pulsed photoconductive antennas based on hot-carriers effect," IEEE J. Sel. Top. Quantum Electron. **23**, (2017).

186. E. R. Brown, K. A. McIntosh, F. W. Smith, K. B. Nichols, M. J. Manfra, C. L. Dennis, and J. P. Mattia, "Milliwatt output levels and superquadratic bias dependence in a low-temperature-grown GaAs photomixer," Appl. Phys. Lett. **64**, 3311–3313 (1994).

187. X. Ropagnol, F. Blanchard, T. Ozaki, and M. Reid, "Intense terahertz generation at low frequencies using an interdigitated ZnSe large aperture photoconductive antenna," Appl. Phys. Lett. **103**, (2013).

188. D. R. Bacon, T. B. Gill, M. Rosamond, A. D. Burnett, A. Dunn, L. Li, E. H. Linfield, A. G. Davies, P. Dean, and J. R. Freeman, "Photoconductive arrays on insulating substrates for high-field terahertz generation," Opt. Express **28**, 17219 (2020).

189. D. S. Kim and D. S. Citrin, "Coulomb and radiation screening in photoconductive terahertz sources," Appl. Phys. Lett. **88**, 161117 (2006).

190. A. Dreyhaupt, F. Peter, S. Winnerl, S. Nitsche, M. Wagner, H. Schneider, M. Helm, and K. Köhler, "Leistungsstarke Emitter und einfach handhabbare Detektoren für die Terahertz-Time-Domain-Spektroskopie," Tech. Mess. **75**, 3–13 (2008).

191. S. Winnerl, "Scalable microstructured photoconductive terahertz emitters," J. Infrared, Millimeter, Terahertz Waves **33**, 431–454 (2012).

192. G. Matthäus, S. Nolte, R. Hohmuth, M. Voitsch, W. Richter, B. Pradarutti, S. Riehemann, G. Notni, and A. Tünnermann, "Large-area microlens emitters for powerful THz emission," Appl. Phys. B Lasers Opt. **96**, 233–235 (2009).

193. A. Singh and S. S. Prabhu, "Microlensless interdigitated photoconductive terahertz emitters," Opt. Express **23**, 1529 (2015).

194. D. R. Bacon, T. B. Gill, M. Rosamond, A. D. Burnett, A. Dunn, L. Li, E. H. Linfield, A. G. Davies, P. Dean, and J. R. Freeman, "Photoconductive arrays on insulating substrates for high-field terahertz generation," Opt. Express **28**, 17219 (2020).

195. D. R. Bacon, T. B. Gill, M. Rosamond, A. D. Burnett, A. Dunn, L. Li, E. H. Linfield, A. G. Davies, P. Dean, and J. R. Freeman, "Photoconductive arrays on insulating substrates for high-field terahertz generation," Opt. Express **28**, 17219 (2020).

196. A. Singh, S. Winnerl, J. C. König-Otto, D. R. Stephan, M. Helm, and H. Schneider, "Plasmonic efficiency enhancement at the anode of strip line photoconductive terahertz emitters," Opt. Express **24**, 22628 (2016).

197. X. C. Zhang, "Generation and detection of terahertz electromagnetic pulses from semiconductors with femtosecond optics," J. Lumin. **66**–**67**, 488–492 (1995).

198. S. Preu, G. H. Dhler, S. Malzer, L. J. Wang, and A. C. Gossard, "Tunable, continuous-wave Terahertz photomixer sources and applications," J. Appl. Phys. **109**, 61301 (2011).

199. P. J. Hale, J. Madeo, C. Chin, S. S. Dhillon, J. Mangeney, J. Tignon, and K. M. Dani, "20 THz broadband generation using semi-insulating GaAs interdigitated photoconductive antennas," Opt. Express **22**, 26358 (2014).

200. J. Madéo, N. Jukam, D. Oustinov, M. Rosticher, R. Rungsawang, J. Tignon, and S. S. Dhillon, "Frequency tunable terahertz interdigitated photoconductive antennas," Electron. Lett. **46**, 611–613 (2010).

201. X. Ropagnol, M. Khorasaninejad, M. Raeiszadeh, S. Safavi-Naeini, M. Bouvier, C. Y. Côté, A. Laramée, M. Reid, M. A. Gauthier, and T. Ozaki, "Intense THz Pulses with large ponderomotive potential generated from large aperture photoconductive antennas," Opt. Express **24**, 11299 (2016).

202. L. A. Sterczewski, M. P. Grzelczak, and E. F. Plinski, "Terahertz antenna electronic chopper," Rev. Sci. Instrum. **87**, (2016).

203. H. Hirori, A. Doi, F. Blanchard, and K. Tanaka, "Single-cycle terahertz pulses with amplitudes exceeding 1 MV/cm generated by optical rectification in LiNbO3," Appl. Phys. Lett. **98**, 091106 (2011).

204. E. Moreno, M. F. Pantoja, F. G. Ruiz, J. B. Roldán, and S. G. García, "On the numerical modeling of terahertz photoconductive antennas," J. Infrared, Millimeter, Terahertz Waves **35**, 432–444 (2014).

205. . D Auston, K. Cheung, J. Valdmanis, D. Kleinman ; M. Mittleman, M. Gupta, R. Neelamani, R. G. Baraniuk, J. V Rudd, and M. Koch, "Nanoplasmonics enhanced terahertz sources," Opt. Express, Vol. 22, Issue 23, pp. 27992-28001 **22**, 27992–28001 (2014).

206. M. van Exter, C. Fattinger, and D. Grischkowsky, "Terahertz time-domain spectroscopy of water

vapor," Opt. Lett. **14**, 1128 (1989).

207. D. Grischkowsky, S. Keiding, M. van Exter, and C. Fattinger, "Far-infrared time-domain spectroscopy with terahertz beams of dielectrics and semiconductors," J. Opt. Soc. Am. B **7**, 2006 (1990).

208. P. U. Jepsen, R. H. Jacobsen, and S. R. Keiding, "Generation and detection of terahertz pulses from biased semiconductor antennas," JOSA B, Vol. 13, Issue 11, pp. 2424-2436 **13**, 2424–2436 (1996).

209. T. A. Liu, M. Tani, M. Nakajima, M. Hangyo, and C. L. Pan, "Ultrabroadband terahertz field detection by photoconductive antennas based on multi-energy arsenic-ion-implanted GaAs and semi-insulating GaAs," Appl. Phys. Lett. **83**, 1322 (2003).

210. T.-A. Liu, M. Tani, M. Nakajima, M. Hangyo, K. Sakai, C.-L. Pan, P. Gu, M. Tani, K. Sakai, and T.-R. Yang, "Ultrabroadband terahertz field detection by proton-bombarded InP photoconductive antennas," Opt. Express, Vol. 12, Issue 13, pp. 2954-2959 **12**, 2954–2959 (2004).

211. N. Karpowicz, J. Dai, X. Lu, Y. Chen, M. Yamaguchi, H. Zhao, X. C. Zhang, L. Zhang, C. Zhang, M. Price-Gallagher, C. Fletcher, O. Mamer, A. Lesimple, and K. Johnson, "Coherent heterodyne time-domain spectrometry covering the entire "terahertz gap,"" Appl. Phys. Lett. **92**, 011131 (2008).

212. J. Dai, X. Xie, and X. C. Zhang, "Detection of broadband terahertz waves with a laser-induced plasma in gases," Phys. Rev. Lett. **97**, 103903 (2006).

213. C. Gollner, H. Lee, X. Jiaqi, C. Weber, E. Sollinger, V. Stummer, A. Baltuska, Y. Zhang, A. Pugzlys, and M. Shalaby, "Efficient Broadband Terahertz Generation in BNA Organic Crystals at Ytterbium Laser Wavelength," Int. Conf. Infrared, Millimeter, Terahertz Waves, IRMMW-THz **2020-November**, 898–899 (2020).

214. I. C. Tangen, G. A. Valdivida-Berroeta, L. K. Heki, Z. B. Zaccardi, E. W. Jackson, C. B. Bahr, D. J. Michaelis, and J. A. Johnson, "Comprehensive Characterization of Terahertz Generation with the Organic Crystal BNA," arXiv (2020).

215. K. Miyamoto, S. Ohno, M. Fujiwara, H. Minamide, H. Hashimoto, and H. Ito, "Optimized terahertz-wave generation using BNA-DFG," Opt. Express **17**, 14832 (2009).

216. C. J. Saraceno, F. Wulf, M. Shalaby, S. Mansourzadeh, and T. Vogel, "Milliwatt average power, MHz-repetition rate, broadband THz generation in organic crystal BNA with diamond substrate," Opt. Express, Vol. 29, Issue 24, pp. 38946-38957 **29**, 38946–38957 (2021).

217. J. Xu, B. Globisch, C. Hofer, N. Lilienfein, T. Butler, N. Karpowicz, and I. Pupeza, "Three-octave terahertz pulses from optical rectification of 20 fs, 1 μm, 78 MHz pulses in GaP," J. Phys. B At. Mol. Opt. Phys. **51**, 154002 (2018).

218. X. Ropagnol, E. Lsgandarov, X. Chai, S. M. Raeis-Zadeh, S. Safavi-Naeini, M. Reid, F. Blanchard, and T. Ozaki, "Generation of intense sub-cycle terahertz pulses with variable elliptical polarization," Appl. Phys. Lett. **120**, 171106 (2022).

219. J. Lu, Y. Zhang, H. Y. Hwang, B. K. Ofori-Okai, S. Fleischer, and K. A. Nelson, "Two-dimensional

Terahertz Photon Echo and Rotational Spectroscopy in the Gas Phase," Int. Conf. Ultrafast Phenom. (2016), Pap. UTu1A.6 UTu1A.6 (2016).

220. Q. Rehman, A. D. Khan, A. D. Khan, M. Noman, H. Ali, A. Rauf, and M. S. Ahmad, "Super absorption of solar energy using a plasmonic nanoparticle based CdTe solar cell," RSC Adv. **9**, 34207–34213 (2019).

221. S. R. Kavanagh, A. Walsh, and D. O. Scanlon, "Rapid Recombination by Cadmium Vacancies in CdTe," ACS Energy Lett. **6**, 1392–1398 (2021).

222. L. F. Champagne, F. O'Neill, and W. T. Whitney, "A large aperture CdTe pockels cell for CO2 lasers," Opt. Commun. **13**, 282–285 (1975).

223. K. Becker, J. B. Johnson, and G. Edwards, "Broadband Pockels cell and driver for a Mark III-type free electron laser," Rev. Sci. Instrum. **65**, 1496 (1998).

224. Z. Tsybrii, M. Vuichyk, K. Svezhentsova, M. Smolii, Y. Gomeniuk, A. Nazarov, and F. Sizov, "Low-temperature growth of CdTe thin films as passivation layers for IR and THz functional elements," Mater. Chem. Phys. **278**, 125581 (2022).

225. R. O. Bell, G. Entine, and H. B. Serreze, "Time-dependent polarization of CdTe gamma-ray detectors," Nucl. Instruments Methods **117**, 267–271 (1974).

226. Y. Eisen and A. Shor, "CdTe and CdZnTe materials for room-temperature X-ray and gamma ray detectors," J. Cryst. Growth **184**–**185**, 1302–1312 (1998).

227. Y. Eisen, A. Shor, and I. Mardor, "CdTe and CdZnTe X-ray and gamma-ray detectors for imaging systems," IEEE Trans. Nucl. Sci. **51**, 1191–1198 (2004).

228. A. Rice, Y. Jin, X. F. Ma, X. C. Zhang, D. Bliss, J. Larkin, and M. Alexander, "Terahertz optical rectification from 〈110〉 zinc-blende crystals," Appl. Phys. Lett. **64**, 1324 (1998).

229. A. Kumari, M. Venkatesh, and A. K. Chaudhary, "Terahertz generation from Cadmium Telluride crystal using tunable oscillator laser pulses," 13th Int. Conf. Fiber Opt. Photonics (2016), Pap. W3A.6 W3A.6 (2016).

230. J. Xu, X.-C. Zhang, and X. Xie, "Terahertz wave generation and detection from a CdTe crystal characterized by different excitation wavelengths," Opt. Lett. Vol. 31, Issue 7, pp. 978-980 **31**, 978–980 (2006).

231. P. Ščajev, S. Miasojedovas, A. Mekys, D. Kuciauskas, K. G. Lynn, S. K. Swain, and K. Jarašiunas, "Excitation-dependent carrier lifetime and diffusion length in bulk CdTe determined by time-resolved optical pump-probe techniques," J. Appl. Phys. **123**, 025704 (2018).

232. C. Kraft, H. Hempel, and V. Buschmann, "Spatially resolved measurements of charge carrier lifetimes in CdTe solar cells ARTICLES YOU MAY BE INTERESTED IN," J. Appl. Phys **113**, 124510 (2013).

233. K. Biswas and M. H. Du, "What causes high resistivity in CdTe," New J. Phys. **14**, 063020 (2012).

234. A. Gädda, J. Ott, A. Karadzhinova-Ferrer, M. Golovleva, M. Kalliokoski, A. Winkler, P. Luukka, and J. Härkönen, "Cadmium Telluride X-ray pad detectors with different passivation dielectrics," Nucl. Instruments Methods Phys. Res. Sect. A Accel. Spectrometers, Detect. Assoc. Equip. **924**, 33–37 (2019).

235. M. C. Beard, G. M. Turner, and C. A. Schmuttenmaer, "Transient photoconductivity in GaAs as measured by time-resolved terahertz spectroscopy," Phys. Rev. B **62**, 15764 (2000).

236. J. N. Heyman, D. Bell, and T. Khumalo, "Terahertz photo-Hall measurements of carrier mobility in GaAs and InP," Appl. Phys. Lett. **88**, (2006).

237. G. Zhao, R. N. Schouten, N. Van Der Valk, W. T. Wenckebach, and P. C. M. Planken, "Design and performance of a THz emission and detection setup based on a semi-insulating GaAs emitter," Rev. Sci. Instrum. **73**, 1715 (2002).

238. A. Bhattacharya, A. Bhattacharya, A. Bhattacharya, D. Ghindani, D. Ghindani, and S. S. Prabhu, "Enhanced terahertz emission bandwidth from photoconductive antenna by manipulating carrier dynamics of semiconducting substrate with embedded plasmonic metasurface," Opt. Express, Vol. 27, Issue 21, pp. 30272-30279 **27**, 30272–30279 (2019).

239. K.-H. Jeong, Y. Choi, Y.-J. Oh, and S.-G. Park, "Terahertz photoconductive antenna with metal nanoislands," Opt. Express, Vol. 20, Issue 23, pp. 25530-25535 **20**, 25530–25535 (2012).

240. V. Amendola, R. Pilot, M. Frasconi, O. M. Maragò, and M. A. Iatì, "Surface plasmon resonance in gold nanoparticles: a review," J. Phys. Condens. Matter **29**, 203002 (2017).

241. B. Karlik, M. F. Yilmaz, M. Ozdemir, C. T. Yavuz, and Y. Danisman, "A Hybrid Machine Learning Model to Study UV-Vis Spectra of Gold Nanospheres," Plasmonics **16**, 147–155 (2021).

242. K. Tanaka, K. Naka, E. Miyoshi, A. Narita, and Y. Chujo, "Control of interparticle spacing in stable aggregates of gold nanoparticles by light irradiation," Polym. J. 2015 4711 **47**, 747–752 (2015).

243. D. S. Sidhaye, S. Kashyap, M. Sastry, S. Hotha, and B. L. V. Prasad, "Gold nanoparticle networks with photoresponsive interparticle spacings," Langmuir **21**, 7979–7984 (2005).

244. M. Essone Mezeme and C. Brosseau, "Engineering nanostructures with enhanced thermoplasmonic properties for biosensing and selective targeting applications," Phys. Rev. E - Stat. Nonlinear, Soft Matter Phys. **87**, 012722 (2013).

245. A. Yuksel, M. Cullinan, E. T. Yu, and J. Murthy, "Near-field plasmonics of gold nanoparticles in dielectric media," J. Quant. Spectrosc. Radiat. Transf. **254**, 107207 (2020).

246. S. Lepeshov, A. Gorodetsky, A. Krasnok, E. Rafailov, and P. Belov, "Enhancement of terahertz photoconductive antenna operation by optical nanoantennas," Laser Photon. Rev. **11**, 1600199 (2017).

247. S. J. O. Hardman, D. M. Graham, S. K. Stubbs, B. F. Spencer, E. A. Seddon, H. T. Fung, S. Gardonio, F. Sirotti, M. G. Silly, J. Akhtar, P. O'Brien, D. J. Binks, and W. R. Flavell, "Electronic and surface properties of PbS nanoparticles exhibiting efficient multiple exciton generation," Phys.

Chem. Chem. Phys. **13**, 20275–20283 (2011).

248. A. Hajjaji, S. Jemai, K. Trabelsi, A. Kouki, I. Ben Assaker, I. Ka, M. Gaidi, B. Bessais, and M. A. El Khakani, "Study of TiO2 nanotubes decorated with PbS nanoparticles elaborated by pulsed laser deposition: microstructural, optoelectronic and photoelectrochemical properties," J. Mater. Sci. Mater. Electron. **30**, 20935–20946 (2019).

249. M. Seo and H. R. Park, "Terahertz Biochemical Molecule-Specific Sensors," Adv. Opt. Mater. **8**, 1900662 (2020).

250. M. Hangyo, M. Tani, and T. Nagashima, "Terahertz Time-Domain Spectroscopy of Solids: A Review," Int. J. Infrared Millim. Waves 2005 2612 **26**, 1661–1690 (2005).

251. H. B. Liu, H. Zhong, N. Karpowicz, Y. Chen, and X. C. Zhang, "Terahertz spectroscopy and imaging for defense and security applications," Proc. IEEE **95**, 1514–1527 (2007).

252. R. Piccoli, R. Piccoli, A. Rovere, Y.-G. Jeong, Y. Jia, L. Zanotto, F. Légaré, B. E. Schmidt, R. Morandotti, R. Morandotti, R. Morandotti, L. Razzari, and L. Razzari, "Extremely broadband terahertz generation via pulse compression of an Ytterbium laser amplifier," Opt. Express, Vol. 27, Issue 22, pp. 32659-32665 **27**, 32659–32665 (2019).

253. P. Bawuah and J. A. Zeitler, "Advances in terahertz time-domain spectroscopy of pharmaceutical solids: A review," TrAC Trends Anal. Chem. **139**, 116272 (2021).

254. S. K. Mathanker, P. R. Weckler, and N. Wang, "Terahertz (THz) Applications in Food and Agriculture: A Review," Trans. ASABE **56**, 1213–1226 (2013).

255. Z. Yan, L. G. Zhu, K. Meng, W. Huang, and Q. Shi, "THz medical imaging: from in vitro to in vivo," Trends Biotechnol. **40**, 816–830 (2022).

256. N. Vohra, T. Chavez, J. R. Troncoso, N. Rajaram, J. Wu, P. N. Coan, T. A. Jackson, K. Bailey, and M. El-Shenawee, "Mammary tumors in Sprague Dawley rats induced by N-ethyl-N-nitrosourea for evaluating terahertz imaging of breast cancer," https://doi.org/10.1117/1.JMI.8.2.023504 **8**, 023504 (2021).

257. B. N. Flanders, D. C. Arnett, and N. F. Scherer, "Optical pump-terahertz probe spectroscopy utilizing a cavity-dumped oscillator-driven terahertz spectrometer," IEEE J. Sel. Top. Quantum Electron. **4**, 353–359 (1998).

258. T. Seifert, S. Jaiswal, U. Martens, J. Hannegan, L. Braun, P. Maldonado, F. Freimuth, A. Kronenberg, J. Henrizi, I. Radu, E. Beaurepaire, Y. Mokrousov, P. M. Oppeneer, M. Jourdan, G. Jakob, D. Turchinovich, L. M. Hayden, M. Wolf, M. Münzenberg, M. Kläui, and T. Kampfrath, "Efficient metallic spintronic emitters of ultrabroadband terahertz radiation," Nat. Photonics 2016 107 **10**, 483–488 (2016).

259. X. Chen, H. Wang, C. Wang, C. Ouyang, G. Wei, T. Nie, W. Zhao, J. Miao, Y. Li, L. Wang, and X. Wu, "Efficient Generation and Arbitrary Manipulation of Chiral Terahertz Waves Emitted from Bi2Te3–Fe Heterostructures," Adv. Photonics Res. **2**, 2000099 (2021).

260. S. Uemura and K. Torizuka, "Sub-40-fs pulses from a diode-pumped kerr-lens mode-locked Yb-doped yttrium aluminum garnet laser," Jpn. J. Appl. Phys. **50**, 010201 (2011).

261. M.-C. Amann, J. Brons, O. Pronin, V. Pervak, G. Boehm, V. L. Kalashnikov, C. Grasse, A. Apolonski, and F. Krausz, "High-power 200 fs Kerr-lens mode-locked Yb:YAG thin-disk oscillator," Opt. Lett. Vol. 36, Issue 24, pp. 4746-4748 **36**, 4746–4748 (2011).

262. K. Ning, H. Huang, X. Xu, D. Tang, J. Ma, K. P. Loh, L. Qian, and G. Xie, "Generation of 30 fs pulses from a diode-pumped graphene mode-locked Yb:$CaYAlO_4$ laser," Opt. Lett. Vol. 41, Issue 5, pp. 890-893 **41**, 890–893 (2016).

263. M. B. Harreguy, V. Marfil, N. W. F. Grooms, C. V. Gabel, S. H. Chung, and G. Haspel, "Ytterbium-doped fibre femtosecond laser offers robust operation with deep and precise microsurgery of C. elegans neurons," Sci. Reports 2020 101 **10**, 1–7 (2020).

264. H. G. Breunig, A. Batista, A. Uchugonova, and K. König, "Cell optoporation with a sub-15 fs and a 250-fs laser," J. Biomed. Opt. **21**, 060501 (2016).

265. R. J. B. Dietz, A. Brahm, A. Velauthapillai, A. Wilms, C. Lammers, B. Globisch, M. Koch, G. Notni, A. Tünnermann, T. Göbel, and M. Schell, "Low temperature grown photoconductive antennas for pulsed 1060 nm excitation: Influence of excess energy on the electron relaxation," J. Infrared, Millimeter, Terahertz Waves **36**, 60–71 (2015).

266. V. Pačebutas, A. Bičiūnas, S. Balakauskas, A. Krotkus, G. Andriukaitis, D. Lorenc, A. Pugžlys, and A. Baltuška, "Terahertz time-domain-spectroscopy system based on femtosecond Yb:fiber laser and GaBiAs photoconducting components," Appl. Phys. Lett. **97**, 031111 (2010).

267. R. B. Kohlhaas, S. Breuer, L. Liebermeister, S. Nellen, M. Deumer, M. Schell, M. P. Semtsiv, W. T. Masselink, and B. Globisch, "637 µW emitted terahertz power from photoconductive antennas based on rhodium doped InGaAs," Appl. Phys. Lett. **117**, 131105 (2020).

268. M. Bashirpour, M. Forouzmehr, S. E. Hosseininejad, M. Kolahdouz, and M. Neshat, "Improvement of Terahertz Photoconductive Antenna using Optical Antenna Array of ZnO Nanorods," Sci. Rep. **9**, 1–8 (2019).

269. I. Ka, L. F. Gerlein, I. M. Asuo, R. Nechache, and S. G. Cloutier, "An ultra-broadband perovskite-PbS quantum dot sensitized carbon nanotube photodetector," Nanoscale **10**, 9044–9052 (2018).

270. G. Zhao, R. N. Schouten, N. Van Der Valk, W. T. Wenckebach, and P. C. M. Planken, "Design and performance of a THz emission and detection setup based on a semi-insulating GaAs emitter," Rev. Sci. Instrum. **73**, 1715 (2002).